University of Nevada, Reno

Modeling, Simulation and Validation of a Bio-Inspired and Self-Powered Miniature Pressure Sensing System for Monitoring Cerebral Intra Aneurysmal Pressure

A dissertation submitted in partial fulfillment of the

requirements for the degree of

Doctor of Philosophy

In BioMedical Engineering

by

Nithya P Mohan

Dr. Yantao Shen / Dissertation Advisor

December 2017

THE GRADUATE SCHOOL

We recommend that the dissertation
prepared under our supervision by

NITHYA P MOHAN

Entitled

Modeling, Simulation and Validation of a Bio-Inspired and Self-Powered Miniature Pressure Sensing System for Monitoring Cerebral Intra Aneurysmal Pressure

be accepted in partial fulfillment of the
requirements for the degree of

DOCTOR OF PHILOSOPHY

Dr. Yantao Shen, Advisor

Dr. Bahram Parvin, Committee Member

Dr. Xiaoshan Zhu, Committee Member

Dr. Hung La, Committee Member

Dr. Matteo Aureli, Graduate School Representative

David W. Zeh, Ph. D., Dean, Graduate School

December, 2017

Abstract

Intracranial aneurysm rupture is one of the main cause for the intracranial bleeding. A brain aneurysm is an abnormal focal bulging of the arteries in the brain. As an aneurysm grows, its wall becomes thinner and weaker, which is more prone to rupture. Rupture of the intracranial aneurysm leads to releasing blood into the spaces around the brain - called a subarachnoid hemorrhage (SAH). 10 to 15% of the patients with subarachnoid hemorrhage die immediately. To prevent aneurysmal bleeding, it is essential to seclude the aneurysm from the blood circulation. This can be done with open craniotomy with microsurgical clipping and minimally invasive endovascular surgery. One of endovascular surgical technique is to place stent/flow-diverter across the neck of the aneurysm. The stent across the aneurysm reduces the flow within the aneurysm and help to form the thrombus within the aneurysm. However, approximately 3% people with the flow- diverter treatment may have delayed aneurysm bleeding after the stent placement. Short-term studies show that the stents can reduce the flow within the aneurysm but not the pressure. Currently there is no other device available to measure the intracranial intraaneurysmal pressure.

This work is on designing a bio-inspired, self-powered, passively operated PVDF pressure sensor that can be deployed within the aneurysm, during flow diverting endovascular treatment that is very sensitive to small changes in pressure. The design utilizes the ear mechanics benefits by consisting of the circular vibrating membrane which vibrates based on the intraaneursymal pressure changes. This mimic the tympanic membrane part of the ear. The design continues to follow the middle ear's mechanical advantage mechanism by incorporating the surface area increase and leverage mechanism, by the other side of the vibrating membrane been connected to three pole-links structures similar to the three bones of the middle ear to perform the middle ear's amplification mechanism.

This is followed by a composite cantilever beam structure with the sensor strips, which mimics the coiled cochlea of the inner ear in elongated form. This piezoelectric sensor strips are responsible for the passive mechanoelectrical conversion and generation of electric voltage, for the intraaneursymal pressure change application. Simulation, experiments and analysis at every level are done. Simulation and experimental result correlate and match the modeling.

Dedicated to my grandmother, parents, sisters, husband and kids

Acknowledgement

Everything happens the way it happens because of God. I have come this far only because of my God. My heartfelt thanks to my creator.

There have been many people who have walked alongside me during the last five years. They have guided me, placed opportunities in front of me and showed me the doors that might be useful to open. I would like to thank each and every one of them.

I would like to express my sincere appreciation to my advisor, Dr. Shen, for his guidance, energy, inspiration, encouragement and support at all levels. This project would not have been seen the light of day without his guidance and insight. I also thank Drs. Zhu, Parvin, La and Aureli for serving on my committee and their expertise.

I thank my grandma and her sisters for supporting me spiritually with their prayers, my parents for their continuous moral support and encouraging words, and my sisters for never doubting me and for lifting my spirits.

It is my utmost joy to thank my husband, Rajesh, who is solely responsible for this accomplishment of mine. If it was not for him, I wouldn't have

reached this place. Thank you for your constant encouragement and support, lending your shoulders and handling my emotions, believing in me more than me and being proud of me all the time.

Ah, my kids!!! Thank you for waiting patiently for five years for mommy to complete her Ph.D. Thank you Riyaa and Rithik for your strong belief that I will finish my Ph.D. one day and I will start spending more mommy time with you.

Last but not the least, my friends, Thiyahiny for being a sister to me and feeding me and my family while I was busy with my PhD work, Akilan for helping me with several technical issues all through my PhD and Saranya for her continuous moral support. Thank you.

Contents

List of Tables

List of Figures

Chapter 1

Introduction

The blood vessels [1] are part of the circulatory system that transports blood throughout the body. Pathologies in blood vessels are categorized under two major classes: blockage and bleeding [3]. There are several reasons and factors that contribute to blockage and bleeding. One of the common and main causes for bleeding is aneurysm [10]. An aneurysm is an outward abnormal bulging of the artery. As an aneurysm grows it becomes thinner and weaker. Due to various factors, the aneurysmal wall can become thinner and weaker, that at one point, it ruptures releasing blood around the brain causing subarachnoid hemorrhage (SAH). Studies [17] show that that SAH rates range from 5 to 16 cases per 100,000 populations in a year, in which 21000 to 35000 cases are reported from Unites States in a year. The effect of SAH from ruptured aneurysm account for 10 to 15% death immediately. To prevent aneurysmal bleeding, it is essential to seclude the aneurysm from the blood circulation. This can be done with open craniotomy with microsurgical clipping and minimally invasive endovascular surgery. One of endovascular surgical technique is to place stent/flow-diverter across

the neck of the aneurysm. The stent across the aneurysm reduces the flow within the aneurysm and help to form the thrombus within the aneurysm. However, approximately 3% people with the flow-diverter treatment may have delayed aneurysm bleeding after the stent placement. The reason behind this rupture is still unclear. One of the main theories behind this rupture is: no change in the pressure within the aneurysm [37]. The theory states that although the endoluminal devices (one of the endovascular treatment options) divert and reduce the flow within the aneurysm, they don't divert or substantially reduce the pressure within the aneurysm and thereby cause a delayed rupture.

1.1 Goal and Objectives

The main goal is to design a self-powered and highly sensitive pressure sensor that can be deployed within the aneurysm, during flow diverting endovascular treatment, which is small in size, and which is very sensitive to small changes in pressure, passively operated and that can transmit the signal wirelessly.

The goal is achieved by accomplishing the following two main objectives:

1. To design a bio-inspired pressure sensor that is sensitive to small changes in pressure inside the intracranial aneurysm

The pressure sensor needs to be small and biocompatible; light weight, flexible and compact; strong and wear resistant; highly sensitive and precise with high levels of chemical inertness suitable for long term implantations; and should be able to generate the output signal passively. The design utilizes the ear mechanics benefits by consisting of the circular vibrating membrane which vibrates based on the intraaneursymal pressure changes, followed by middle ear mimicked three-pole link for mechanical amplification and an inner ear inspired composite cantilever beam structure with piezoelectric PolyVinyliDene Fluoride(PVDF) striped sensing layers.

2. To design a self-powered sensor with digitalization mechanism for data recovery

This part focuses the next step of how the dynamic signal (voltage) (if seen) generated by the PVDF sensors gets converted back to the variations (if seen) of the blood pressure inside the aneurysm. To account for that, each piezo sensor's output is connected to a microchip, which has built-in memory that stores these digitalized signals, for which the power can be passively generated by another PVDF layer beneath the beam. Any pressure change, if present, inside the aneurysm after the flow-diverting stent placement can be digitized.

1.2 Contributions

The work focusses on designing the pressure sensor unit by incorporating the human ear mechanics benefits. The design consists of the circular vibrating membrane which vibrates based on the intraaneursymal pressure changes. This mimic the tympanic membrane part of the ear. The other side of the vibrating membrane is connected to three pole-links structures similar to the three bones of the middle ear to perform the middle ear's leverage amplification mechanism.

The composite striped sensing cantilever beam structure mimics the coiled cochlea of the inner ear, in elongated form. This piezoelectric striped sensing beam is responsible for the passive mechanoelectrical conversion and generation of electric voltage, for the intraaneursymal pressure change application.

The surface area of the vibrating membrane is made > 3 times larger than that of the circular part of the last link which deflects the tip of the cantilever beam, upon pressure.

The three-pole mechanical structure is simulated on ANSYS to study its mechanism. Piezoresistive and piezoelectric sensors are used to study and compare, for the striped sensing cantilever beam. Simulation on ANSYS, followed by experiments are done to compare and select the better suited

one for this application. Piezoelectric sensors are selected due to their inherent passive generation of electric signals' capability. The pressure sensing unit is modeled and validated. Later, simulation and experimental analyses are done on the pressure unit and validated with the modeling.

The work continues to propose the self-powered mechanism to provide power for the microchip which has built-in memory to store the digitalized signals. The power required for the micro-chip can be passively generated and supplied by placing a PVDF layer beneath the beam for its length. The design continues to propose the digitalization model where any pressure change, if present, inside the aneurysm after the flow-diverting stent placement is digitized as "1". The minimal pressure change that is in consideration in our analysis is 10mmHg of pressure difference from the parent vessel artery.

1.3 Dissertation Overview

The dissertation is organized as follows. Chapter 2 presents and discusses the background and significance of the work. Information on aneurysm, its significance and treatments options are discussed. Additionally, the complications that are seen with one current treatment option and the limitation in technology present is discussed.

Chapter 3 provides a review of previous work. It discusses the possible evidence of pressure or some kind of stress present inside the aneurysm

after flow-diverting stent placement and the technological devices that are currently available in the market, along with their limitations.

Chapter 4 presents the design specifications of the pressure sensor unit. It discusses the bio-mimicked process from human ear by discussion on the theory and principle of the ear hearing, piezoresistive and piezoelectricity (for sensors); presentation and discussion of the bio-inspired pressure sensor unit design; followed by discussion on the proposed self-power and digitalization of the output signal.

To validate and study the proposed mechanical part of the bio-mimic pressure sensor unit; one part of the unit that mimics the middle ear structure, for amplification, is modelled and simulated in ANSYS. The results are discussed in chapter 5.

In Chapter 6, comparison and analyzes on piezoresistive and piezoelectric sensing beams are done by simulation and experiments. Piezoelectric sensing beams on cantilever beam is used on further analyzes due to its self-power inherent quality.

Chapter 7 provides the modeling for the PVDF striped sensing beam. It also provides the simulation results from ANSYS 16.2 which are done to test the validity of the modeling.

Chapter 8 provides the results and discussion of the experimental analysis on the pressure sensor unit design. The results, design and the modeling are verified using Digital Signal Analyzer.

Chapter 9 provides a brief proposal of the future work on wireless transmission of the digitized signal. It provides the conclusion, followed by appendices.

Chapter 2

Background and Significance

The blood vessels, a part of the circulatory system, transport blood throughout the body [1]. There are three major types of blood vessels [1]: the arteries, carry the blood away from the heart; the veins, carry blood from the capillaries back toward the heart. and the capillaries, enable the actual exchange of water and chemicals between the blood and the tissues. Several known or unknown factors [2] like wall shear stress, weakness in blood vessels, thickening of blood vessels due to fatty deposits, blood clot formation or congenital abnormalities, cause mild to severe pathologies, which at times could be fatal. Pathologies in blood vessels are categorized under two major classes: blockage and bleeding [3]. Blockage causes loss of blood supply to a particular organ or brain and that leads to ischemic stroke [4] (Figure 2.1). Bleeding [1] is caused by rupture of the blood vessel and it leads to hemorrhagic stroke [5] (Figure 2.2). There are several reasons and factors that contribute to blockage and bleeding [6]. Some of the common causes are discussed below.

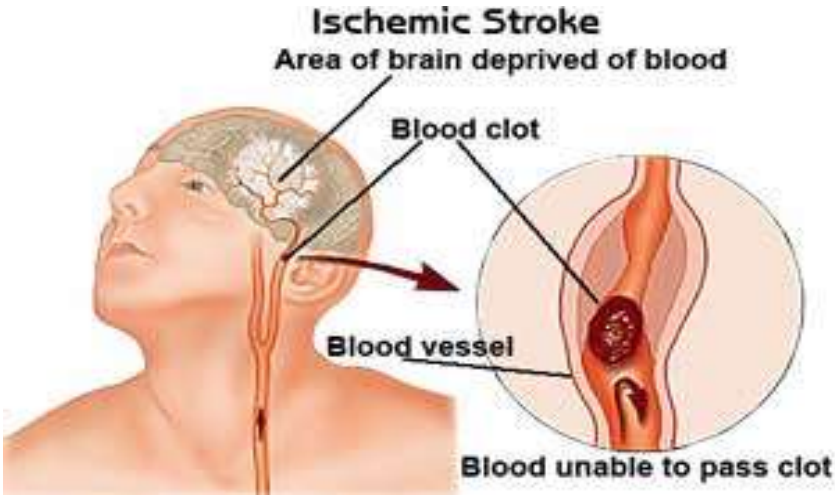

Figure 2.1: Ischemic stroke (adopted from ischemicstroke.org)

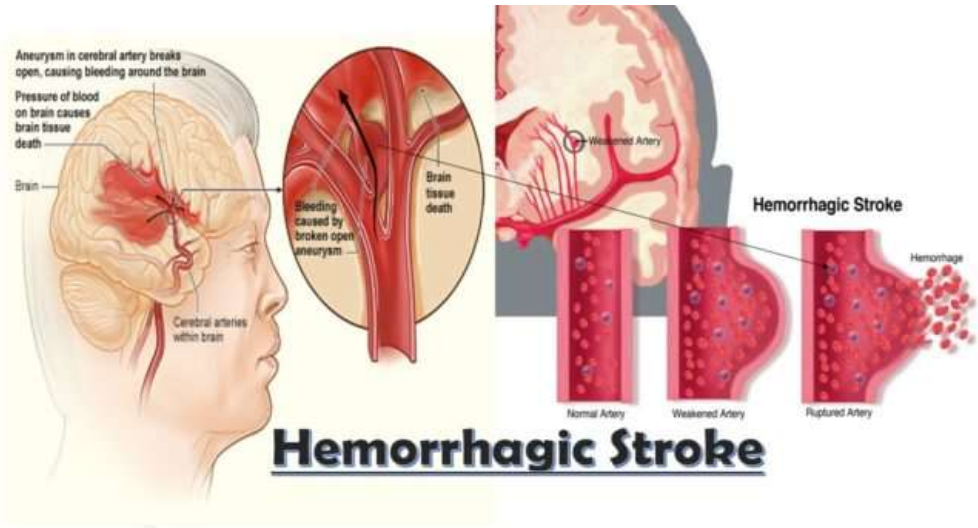

Figure 2.2: Hemorrhagic stroke (adopted from hemorrhagicstroke.org)

Blockage is further classified into occlusion (complete blockage) or stenosis (constricted blood vessel). Occlusion is caused by thrombosis [7] (a blood clot in the brain or neck) or embolism [8] (a blood clot from somewhere else that has moved and now blocks a blood vessel in the brain

or neck). Stenosis [9] is caused by atherosclerosis (thickening of blood vessel due to fat deposits), vasculitis (inflammation of the blood vessel wall) or dissection (bleeding within the vessel wall).

Bleeding is caused by either aneurysm [10] (an abnormal outward bulging of the arteries) or vascular malformation [11] (abnormal arterio-venal connection). Aneurysm is caused by several known and unknown factors [12] like weakness of the blood vessels, wall shear stress, inflammation, etc. Vascular malformation is congenital. Since the focus of the research is on aneurysm, all discussions will be on it.

2.1 Brain Aneurysms

A brain aneurysm [13] (Figure 2.3) is an abnormal bulging outward of one of the arteries in the brain. As an aneurysm grows it becomes thinner and

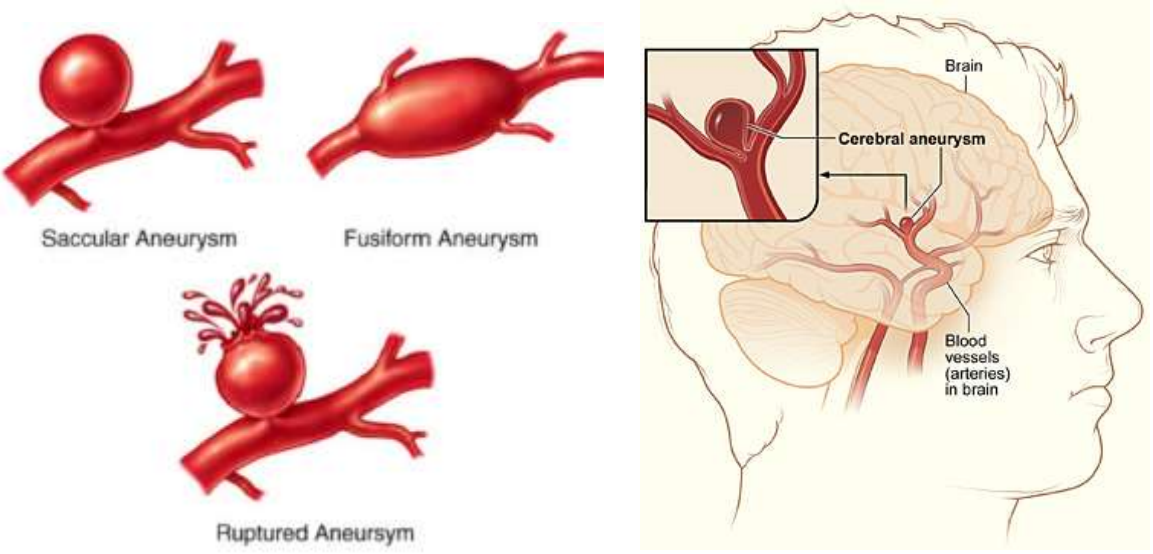

Figure 2.3: Brain aneurysm (adopted from anatomy-medicine.org)

weaker [14]. Due to various factors, the aneurysmal wall can become thinner and weaker, that at one point, it ruptures releasing blood around the brain causing subarachnoid hemorrhage (SAH). [15].

Aneurysms are typically and commonly observed at bifurcations [16] of the arteries, branching of blood vessels and at segments with shorter radii of curvature which receives higher hemodynamic stresses. It is shown in Figure 2.4.

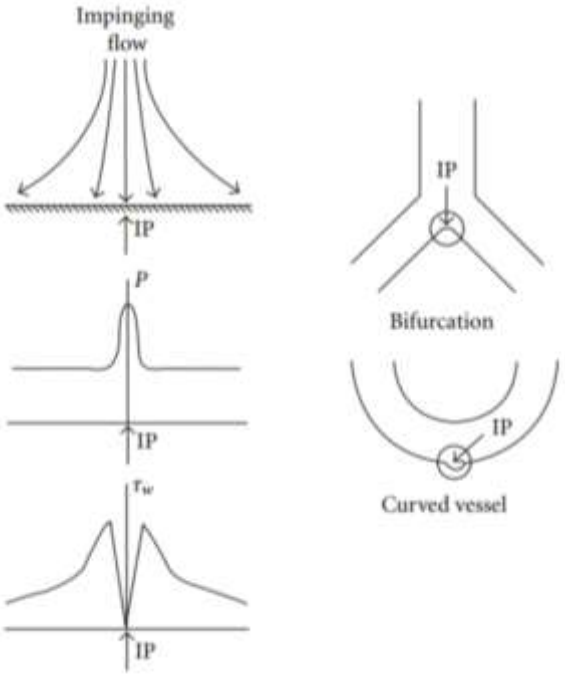

Figure 2.4: Typical locations of aneurysms (adopted from https://clinicalgate.com [16])

Studies have been done for more than a decade and they show that aneurysmal growth and formation is highly related to the elevated abnormal hemodynamic stress factors [16]. Almost 90% of aneurysms are noted in the anterior circulation (Anterior Communicating Artery

accounting for 40%, Internal Carotid Artery for 26 to 30% and Middle Cerebral Artery for 22 to 28%). Vertebrobasilar system accounts for a 10% of the aneurysms. It is shown in Figure 2.5. Based on the size, aneurysms are classified into subgroups as small aneurysms (<4 mm), medium aneurysms (4 to 12 mm), large aneurysms (12 to 24 mm) and giant aneurysms (> 25 mm) [16]. Also, based on the morphological structure, they are classified as saccular or fusiform aneurysm.

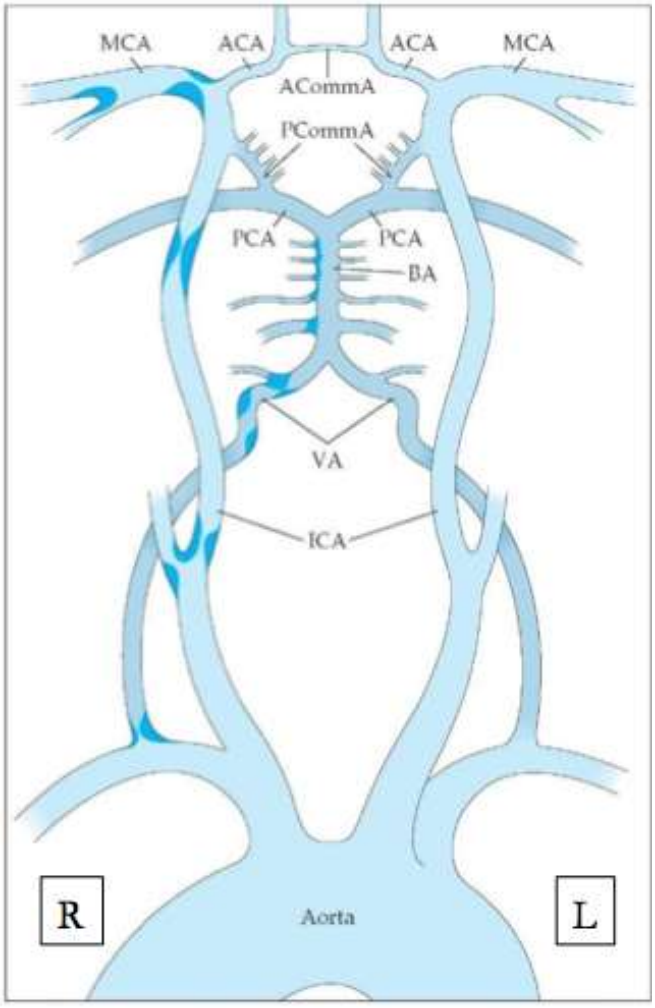

Figure 2.5: Anatomical location of occurrences of brain aneurysms (adopted from https://clinicalgate.com)

2.2 Subarachnoid Hemorrhage

Subarachnoid hemorrhage (SAH) is the most common and serious cause of a ruptured intracranial aneurysm. The symptoms of SAH include sentinal headache (within 1 to 6 weeks prior to SAH), sudden onset of severe headache, nuchal rigidity, fever, photophobia and reduced level of consciousness. Studies [17] show that that SAH rates range from 5 to 16 cases per 100,000 populations in a year, in which 21000 to 35000 cases are reported from Unites States in a year. The effect of SAH from ruptured aneurysm account for 10 to 15% death immediately. The risk of rebleeding and/or a neurological deficit risk contribute to 50-60% of the cases that survived the initial phase. Although upto 2.4% of aneurysms (in ruptured form) are noted in autopsy, clinical and angiographic studies, most of the unruptured aneurysms are asymptomatic.

Size / **Location**	**<4 mm**	**4 to 12 mm**	**13 to 24 mm**	**>25 mm**
Cavernous ICA	0%	0%	3%	6.4%
ACA / MCA / SC ICA	0 – 1.5%	2.6%	14.5%	40%
PCoM / BA	2.5-3.4%	14.5%	18.4%	50%

Table 2.1: Percentage of bleeding for patients with unruptured aneurysms (without treatment) (adopted from [18] Pouratian N et al)

Some symptoms associated with unruptured aneurysms are mass effect, cranial nerve palsy, epilepsy and embolic phenomenon. These unruptured aneurysms, if not treated, has a percentage of risk of rupture and bleeding based on its location and size. Table 2.1[18] summarizes the percentage of bleeding of unruptured aneurysms when not treated.

2.3 Treatment Options for Aneurysms

With the advent of non-invasive imaging modalities, an increased number of unruptured, incidental aneurysms are being detected and decision on the treatment procedure is made. There are two different treatment approaches available today: micro surgery [19] (clipping) and endovascular surgery. The focus of this report will be on endovascular surgery. Endovascular surgery [20] is a form of minimally invasive surgery. A catheter, guided by a guidewire, carrying devices or miniature instruments is inserted into a blood vessel, through the femoral artery, for the treatment of vascular disease. Endovascular surgery [21] is performed by radiologists, neurologists, neurosurgeons, cardiologists, and vascular surgeons. The procedure (Figure 2.6) is performed by making a small incision on the femoral artery and by navigating a guiding catheter (6F to 8F:1F=0.33 mm) with the help of a guidewire to the base of the skull, where the artery's diameter is more than 4mm.

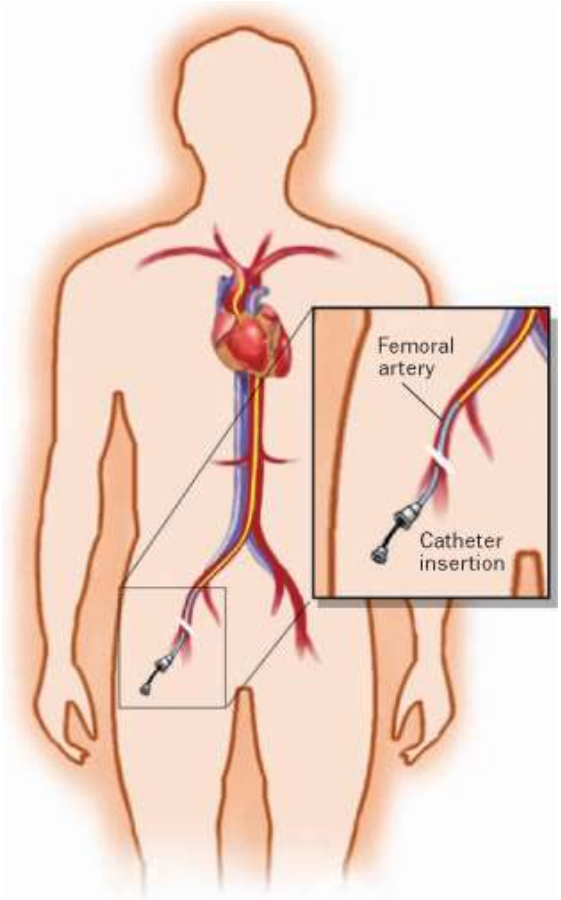

Figure 2.6: Endovascular surgery (adopted from medicine.stonybrookmedicine.edu)

A micro-guidewire followed by a micro-cathether (0.017 to 0.028 inch) is introduced into the guiding catheter and it goes to the location where aneurysm is present. Through the microcatheter are inserted the endovascular devices to treat the aneurysm. Based on the size, location and morphology of the aneurysm, few endovascular treatment options [22] are available. They are categorized as endo-saccular treatments and endo-luminal treatments. Simple Coiling, Balloon-assisted Coiling, Stent-

assisted Coiling, Liquid embolization are few endo-saccular treatments. Flow diverting Stents fall under endo-luminal treatment option.

2.4 Endovascular Treatment Options

Endovascular coiling (Figure 2.7) has become an accepted and often first-line treatment for ruptured and unruptured intracranial aneurysms [23]. The coils [24] used for endovascular treatment are thin metal wires made up of platinum (92%) and tungsten (8%). The coils come with an introducer sheath which is deployed inside the aneurysm via the catheter. The coils

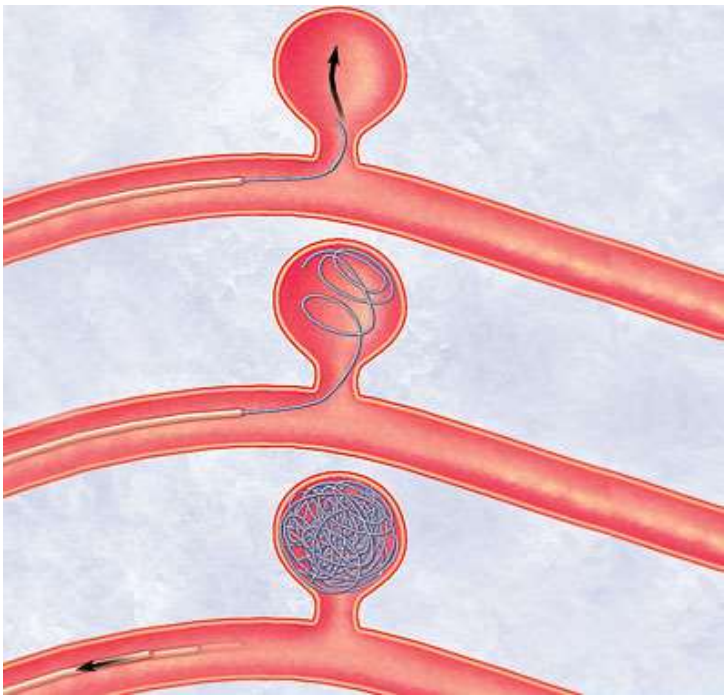

Figure 2.7: Endovascular coiling (adopted from mayoclinic.org)

act as an embolizing device and occlude the aneurysm, thereby diverting the blood flow through the parent blood vessel [25].

Balloon-assisted coiling [26] is used each time the shape of the aneurysm makes use of the standard treatment impossible or difficult, particularly when the neck is wide-larger than 6 mm. Balloon-assisted coiling is used to treat wide-neck aneurysms, in which a small balloon (Figure 2.8) is inflated and deflated alternatively during the deployment of coils within the aneurysm, to protect the parent vessel artery and to hold the coils inside the aneurysm.

Figure 2.8: Balloon assisted coiling (adopted from [26], Spiotta A. M et al)

In case of aneurysms that have a wide neck [27], a stent (Figure 2.9) is placed in conjugation with coiling, to hold the coils in place. Stent [28] is a small self-expandable mesh tube commonly made up of nitinol

(nickel/titanium). Nitinol has the mechanical properties of super elasticity and shape memory alloy.

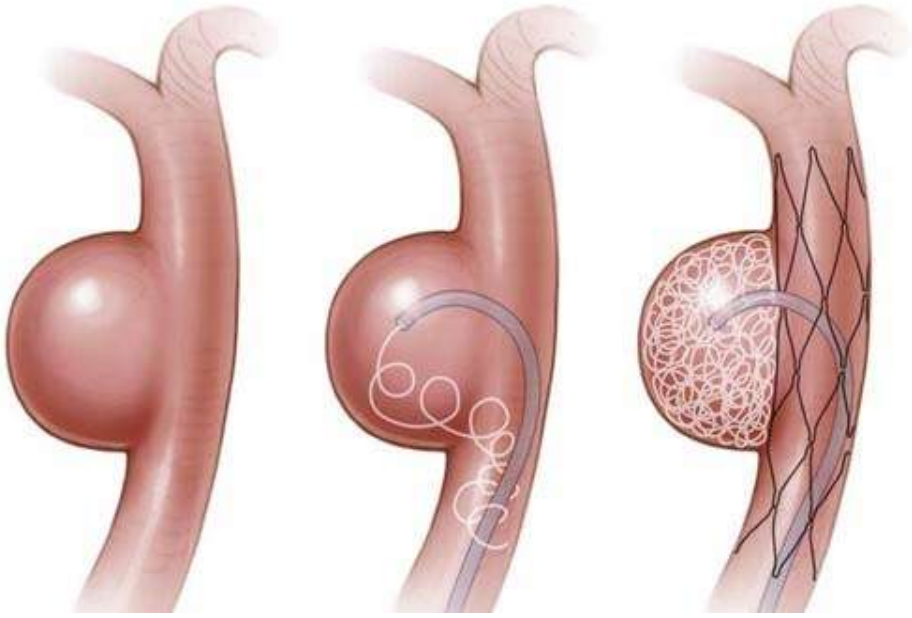

Figure 2.9: Stent assisted coiling (adopted from [27], Spiotta A. M et al)

Another endovascular method is to fill the aneurysms with the liquid embolic agent like Onyx HD 500. This liquid embolic agent [29] is comprised of 20% EVOH, ethylene vinyl alcohol, copolymer and 80% of DMSO, dimethylsulfoxide. It is mixed with micronized tantalum powder [29], to provide contrast for visualization under fluoroscopy. Once it comes in contact with blood, it forms a clot and stops bleeding.

Flow-diverting stents (Figure 2.10) now offer a new alternative treatment for aneurysms. Unlike the above techniques, this option focuses on remodeling the parent artery. These stent [30] have 30% more metal

coverage to keep the small blood vessels open. The more metal coverage reduces and thereby stagnates the blood flow to the aneurysm. This stagnation causes thrombosis inside the aneurysm and embolizes it. The flow diverting stent to get the first FDA approval in USA is the Pipeline Embolization Device. The stent is a wired cylindrical mesh made of strands of braids of platinum and nickel-cobalt chromium alloy [30], with 30% metal surface coverage to be placed within the parent vessel artery to treat brain aneurysms. It comes in varying lengths on up to 20 mm and diameters in the range of 2.5-5 mm in 0.25 mm increments. The stent comes in a closed cell design with a higher radial force. It comes with its own pusher wire and is compatible with a 3F microcatheter and can be retrieved up to full deployment. The flow diverters are used to treat giant or thin walled aneurysms.

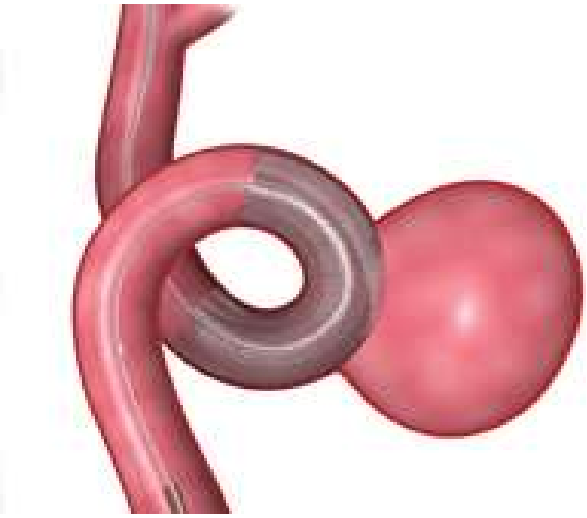

Figure 2.10: Flow-diverting stent (adopted from [30],Zhang J., Lu X. et al)

When placed across the aneurysm neck, the flow diverter's role is to redirect the blood flow away from the aneurysm, thereby causing stagnation of blood inside the aneurysm. This stagnation of blood induces blood clot.

The clot inside the aneurysm prevents rupture of the aneurysm and may also cause the aneurysm to shrink in size over time. Thus, the Pipeline Device works on restoring original, natural blood circulation while providing permanent long-term occlusion.

2.5 Complication in Flow-Diverting Stents

The treatment results for the flow-diverting stents are promising; however, early postprocedural aneurysm rupture (3 to 6 months after the procedure) has been described [31]. The actual reason for this unknown delayed rupture is still unclear but maybe related to the intra-aneurysmal pressure changes. The complications associated with flow diverters are hemorrhagic complications due to delayed aneurysm rupture. Currently, the actual or exact hemodynamic reasons causing the delayed aneurysm rupture through flow diversion are still unclear [32,33,34]. With the available treatment options, studies show that the pre-procedural complication rate is 3 to 5% [32] leading to stroke or rupture of aneurysm. The post procedural complication rate is 3% leading to delayed bleeding.

Endoluminal treatments of aneurysms currently available today post a 3% post rupture rate within 3-6 months of the procedure. The reason behind this rupture is still unclear. The reasons behind this rupture are just theories. One of the main theories is: no change in the pressure within the aneurysm. The theory states that although the endoluminal devices divert and reduce the flow within the aneurysm, they don't divert or substantially reduce the pressure within the aneurysm [32] and thereby cause a delayed rupture. There has been quite an extensive work done real-time but short term [12] or computationally [33,34,35] to show that no substantial pressure may be a reason for the rupture. To add to it, another theory behind this unclear state is: autolysis of aneurysmal wall due to thrombosis may contribute to the delayed aneurysmal rupture. With all theories and study behind this post rupture rate, there is still no device that is available to monitor the aneurysm on a long-term basis (atleast for the 3 to 6 months period where the rupture is actually happening) real-time, and identify the actual reason.

The sizes of the current available pressure sensing devices are significantly large to be implanted or navigated into the intracranial blood vessels. Also, the 3% of the unexplained unclear delayed aneurysmal rupture leads to the necessity of identifying this unexplained state of delayed aneurysm and thereby assist the endovascular surgeons with a more optimal choice of treatment. So, there is a need for a smaller (micro < 1 cm in diameter)

pressure device that can be placed inside the aneurysm during flow diverting treatment that can measure the pressure changes remotely during and after the stent placement. Based on the pressure recordings from the sensor inside the aneurysm, after the stent placement, the future research can be in two directions:

If the pressure changes after the deployment of the stent, it can turn the research focus into development of better stents which may not increase the pressure.

If there is no change in pressure, then the theory that delayed aneurismal rupture due to pressure changes can be ruled out and can further lead to search for other causes of delayed aneurysmal rupture.

Chapter 3

Related Work

To date, there are up to three pressure sensing devices available in market to measure endoluminal pressure and pressure changes after stent placement across abdominal aortic aneurysm and pulmonary artery aneurysm [36]. They are Endosure Wireless Pressure Sensor (CardioMEMS, Inc, Atlanta, USA), Remon Impressure AAA Sac Pressure Transducer (Remon Medical, Tel Aviv, Israel), and, Telemetric Pressure Sensor (Helmholtz Institute for BioMedical Engineering, RWTH Aachen along with the Institute of Materials in Electrical Engineering, RWTH Aachen [36].

Remon Impressure AAA Sac Pressure Transducer is shown in Figure 3.1 and it measures 3 mm * 9 mm * 1.5 mm. It comes sewn to the stent graft [36,37] and is packaged in the delivery sheath. Ultrasound waves from a handheld probe charges the capacitor by actuating the piezoelectric membrane. The transducer measures the ambient pressure and generates an equivalent ultrasound signal, which is relayed to the probe.

Figure 3.1: Remon Impressure AAA pressure transducer (adopted from [37], Ellozy S.H., Carroccio et al)

Endosure Wireless Pressure Sensor is shown in Figure 3.2. It measures 30 mm* 5 mm * 1.5 mm and comes with its own sheath to be delivered inside the aneurysm [36,38]. It consists of several laminating layers that forms a capacitor, along with metal spirals on its first and last layers to form the inductor [38]. Induction of current in the sensor circuit causes energy oscillation that varies with frequency. The pressure in the aneurysm causes changes in the circuit's resonant frequency. The sensor comes with an external antenna [38], which can measure the change in the resonant frequency.

Figure 3.2: Endosure wireless pressure sensor (adopted from [38], Silveira P.G., Miller C.W.T.. et al)

Telemetric Pressure Sensor [36,39] comes with an implantable sensor in the form of a capsule that can be sutured on the aneurysmal wall, and an external readout station. The capsule works on the capacitive absolute pressure sensing technology and consists of an in capsule microchip for signal processing and telemetry. It does not need a power source. It measures 26 mm * 3.3 mm. The fixation holes at both ends of the capsule allows it to be sutured on the aneurysmal wall before the stent placement. It comes with its own deployment system.

The major limitation in all the above available implantable pressure sensors is the size to place in the intracranial aneurysms. Along with that, the complication rate and its unknown cause with rupture of aneurysms after the deployment of flow diverting stent urges the need for a pressure sensing device.

One of the extensive retrospective cohort studies [40] was done in Canada between July 2008 and December 2010 on 97 cases of unruptured intracranial aneurysms from 7 different Canadian centers with a follow-up range of 0.25 – 2.5 years. The aneurysms were treated with the flow diverting stents, Pipeline Embolization Device (PED) [40]. The 6-month follow-up showed complete or near-complete occlusion in 65% of aneurysms and the one-year follow-up showed complete or near-complete occlusion in 90% of aneurysms. 88% of the patients showed stable or improved outcome. The overall mortality rate was 6% and postprocedural hemorrhage of the aneurysm was seen in 3% of the cases. This study provided an insight on the complication rates that can occur after the use of the flow-diverting stents for unruptured aneurysms. This extensive work was published in August 2012. The authors suggest that careful consideration of the efficacy and morbidity of these devices must be taken into account, when deciding on the treatment options. They also suggest the need for more detailed analysis of flow-diverting stents for radiographic and clinical performance. More related and similar analyses are done on the flow-diverters.

Extensive computational analyses have been done over the past decade to identify the reasons behind the unexplained, still questionable delayed aneurysmal rupture after the procedure. The analyses have focused to

study the hemodynamics within the aneurysm before and after the stent placement. One such study analyzed 7 aneurysm cases that were treated with the flow-diverting stents [31]. Computational Flow Dynamics (CFD) analyses was done on all 7 cases before and after the sent placement. 3 cases ruptured after the treatment and 4 were successfully stented. Hemodynamic changes inside the aneurysm and comparison between the successful and rupture cases were analyzed. CFD results showed a decrease in flow velocity and wall shear stress after flow-diverting stent on the successful cases [31]. However, in each ruptured case, after the stent placement, an increase in pressure was seen in contrast to no significant increase in pressure was seen in the successfully treated 4 cases. The authors discuss the possible scenarios that would have caused the post procedural rupture [31]. Aneurysm present proximal to a stenosed artery have the potential of increased intra-aneurysmal pressure, if the flow diverter resulted in opening the stenosis. Aneurysm located at the bifurcations or branching artery where it receives most of the patent artery flow is highly vulnerable, especially when the aneurysm is a large or giant aneurysm. Autoregulation acting to maintain the flow may cause an increase in the pressure gradient.

Aguilar et al and group [41] studied 23 patients by numerical simulation to identify the potential roles of intra aneurysmal pressure changes and

aneurysm morphologies with flow diverters. Different sized and shaped aneurysms located at the supraclinoid segment of the ICA were prepared for simulation analysis. Wall shear stress, flow velocity, residual and turnover time and pressure changes were accessed before and after the flow diverter placement. Significant reductions in the values were observed for most of the hemodynamic variables after the stent placement, except for the intra-aneurysmal pressure [41]. Calculations did not show a significant reduction in the intra-aneurysmal pressure change or mean pressure in all 23 cases.

A short and intermittent increase in blood pressure and its effect on intra-aneurysmal hemodynamics have been studied by Hasan et al and group [42]. They studied the effect of controlled transient increase in blood pressure inside the aneurysm on various pressure parameters. 12 patients [42] were used in this study. Dual sensor microwires that can measure the flow velocity and pressure (systolic, diastolic and mean) both inside the aneurysm and the parent vessel were used. The pressure was recorded in the dual sensor along with a simultaneous radial artery measurement. A very similar and linear relationship was seen between the radial and aneurysmal pressure changes. The systolic and mean pressure also were similar between the aneurysm and feeder parent vessel.

In order to study the efficacy of flow diverting stents, Shobayashi et al and group created a 3D anatomically realistic computational aneurysm model

of a large internal carotid artery aneurysm from digital subtraction angiogram which can be treated with a flow diverting stent or a neck bridging stent [43]. The 3D models of both the stents were created based on stereo microscope. Both the stents were placed in the computational aneurysmal model and the intra-aneurysmal parameters were measured before and after the stents placement. Computational Fluid Dynamics were performed by solving the continuity and Navier-Stokes equations for steady blood flow on finite volume method. Blood was assumed as an incompressible Newtonian fluid, with vessel walls as rigid, and with no slip boundary conditions. With no stent, the blood entered the aneurysm dome from the mid to proximal neck area and ascended along the distal wall of the aneurysm. It then changed its direction anteriorly and moved along the proximal wall of the aneurysm dome. In addition to it, a counterclockwise vortex was also observed. When the neck bridging stent was placed, a reduction in flow velocity of 14% [43] and a small change in the flow pattern was observed. When the flow diverting stent was placed, a reduction in flow velocity of 74% [43] and a significant reduction in flow pattern intra-aneurysm was observed. Although the flow changes were seen, the Neuroform (neck bridging stent) and Pipeline (flow diverting stent) showed only 4 mmHg and 8 mmHg of pressure reductions respectively. The authors hence concluded that, the effect of flow diverting stent was only in flow reduction. In a non-thrombosed aneurysm [43], the

intra-aneurysmal pressure remained unchanged regardless of which stent was used.

Lu et al and group did a literature review [44] to evaluate the complications with flow diverting stents to better understand it. The complications [44] included aneurysm rupture, occlusion of vessels, stent migration or shortening, intra-aneurysmal pressure and in-stent stenosis, distal brain hemorrhages and embolisms. They suggested proper patient selection, preferably smaller aneurysms without tortuous anatomy can reduce the complications.

Another study was conducted by Aymeric and group [45] to study the associated risk factor with flow diverters. They suggest that 80% of the complication is seen within 30 days of treatment and 80% show poor clinical outcome. The study shows a high correlation between aneurysm rupture after the procedure and giant aneurysms. It also suggests that assisted coiling does not necessarily avoid the risk of delayed rupture as 20% of delayed rupture is seen on aneurysms with flow diverters assisted with coiling.

Although CFD simulations and analyses try to mimic the real-time scenario, many assumptions have to be taken into account. A real-time analysis is indeed difficult but better. To better access the functionality of the flow-diverting stent, a case study [46] was done to measure the

pressure changes before, during and after the deployment of the stent. The patient was a 50-year-old with a partially thrombosed giant aneurysm [46] at the proximal M1 segment of the MCA. The treatment options were to place the flow diverting stent along with partial coiling of the aneurysm, to promote thrombosis. A microcatheter was introduced inside the aneurysm before placement of the flow-diverting stent. Stent was placed over the microcatheter (jailing of microcatheter). A ComboWire featuring a Doppler velocity sensor and a pressure sensor at the tip of the wire was introduced inside the aneurysm via microcatheter to continuously measure intra-aneurysmal pressure before, during and after the stent placement. The pressure inside the aneurysm dropped immediately dropped by 20mm Hg during the stent placement, but was seen to go back to its normal level after the placement of the stent. From the results as in Figure 3.3, the authors infer that no change in the aneurysmal pulse pressure with the stent was seen. They suggest that the stent is a flow diverter but not a pressure diverter and so the aneurysm is not protected from pressure. So this direct aneurysm pressure measurement during the treatment also reveals that that pressure does not necessarily change after the treatment. The immediate direct measurement of pressure using the direct combowire does not accurately represent the delayed changes in the aneurysm.

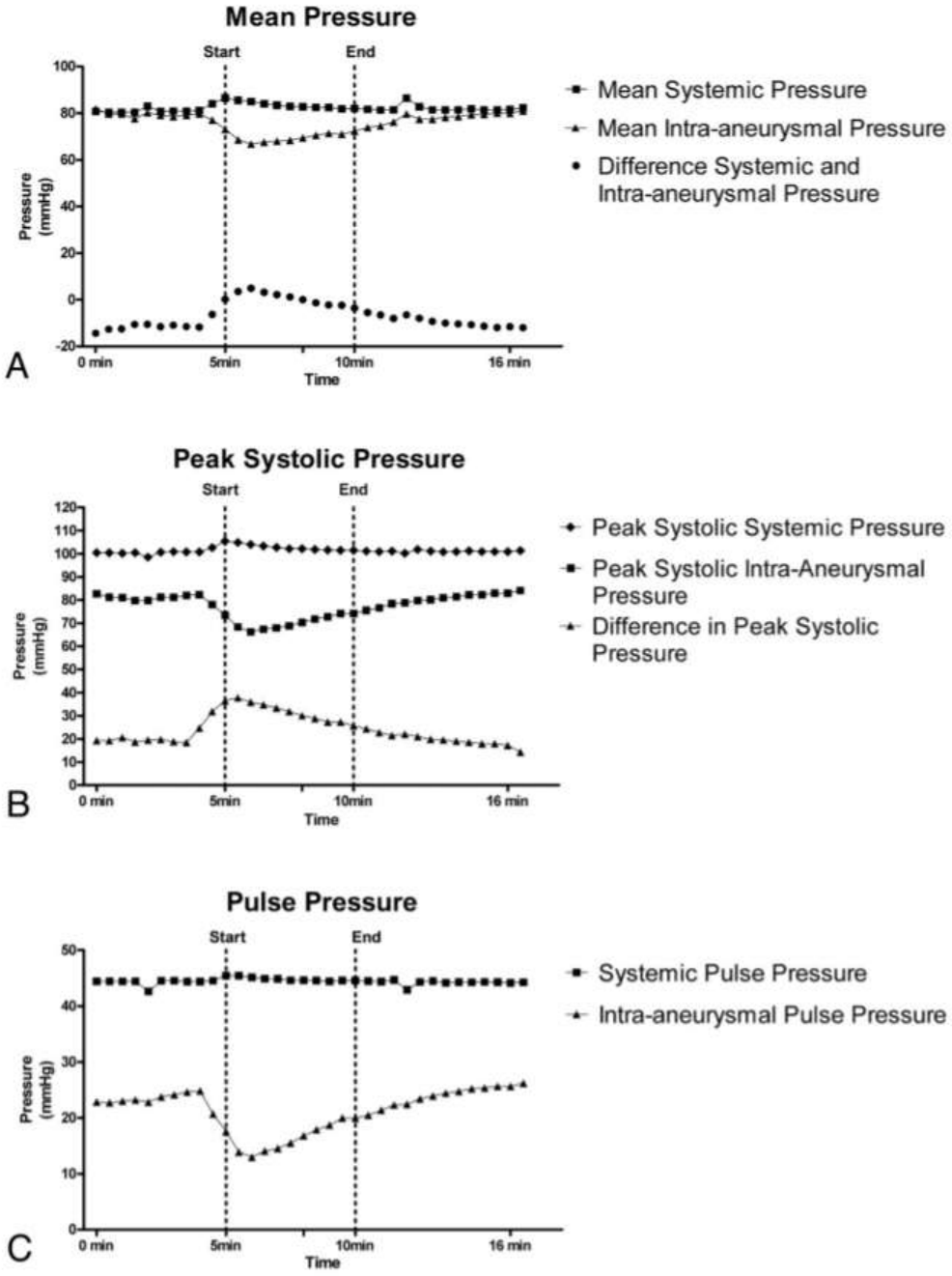

Figure 3.3: Systemic and intra-aneurysmal pressure measurements during stent deployment (adopted from 42], J.J. Schneider et al)

A: Mean pressure, B: Peak Systolic pressure, C: Pulse pressure

Cavalcanti et al [47] and his colleagues use nanorobots and nanoelectronics in advance medicine where they use a platform architecture to navigate the nanorobots for intracranial prognosis and thereby integrate it with medical instrumentation. The study further incorporated proteomics, nanobioelectronics and electromagnetics along with medical nanorobotics. The nanorobots are designed to search for overexpression of a protein so as to identify the initial stages of an aneurysm. An advanced 3D task based, nanomechatronics simulator is implemented for the device prototype and this proposed model provides details on how a nanorobot can help in early detection of brain aneurysm. An optical force sensor is developed by Nagano and Fujimoto [48]. The sensor detects the insertion force of the guidewire by measuring the deflection amount. The optical sensing system consists of a LED, photo line sensor, lens array. The sensor body is made of transparent resin to enable LED light transmission. The optical piece is embedded in the watertight resin. The light from the LED passes the sensor body and the lens array and is directed to the photo line sensor. The wire blocks a portion of the LED light and based on the pd identification the deflection of the wire and thereby the insertion force is measured.

In the last decade, considerable focus has been done on micro-force sensing due to the requirements of automation in micromanipulation

processes. To increase the sensitivity of the sensors, cantilever beams are implemented in several sensing structures, like atomic force microscopy (AFM) with their major limitation being the flexibility and dynamic range for micro-scale. Dynamic range can be improved in macro-scale by using force balancing but however very few sensors are available for micro-scale. In the recent years, piezoelectric materials have been investigated as smart structures for sensing and actuating. In a recent work, a closed-loop optimal control-enabled composite cantilever beam [4] PolyVinyliDene Fluoride (PVDF) sensor and actuator with better dynamic range and micromanipulation. With all these advances, to our best knowledge, there is still no micro-pressure sensor available to measure pressure changes in the intracranial aneurysms.

The major limitations in all the above available implantable pressure sensors are: suturing of the sensor on the aneurysmal wall; sensors sutured with a stiff stent that cannot be navigated inside the tortuous anatomy of brain blood vessels; and their larger size to place in the intracranial aneurysms. Along with that, the complication rate and its unknown cause with rupture of aneurysms after the deployment of flow diverting stent urges the need for a passive pressure sensing device that can be implanted inside the brain aneurysm after flow-diverting stent placement, to monitor pressure changes, if present, inside the aneurysm.

Chapter 4

Bio–Inspired Sensor and Sensing Principles

This work is on designing a self-power pressure sensor device that can be deployed within the aneurysm. This work will focus on designing a pressure sensor device that can be implanted inside the intracranial aneurysm, during flow diverting treatment, which is small in size, and which is very sensitive to small changes in pressure, passively operated and that can transmit the signal wirelessly. The deployment will be similar to the deployment of endosaccular devices. This sensor once deployed can be operated remotely outside and the pressure changes inside the aneurysm can be monitored remotely as shown in the below Figure 4.1.

Figure 4.1 shows a broad view of the proposed work where the sensor is implanted inside the aneurysm with the flow diverting stent. The sensor can be operated passively and the data can be transmitted wirelessly,

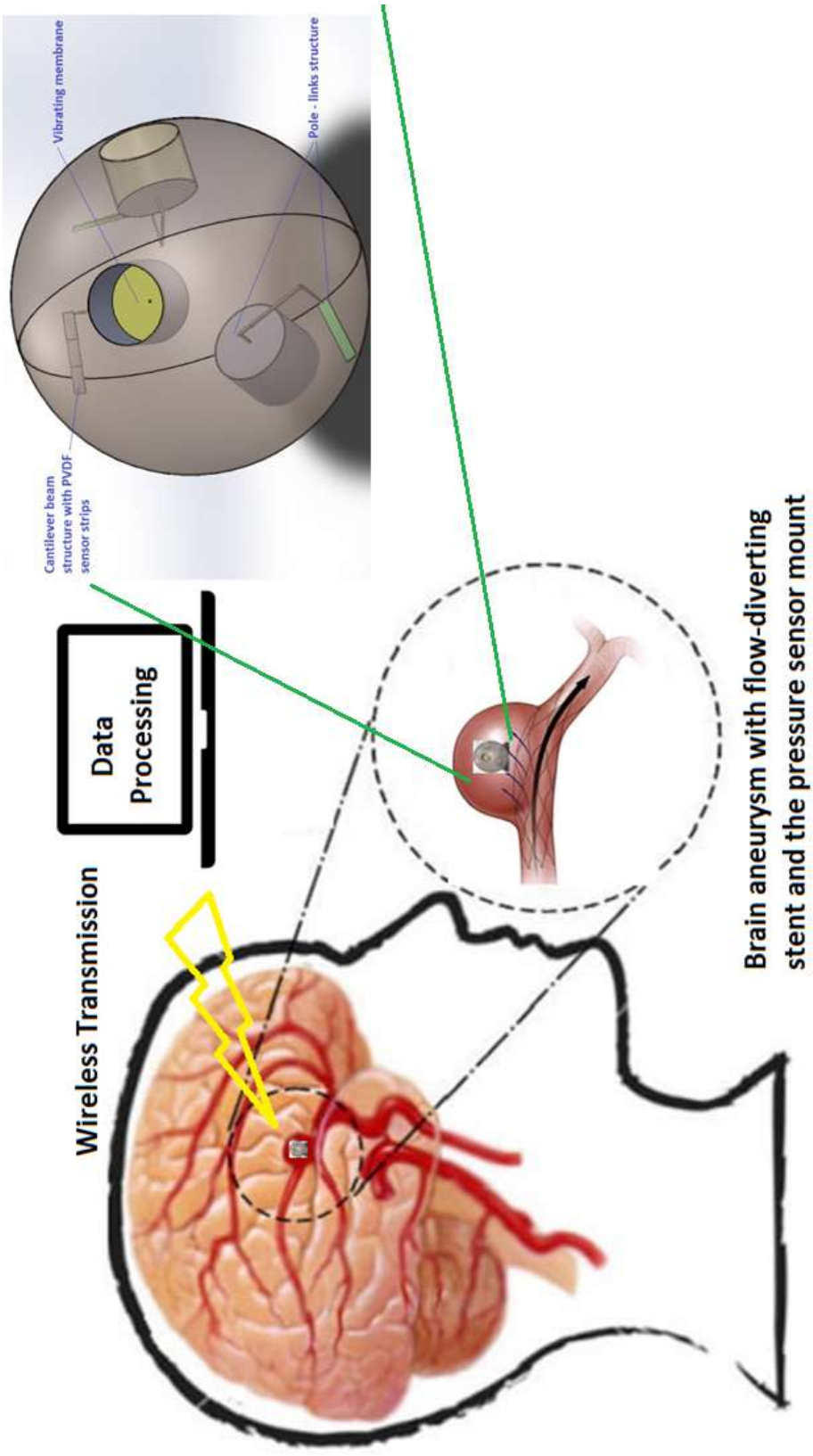

Figure 4.1: A complete picture of the entire setup

where the data is received in the handheld RF reader and post-processed to read the pressure changes on a computer.

The initial step is the actual mounting device that has to be mounted inside the aneurysm, as shown in figure 4.1, with three sensors units for redundancy and accuracy by averaging the output data. The mounting device itself is aimed at being less than 1 cm in diameter but however, for the dissertation work, it is designed in a macro-scale to prove the concept.

The rest of the chapter discusses the theory and principle behind each part of the pressure sensor unit. It starts with discussion on the theory and principle of the ear hearing, piezoresistive and piezoelectricity (for sensors), discussion on the proposed self-power consumption and digitalization of the output signal, followed by presentation and discussion of the bio-inspired pressure sensor unit design.

4.1 Bio-Inspiration from Ear Hearing Mechanism

The design is extended by incorporating the operating mechanism of the human ear.

4.1.1 External Ear Mechanism

The external ear, as shown in Figure 4.2, comprises of the pinna, ear canal and the tympanic membrane. The shape of the head and the upper torso,

along with the locations and shapes of the pinnae allows some sound waves to be reflected into the ear canal, while attenuating the others. The mid and high frequency regions of the sound are the primary waves that penetrate the canal due to the relatively small dimensions of the pinna compared to the sound wavelengths [52]. Low frequency sounds with longer wavelengths are diffracted away. The sound waves that enters the pinna are further altered by the resonances of the ear canal, due to the presence of the ridges and soft tissues. It is altered in such a way that some frequencies are amplified, relative to others; and those that get amplified are important to human communication and behavior.

Once the sound waves make way through the ear canal, the ear canal acts as ¼ wavelength resonator [52] on the sound waves and increase those sound pressure waves that have a wavelength four times the length of the tube and any odd whole multiple of the wavelength, at the blocked end of the tube. The ear canal being approximately 30 mm long and approximating the ear canal as a uniform cross-sectional cylinder, the average ear canal would increase sound waves around 2833 Hz. However, since it is a soft tissue with non-uniform cross-section, the peak of resonance occurs between 2000 to 3000 Hz, which corresponds to 15 to 20 decibels [52]. This is the region corresponding to speech communication.

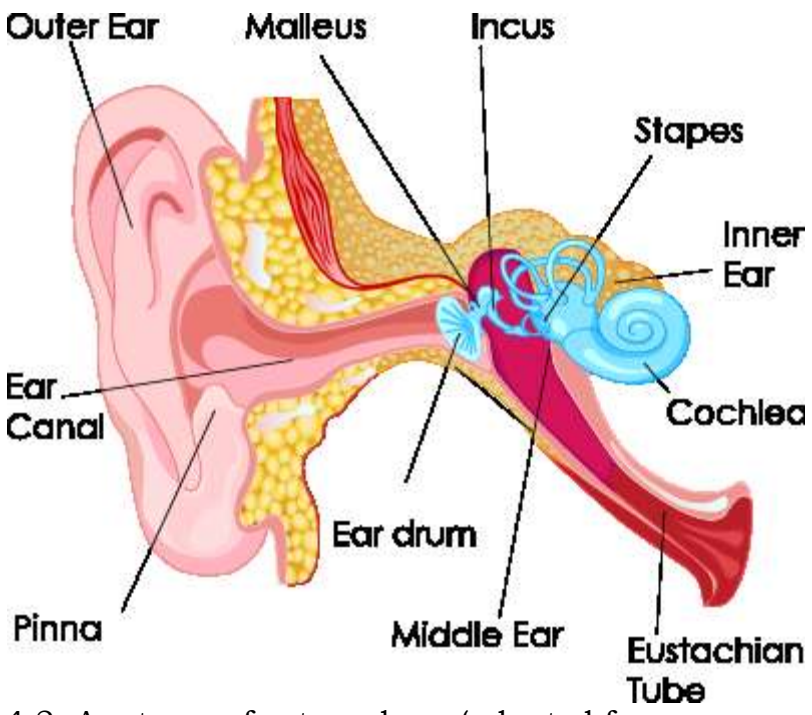

Figure 4.2: Anatomy of external ear (adopted from www.nacd.org)

4.1.2 Middle Ear Mechanism

The middle ear as shown in the Figure 4.3, consists of three small bones – malleus, incus and stapes [50]. These three bones are the smallest in human body and together are the size of a finger nail. The main purpose of the middle ear is to provide impedance matching between the air-filled external ear and fluid-filled inner ear.

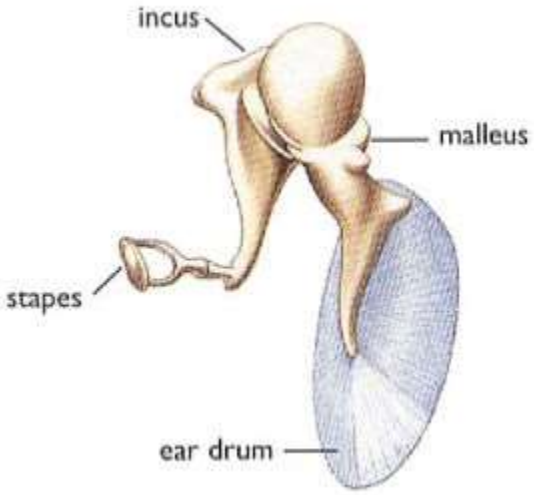

Figure 4.3: Anatomy of the middle ear (adopted from www.naturalhistory.si.edu)

The sound wave that reach the tympanic membrane gets converted into physical vibrations of the ossicular chain. The ossicular chain connects the tympanic membrane to the oval window of the inner ear, thereby providing an anatomical bridge between the external and inner ears.

The acoustic impedance of air in the ear canal is the normalized characteristic impedance of air, to the cross-sectional area of the ear canal. The impedance in ear canal approximates to 100 acoustic Ω [52]. The power transmission index from the ear canal to the tympanic membrane is approximately 0.75 [52]. The impedance of the tympanic membrane is 300 acoustic Ω [52], thus leading to an impedance ratio of the inner ear fluid to tympanic membrane being 4000 approximately.

For efficient energy transmission from the external to the inner ear, proper and efficient impedance matching is needed. The middle ear provides this matching by increasing the pressure between the tympanic membrane and the inner ear by approximately 36 dB. The impedance matching is done by area ratio transformation and ossicular chain level action.

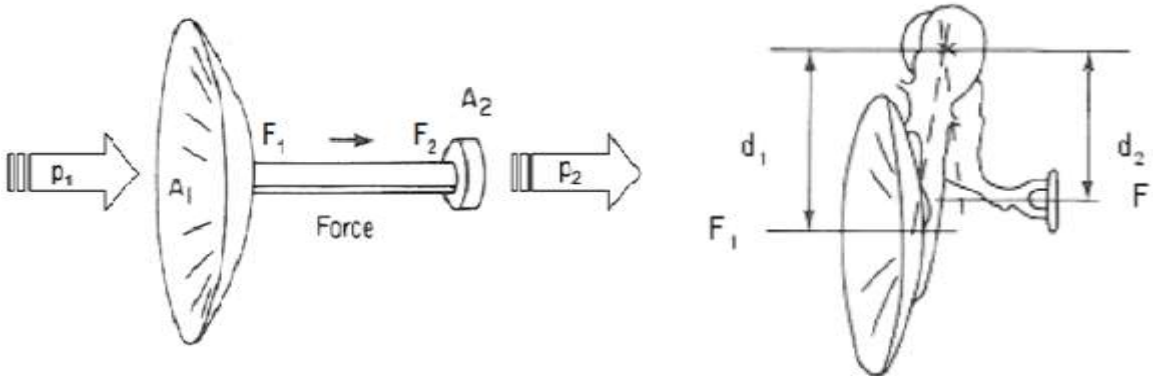

Figure 4.4: Area ratio transformation and Ossicular chain transformation (adopted from Auditory Function, Diana C. Emanuel et al)

The area ratio transformation [52] results from the difference in the cross-sectional surface area between the tympanic membrane and the oval window membrane, as shown in Figure 4.4. When a pressure p_1 acting on the tympanic membrane results in a force F_1 ; and assuming that the ossicular chain is a lossless system, the corresponding force F_2, acting on the oval window will be similar to F_1, such that,

$$F = p_1 * A_1 = p_2 * A_2 \Longrightarrow\ p_2 = p_1 * \frac{A_1}{A_2} \qquad (4.1)$$

Since the cross-sectional surface area of the tympanic membrane (A_1= 55 sq.mm) is 17.2 times larger than the cross-sectional surface area of the

oval window membrane (A_2= 3.2 sq.mm); it results in a corresponding increase in sound pressure level by 17.2 times on the oval window. This 17.2 times increase correspond to 25 dB of SPL increase.

The ossicular chains in the middle ear provide a lever action, by the rotational motion of the malleus and stapes.

The level arrangement [52] creates a fulcrum with incus and a rotational motion with malleus and stapes. The level mechanism is shown in Figure 4.4. In the lever, a force F_1 on the arm at a distance d_1, results in a corresponding force of F_2 on the effort arm at a distance of d_2, such that.

$$F_1 * d_1 = F_2 * d_2 \quad (4.2)$$

Forces F_1 and F_2 are the forces acting on malleus and stapes and the distances d_1 and d_2 are the lengths of the malleus and incus respectively. The length of the malleus is 1.3 times longer than the length of the incus and this causes an increase in force by 1.3 times, which corresponds to an approximate 2 dB increase in SPL. This along with the area ratio transformation account for an overall of 32 to 33 dB increase in SPL and an effective impedance matching.

Currently, a middle-ear prosthesis to treat middle ear pathology is available in the market. KURZ technology has developed Titanium Tympanoplasty Prosthesis [51] enabling partial and full ossicular reconstructions. The prosthesis uses the area amplification alone which accounts for the 18.6 times amplification.

Figure 4.5 shows the ear and KURZ Tympanoplasty Prosthesis [51] where L varies from 3mm to 7mm. To further study the biomechanics, a finite element model study was done where four different middle ear prostheses were used to compare and study the impedance matching. All four prostheses had a close to normal vibrations on both the tympanic membrane and inner ear, suggesting that these prostheses have an impedance matching close to normal. Also, this study suggest that the middle ear does the impedance matching as the vibrations on external and inner ear is similar.

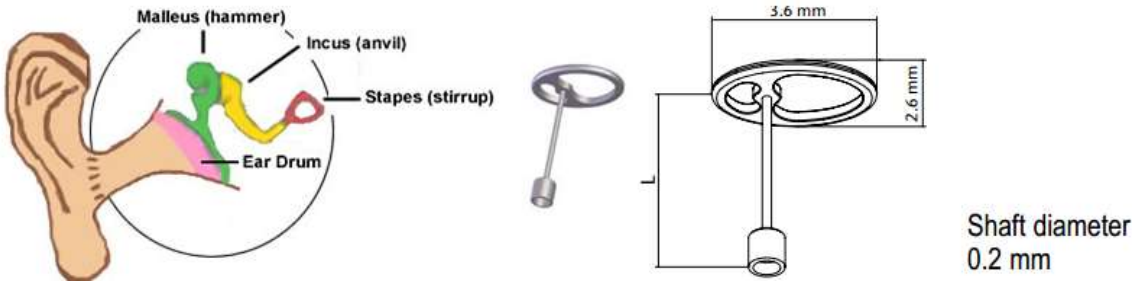

Figure 4.5: External and middle ear; KURZ Tymphanoplasty (adopted from [51])

4.1.3 Inner Ear Mechanism

The primary part of the inner human ear is the fluid-filled coiled cochlea which is lined with hair cells, which upon vibrations, causes a movement of the hair cells. This generates electrical nerve impulses which is transmitted to the brain.

The main role of the cochlea [52] is to convert the mechanical vibrations of the stapes to electrical impulses. These impulses are transmitted to the

auditory cortex of the brain by the auditory nervous system, for sound perception. The cochlea does this conversion in stages with the first stage being the conversion of the stapes motion into the motion of the fluids within the cochlea, thereby generating a traveling wave motion along the basilar membrane.

The inward and outward motion of the stapes on the oval window of the inner ear, creates a traveling wave motion along the basilar membrane. The basilar membrane is systematic arranged in such a way that it responds differently to sound stimuli of different frequencies, making the location where it reaches the maximum displacement depend on the frequency. This systemic shift of maximum vibration goes from apex to base as frequency increases. This maximum displacement induces movement of the outer and inner hair cells.

The outer hair cells amplify, while the inner hair cells are sensory receptor cells. They cause the release of the neurotransmitter into the auditory nervous system which gets transmitted into the auditory cortex, for sound perception.

4.2 Piezoresistive Sensing Principle

Piezoresistivity [55] is change in resistance when mechanically stressed. Piezoresistive effect dates back to 1856 when Lord Kelvin noted the

resistance change when metal devices where mechanically strained. This change in resistance can happen in two ways. First, the dimensions of the device changes with strain change. One such application is the strain gauge. Second, when mechanically strained, the resistivity of the material itself changes. One such application is the piezoresistor. Piezoresistors are semiconductor silicon.

Resistance is the measure of charge carrying density. When the resistance changes, it causes the change in the number and mobility of the charge carriers. The change of resistance with piezoresistors are higher than the strain gauges.

Piezoresistive sensors can be made extremely small by micromachining. They have been used in medicine [55] to be implanted inside the body tissue to measure the stresses. They can be made into small strain gauges to measures very low stresses being generated. They can be fabricated in a wide range.

Piezoresistive sensors [55] have high sensitivity of the order of 10mV/V and shows linearity at constant temperature, without hysteresis. One major disadvantage is temperature dependence of 1%/Kelvin, drift with temperature and initial offset of 100% or more.

With these principle and concept, in order to increase the sensitivity,

accuracy and reliability, our proposed sensor design consists of dividing the active resistor area into smaller equally spaced independent channels. For the dissertation work, a piezoresistive sensor 2.2” long is used.

The sensor is made of a thin diaphragm in which resistor is embedded in an array of channels to form a variable resistor for a Wheatstone bridge. The active resistor area is divided into small 1KΩ resistors channels and conductive strips alternating, to study the distribution of strain and stress [59] from free end to the fixed end by studying the change in resistance as the pressure is applied. These sensors change in resistance depending on the amount of pressure on the sensor. When the sensor is straight, the intrinsic resistance is about 25KΩ. When the pressure is applied on the sensor, the stress increases, thereby increasing this resistance. When the sensor is undeflected upon the removal of the stress [59], the resistance returns to the original value.

Thus, when pressure is applied to the diaphragm, the electrical resistivity changes due to the mechanical stress, which is the piezoresistive effect [55]. The bridge circuit is supplied with a supply voltage of 5V. A sensor output signal proportional to pressure is generated [59]. By measuring the resistance, we can determine the pressure applied.

4.3 Piezoelectric Sensing Principle

Piezoelectricity is generation of charges when mechanically stressed. Along with that, it mechanically deforms when a voltage is applied. Piezoelectricity dates back to 1880 when Jacques and Pierre Curie discovered piezoelectric effect on quartz and tourmaline. Piezo originates from the Greek work piezein which means “to squeeze” [56]. The piezoelectric film, PVDF, comes in various thickness and lengths and is extremely light weight and flexible plastic. Its mechanical and electrical properties [56] allow it to be used a transducer with a wide frequency and dynamic range ranging between 0.001 – 109 Hz and 10.8 to 106 psi to Mbar, respectively. It has a low acoustic impedance, very similar to water and human tissue; has higher output voltage than piezo ceramics, 10 times more for the same input; high elastic compliance; high mechanical and dielectric strength; high impact resistance and highly stable. It resists moisture, most chemicals and oxidants, UV and nuclear radiation. Piezo film is highly sensitive and has low density. It can be fabricated [56] in any design and can be glued using any commercially available adhesives directly onto any structure without changing or influencing the mechanics of the structure. Piezoelectric sensors are highly suitable for sensing applications.

Biological polymers exhibit piezoelectric effect. Along with piezoelectric,

they exhibit pyroelectric and electro-optical effect [56]. Biological materials like bone, cellulose and a wide variety of polysaccharides show piezoelectric effect. These materials have gained high interest in research field due to their biocompatibility and biodegradability abilities [56]. The naturally occurring materials that exhibit piezoelectric effect apart from quartz and tourmaline are; silk, Topaz, Rochelle salt, tendon, wood, dentin, DNA, enamel and more.

In the crystal classes [57], 21 out of 23 crystal structures show non-centrosymmetry. Of them, 20 exhibit piezoelectricity [57]. Ten of them belong to polar crystal classes, and they exhibit spontaneous polarization without mechanical stress due to the presence of an inherent dipole moment associated with their unit cell. Piezoelectric effect is manifested on these non-zero polarization crystals, when mechanically stressed, by inducing a change in polarization.

For the class of non-polar yet piezoelectric crystals, a polarization is manifested only on the application of the mechanical stress through a mechanical load [57]. This is done by changing the non-polar crystals to polar crystals by mechanically stressing them.

Kawai found very high piezoelectric activity in the fluoropolymer, polyvinylidene fluoride (PVDF), in 1969. PVDF and its copolymers exhibited a very high piezoelectric effect [57].

PolyVinyliDene Fluoride (PVDF) is a polymer and is made up of long repeating chains of the monomer (—CH2—CF2—) [58]. The positive hydrogen atoms and the negative fluorine atoms, with respect to the associated carbon atoms, together hold a dipole moment, for every monomer. In the liquid state, the polymer chains are in random orientation and so the dipoles cancel out each other. This results in a zero-dipole moment. PVDF film [58] is solidified, stretched in a certain direction and poled. Upon stretching [58], the polymer chains align along the direction of stretching. This provides a net polarization. When this stretching is combined with poling, where a strong DC electric field is applied, the dipoles are locked into their configuration of near alignment [58]. This imparts a permanent net dipole moment to the piezoelectric material. The poling process in case of piezo ceramic is shown in Figure 4.6.

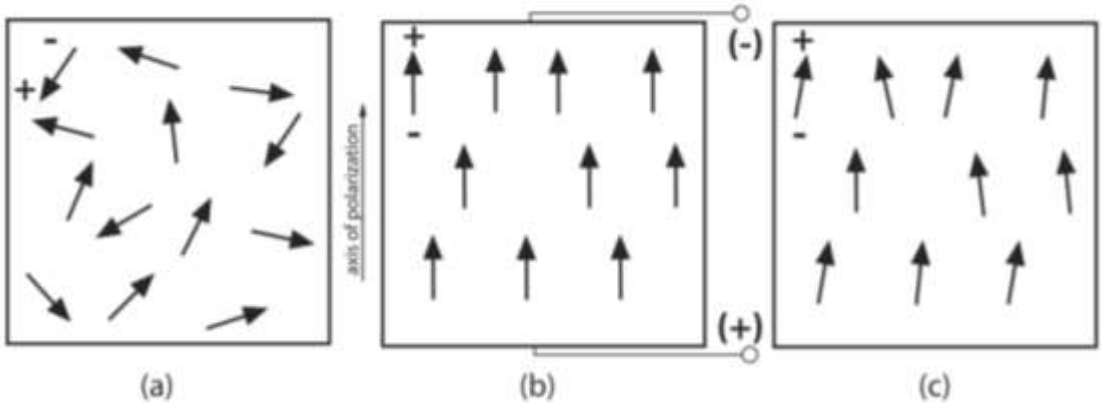

Figure 4.6: Poling process (adopted from [56])

a: Prior to polarization polar domains are oriented randomly, b: A very large DC electric field is used for polarization, c: After the DC field is removed, the remnant polarization remains.

The stretching of the piezoelectric film makes the material piezoelectrically orthotropic, which implies that $d_{31} \neq d_{32}$ [58]. However, for smaller strains, mechanically isotropic property is assumed for the material.

Mechanical stress in the form of compression or tension changes the orientation of the dipole moment. This electric displacement results in generates of a charge. Tension orthogonal to the polarization direction, and compression along the polarization direction, generates a charge, in the form of voltage, as the same polarity as the poling voltage. Tension along the polarization direction, and compression orthogonal to the polarization direction, generates a charge, in the form of voltage, as the opposite polarity as the poling voltage. It is shown in Figure 4.7. Voltages generated upon the stress is linearly proportional to the stress. The material operated in this manner is used in sensing setup.

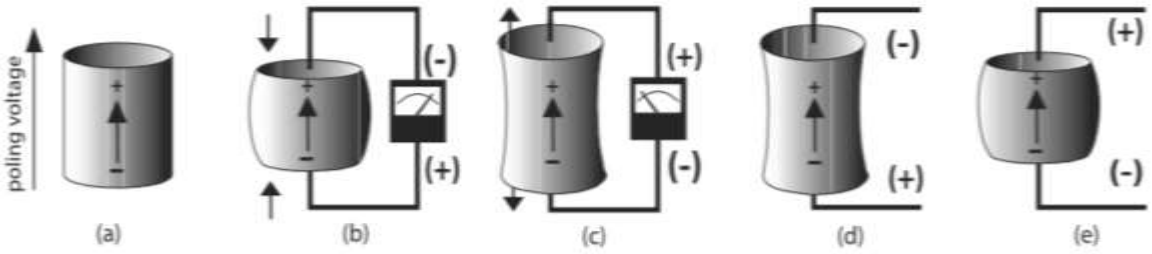

Figure 4.7: Reaction of a poled piezoelectric element to applied stimuli (adopted from [56])

4.4 Our Bio-Inspired Pressure Sensor

The design [59,60,61] includes three pressure sensors structures in cantilever design, inserted inside the mount in three directions for redundancy so that it can measure changes in pressure from any direction at any point of time, as shown in Figure 4.1. However, the design is in such a way that the sensor is not in direct contact with the surroundings. The entire mount has three openings in 3 directions with a vibrating membrane.

This vibrating membrane will be a biocompatible one that vibrates to any intraaneurysmal pressure changes. This vibration will cause displacement of the cantilever beam. For this dissertation work, only one pressure sensor unit is designed and tested.

The design includes three piezoelectric PolyVinyliDene Fluoride (PVDF) pressure sensors structures in cantilever design, inserted inside the sensor unit in three directions to measure changes in pressure from any direction at any point of time, by measuring the change in the voltage output.

The output voltage can be transferred via wirelessly (outside the scope of the work) using RFID transmission by winding RFID coil around the micro-mount. However, the output voltage from the piezoelectric sensor will only

be in the order of mVolts for the experienced pressure changes. To amplify the input dynamic pressure, an amplification mechanism is implemented between the input pressure and sensor.

4.4.1 Sensor Features: Ear Hearing Bio-Inspiration

The work focusses on designing the pressure sensor unit by incorporating the human ear mechanics benefits as shown in Figure 4.8. The human ear receives the sound pressure waves through the ear canal. The pressure waves are converted into physical vibrations when it hits the tymphanic membrane. This physical energy is amplified by the three small bones in the middle ear and transferred to the inner ear, where it is converted to electric impulses to be transferred to the brain for sound interpretation.

The design consists of the vibrating membrane which vibrates to the intraaneurysmal pressure changes. The vibrations are transferred to the striped sensing beam through the three pole-links structure similar to the three bones of the middle ear to provide amplification.

The bio-inspired pressure unit corresponding to the human ear structure is shown in the Figure 4.8. The design utilizes the ear mechanics benefits by consisting of the circular vibrating membrane which vibrates based on the intraaneursymal pressure changes.

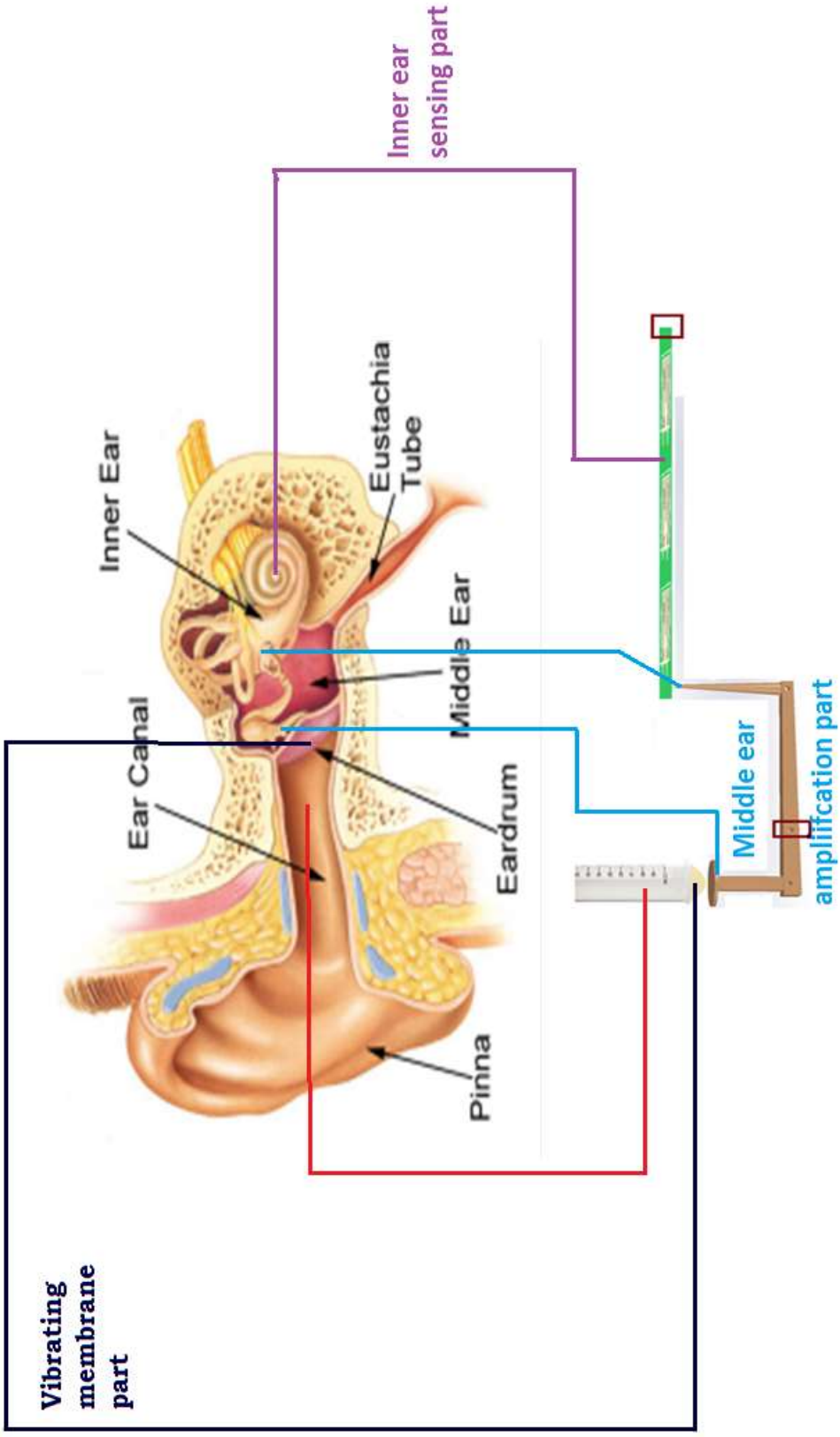

Figure 4.8: Bio – inspired pressure sensing unit

This mimic the tympanic membrane part of the ear. The other side of the vibrating membrane is connected to three pole-links structures similar to the three bones of the middle ear to perform the middle ear's leverage mechanism.

The composite cantilever beam structure with the sensor strips mimics the coiled cochlea of the inner ear, in elongated form. This piezoelectric sensor strips are responsible for the passive mechanoelectrical conversion and generation of electric voltage, for the intraaneursymal pressure change application.

The surface area of the vibrating membrane is made > 3 times larger than that of the circular part of the last link which deflects the tip of the cantilever beam, upon pressure.

4.4.2 Sensor Features: Self-Power Consumption

This part proposes the next step of how the dynamic signal (voltage) (if seen) generated by the piezo sensors gets converted back to the variations (if seen) of the blood pressure inside the aneurysm. To account for that, each piezo sensor's output can be connected to a microchip, which can have in-built functionalities of analog-to-digital conversion and in-built memory that stores these digital signals. The power required for the micro-chip can be passively generated and supplied by the PVDF layer beneath the beam for its length as in Figure 4.9.

For every deflection caused on the beams, the PVDF strips on the top layer are responsible for detecting the deflection and the PVDF below the beam is responsible for powering up the micro-chip. The micro-chip gets output signals from all three beams, digitizes and stores in the memory.

Figure 4.9: Self power consumption with a PVDF layer below the beam

4.4.3 Sensor Features: Digitalization of the Sensing Beam

The design continues to adopt the digitalization model where any pressure change, if present, inside the aneurysm after the flow-diverting stent placement is digitized as “1”. The minimal pressure change that is in consideration in our analysis is 10mmHg of pressure difference from the parent vessel artery.

Since the whole idea is to know if the aneurysm is facing the pressure changes as the parent vessel artery, after the stent placement, or not; a binary value of 1 or 0 per sensor for a voltage value above or below the threshold value, will be optimal. The pattern of few basic digitized

combinations is shown in the below Figure 4.10. So, from the digitized output, approximately the pressure the aneurysm is facing in comparison to the parent vessel artery can be calculated.

For instance, a “1-1-0” will correspond to an approximate 20 mmHg of pressure higher from the diastolic pressure range of the patient. Similarly, a “1-0-0” will correspond to an approximate 10 mmHg of pressure higher from the diastolic pressure range of the patient. A “1-1-1” will correspond to approximately equal to or closer to the systolic pressure range of the patient.

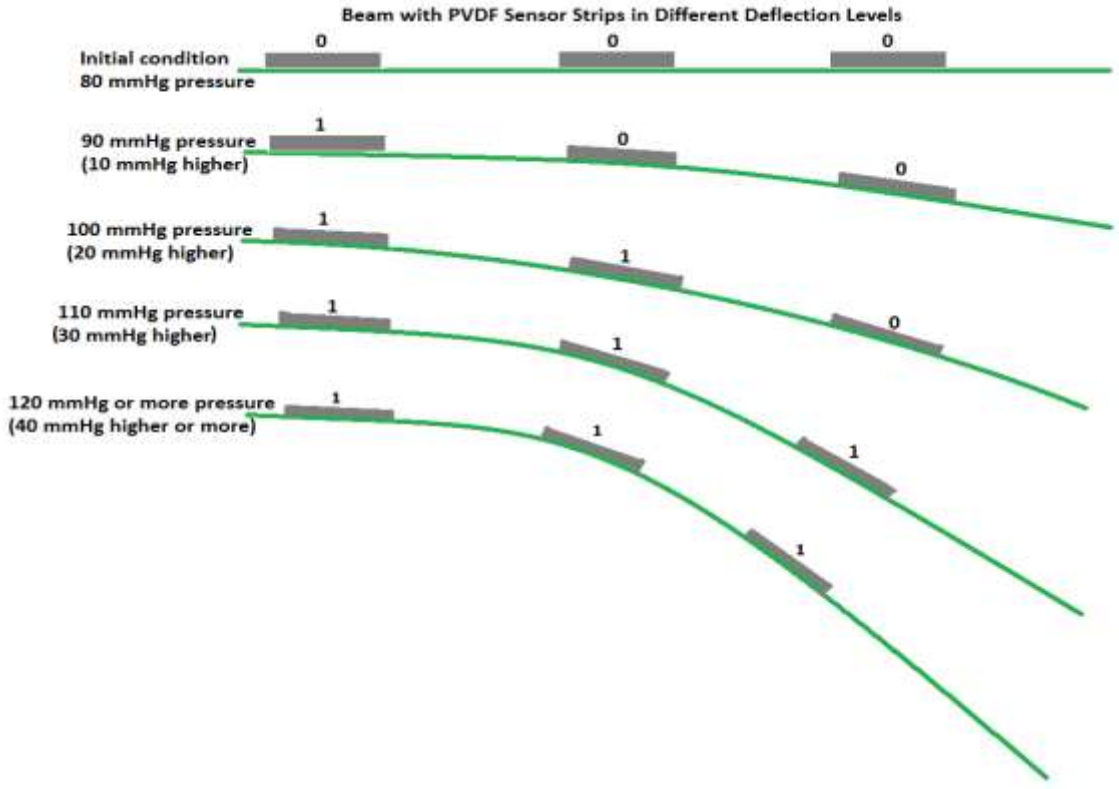

Figure 4.10: Digitization of output voltages from the PVDF Sensor Strips upon deflection

An experimental analysis is done with the mechanical structure design, where pressure is increased in steps of 10 mmHg from the initial 80 mmHg pressure to 120 mmHg and then decreased back to 80 mmHg pressure. The sensor output voltages corresponding to this step increase and decrease is shown in the below Figure 4.11.

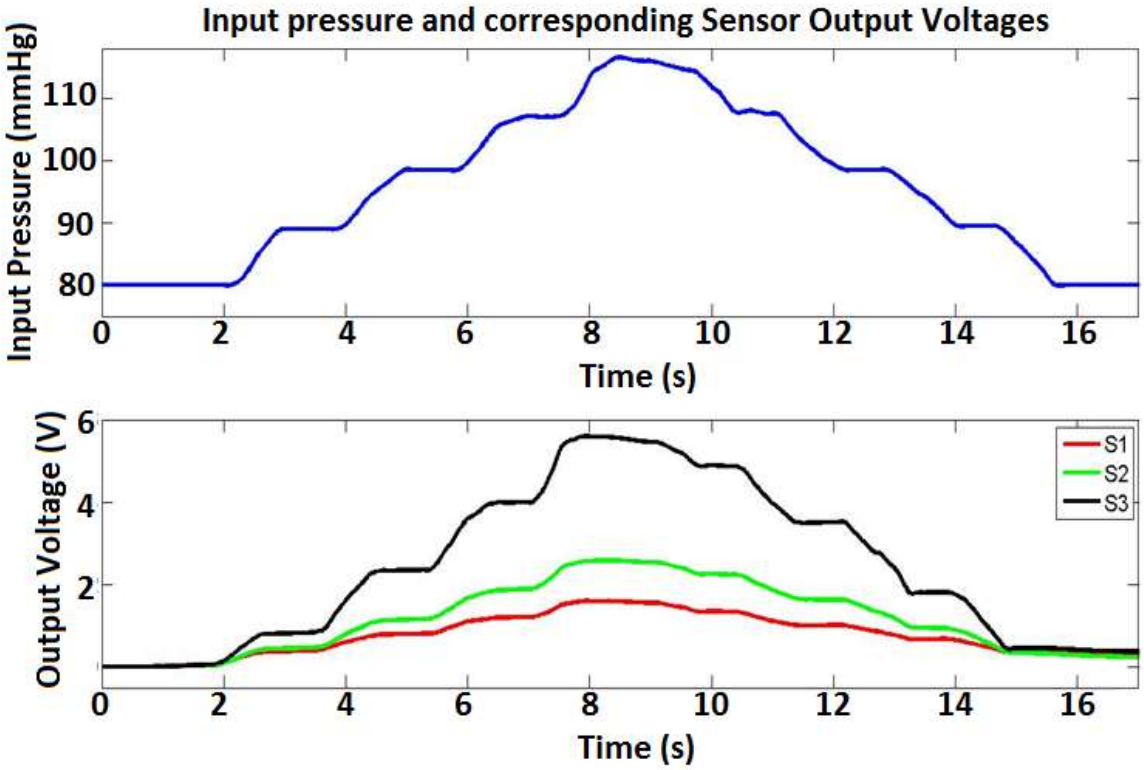

Figure 4.11: PVDF Sensor output voltages corresponding step increase in input pressure

The minimal pressure change of 10 mmHg inside the aneurysm causes a small deflection, which according to the plot generates approximately 1V of output voltage from sensor 3 (S3 – towards clamped end) and a voltage lower in the other two sensors. Voltage of 1V and higher when digitized to

a “1” and voltage less than 1V digitized to a “0”, will contribute to the presence of any pressure change inside the aneurysm. From the experimental analysis, the threshold voltage to be set can be 1V. The test is repeated several times to test the reliability and consistency of the results.

4.5 Testing Setup

The below Figure 4.12 shows the complete setup for the experimental analysis. The dual syringe setup is setup to mimic the arteries and an initial pressure of 80 mmHg is set in the fluid inside the syringes to mimic the base pressure of the blood vessels in the human body. The input force is applied using the force meter FG – 3006 and the corresponding pressure is monitored on the sphygmomanometer. All the force applied in our analyses correspond to 40 – 50 mmHg of change in pressure.

The vibrating membrane correspond to the tympanic membrane of the external ear. The mechanical structure is placed on the other end of the vibrating membrane. This mechanical structure consists of the three parts – pole, horizontal link and the vertical link. These three parts together correspond to the middle ear.

The cross-sectional surface area difference of 2.7 times between the pole and vertical link tip and the 1:3 ratio of the mount (fulcrum) on the

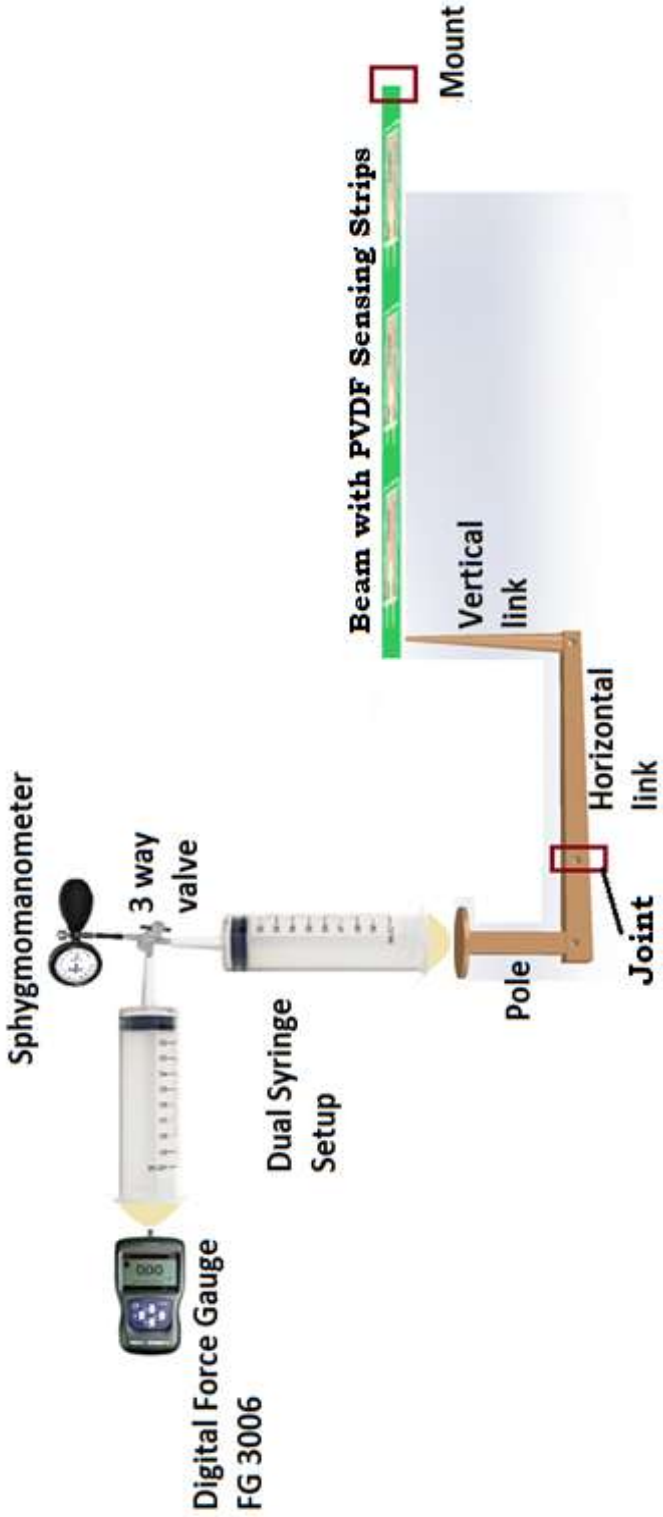

Figure 4.12: Block diagram for testing setup of the bio-inspired pressure sensor

horizontal link, provide approximately 6 times amplification in the displacement of the beam. The beam mounted in cantilever form hosts the three PVDF sensor strips. This correspond to the inner ear which generate electric impulses. The displacement of the vibrating membrane due to input force, causes amplified displacement of the mechanical structure which further displaces (deflects) the cantilever beam. This deflection generates stress in the PVDF sensor strips and according to the direct piezoelectric property, a voltage corresponding to the stress generated is developed across the PVDF sensor strips.

4.6 Other Potential Applications

Other potential applications of this device can be pressure measurement inside the aneurysm under any endovascular treatment option, intra abdominal aneurysm pressure measurement, pulmonary artery pressure measurement, intervertebral disk pressure measurement following disk prosthesis, joint pressure measurement following joint prosthesis, pressure undersea – a warning tool for volcanoes or earthquakes, pressure measurement inside building wall or inside bridge – a warning tool and more.

Chapter 5

Bio-Inspired Mechanical Amplification Structure: Simulation and Analysis

To validate and study the proposed mechanical part of the bio-mimic pressure sensor unit, one part of the unit that mimics the middle ear structure is modelled and simulated in ANSYS. The structure is shown in Figure 5.1. For initial testing purposes, the structure is enlarged to higher dimensions. In future work, it will be reduced to the micro scale.

The structure shows the circular vibrating membrane made of Silicon nitride and is approximately 60 mm in diameter. Noon et al [56] compared circular silicon nitride microphone with square silicon nitride microphone and showed that the circular one has a uniform stress distribution along the circumference of the microphone and is more sensitive than the square microphone. The pole and the links are made up of strong and flexible plastic with the horizontal link alone being a rigid part, as it is responsible for only transferring the force from pole to the vertical link.

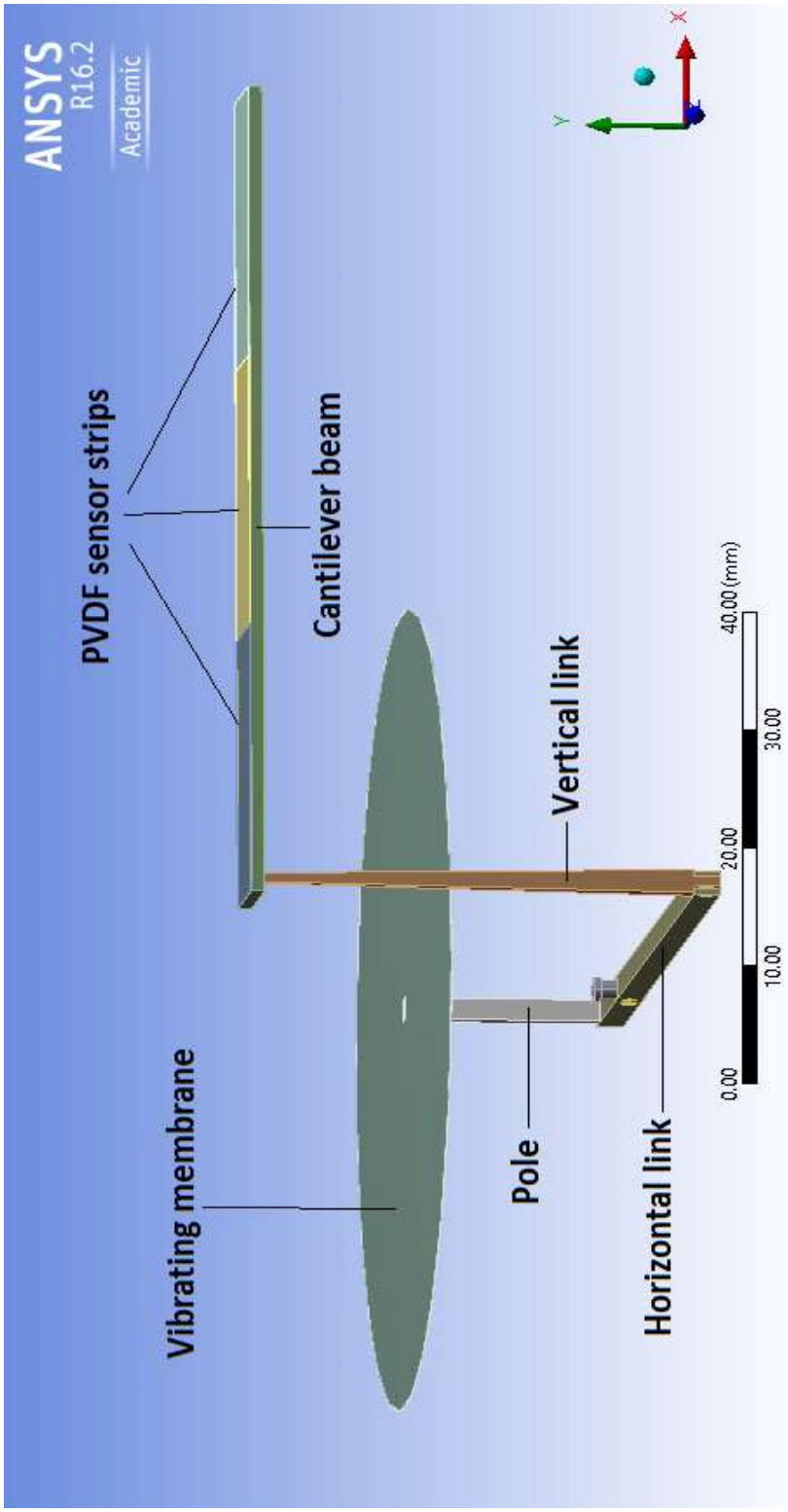

Figure 5.1: Bio – mimic ear structure part used for simulations

The cantilever beam, made of Aluminum alloy, hosts the three approximately 20mm PVDF sensor strips. Since the pressure load that the vibrating membrane will face will be the blood pressure range of humans; the pressure application range for our study will be 10KPa – 25KPa which correspond to 80mmHg – 180mmHg. Most of the simulations are done for 10KPa of input pressure.

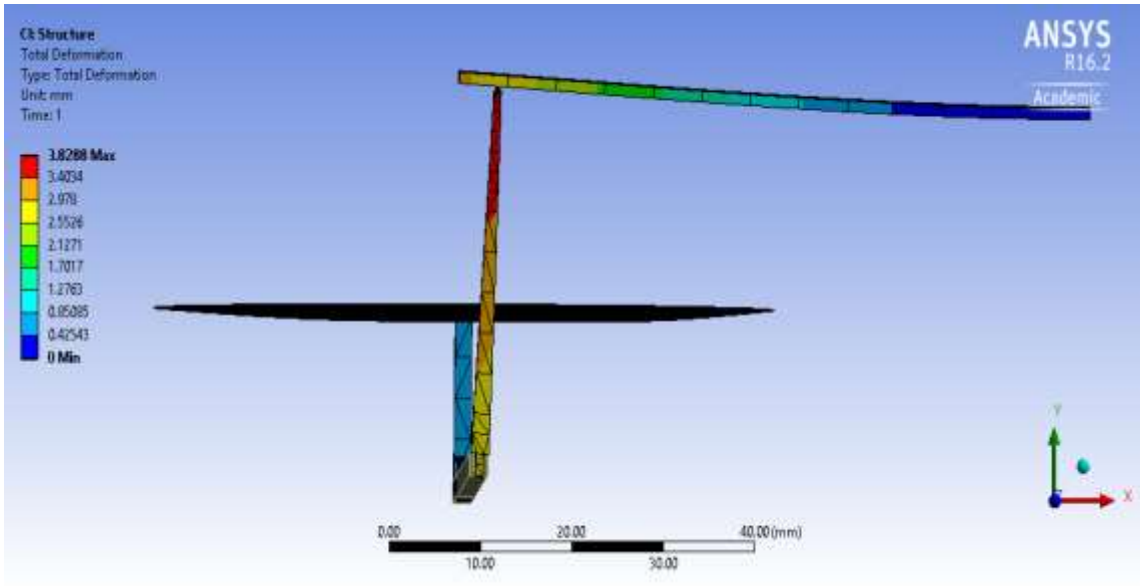

Figure 5.2: Total deformation of the structure for 25 KPa of input pressure

The material properties of the parts used for simulations are: vibrating membrane with ρ as 3100 kg/m^3 , Y as $85 * 10^9 Pa$ and γ as 0.25, similar to Silicon nitride; beam, pole and links with ρ as$1.39 * 10^3 kg/m^3$, Y as $3.8 * 10^9 Pa$ and γ as 0.4, similar to plastic; electrode layers with ρ as $3 * 10^3 kg/m^3$, Y as $0.1 * 10^9 Pa$ and γ as 0.37, similar to that of silver ink; and PVDF sensor layer with ρ as $1.78 * 10^3 kg/m^3$, Y as $3 * 10^9 Pa$ and γ as 0.34.

Bonded contacts are defined between layers in the composite cantilever beam. Fixed and revolve joints are defined between diaphragm, pole and links parts.

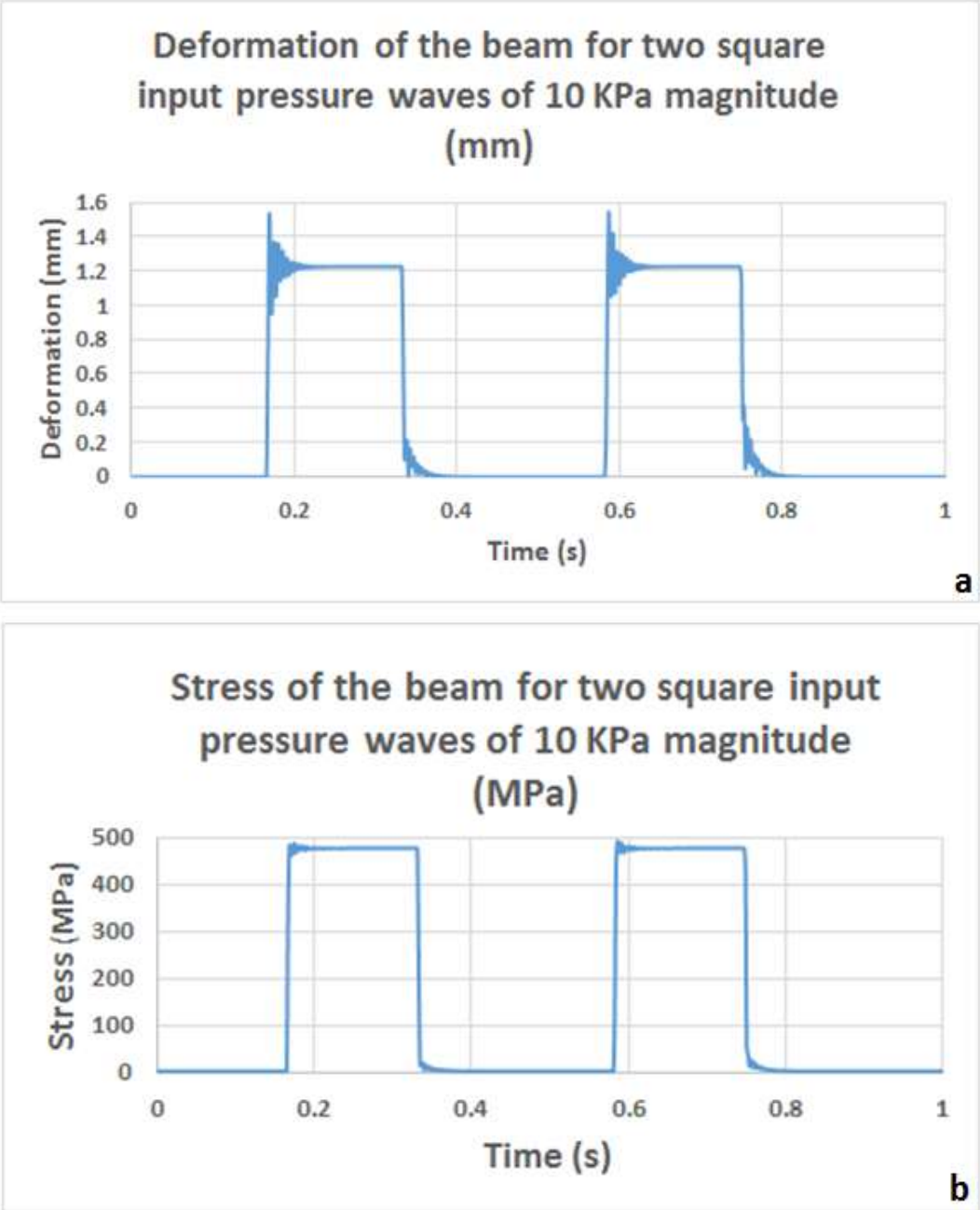

Figure 5.3: a: Deformation and, b: Stress curves for input square pressure

Simulation is done to study the mechanical movement of the structure when the pressure load is applied. The total deformation of the structure for 25 KPa of input pressure on the diaphragm is shown in Figure 5.2. The deflection of the diaphragm is transferred via the pole and links to the beam and the beam gets deflected up.

To study the dynamics of the structure, two square wave input pressure loads of 10 KPa magnitude is applied. The deformation and stress distribution curves of the beam for transient analysis are shown in Figure 5.3. The curves follow the input curve. It is also seen that the oscillations of the beam decay in less than 70ms and show the stability of the structure. It is further verified with impulse, triangle and sawtooth waves and it is seen that the deformation and stress of the structure follow the respective input curves and stability.

Further study is done to identify the optimal joint between the vertical link and the free end of the cantilever beam. The joints that are compared in our study are translational, planar and fixed joints. The constrained degrees of freedom for translational joint is UY, UZ, ROTX, ROTY, ROTZ; for planar joint is UZ, ROTX, ROTY; and for fixed joint is all. Simulation is conducted for all the above joints with rigid horizontal link and for two square wave input pressure loads of 10KPa magnitude. The deformation and stress distribution curves of the beam for transient analysis are shown

in Figure 5.4.

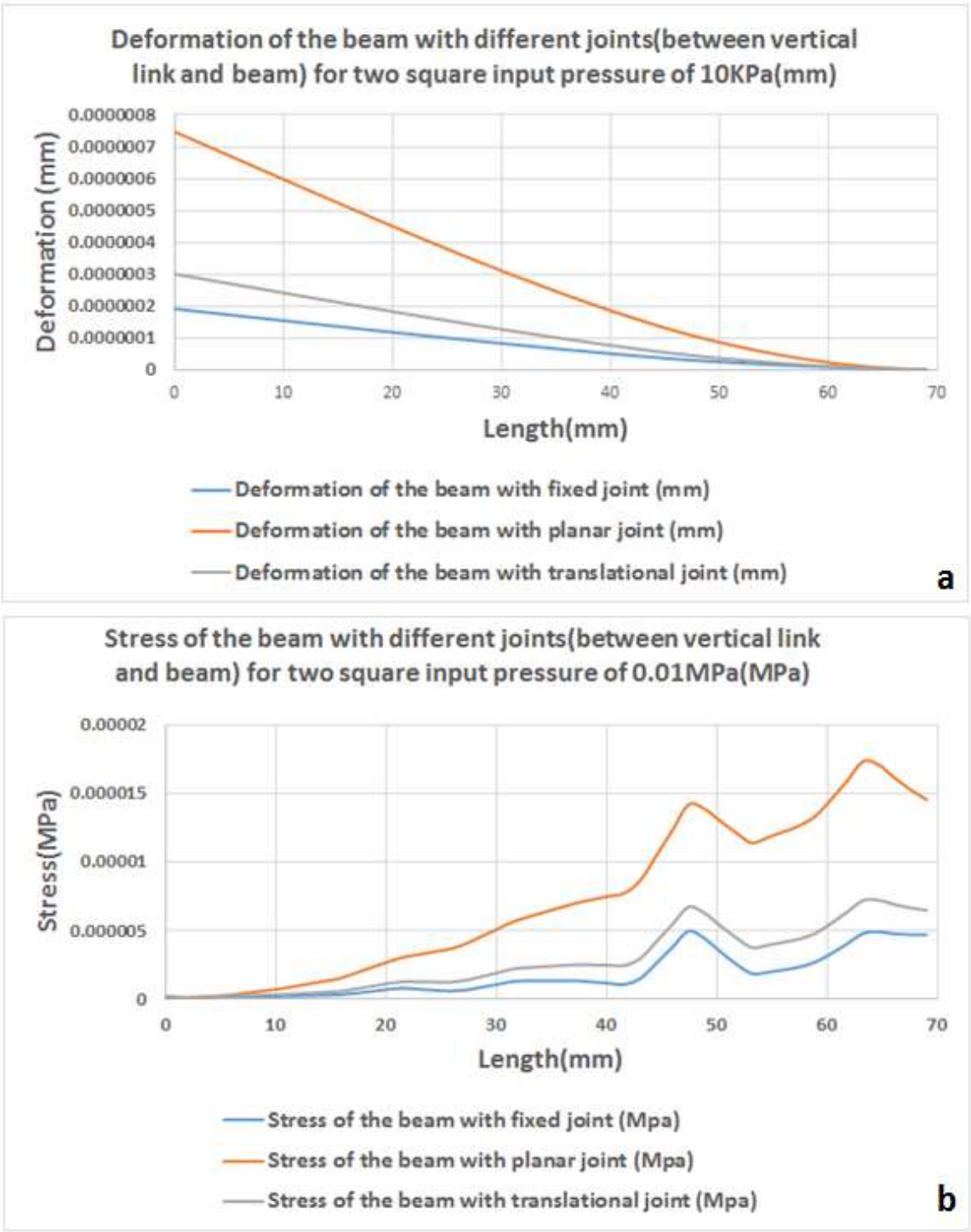

Figure 5.4: a: Deformation curve, b: Stress curve - for input square pressure waves for different joints between the vertical link and the free end of the beam

The results show a linear deformation of the beam, along the length, for all the joints with planar joint being more linear and stronger. The stress distribution of the beam, is slightly linear from the free end to half of the length, but has buckling effect on the other half of the length of the beam towards the clamped end.

To reduce the buckling effect, we propose to redesign the sensor unit by having a tapered vertical link as shown in Figure 5.5. This increases the surface area ratio transformation between the vibrating membrane and that of the tapered end of the vertical link more thereby contributing more to the amplification part of the structure and reduction of the buckling effect. The altered design is shown in Figures 5.5 and 5.6.

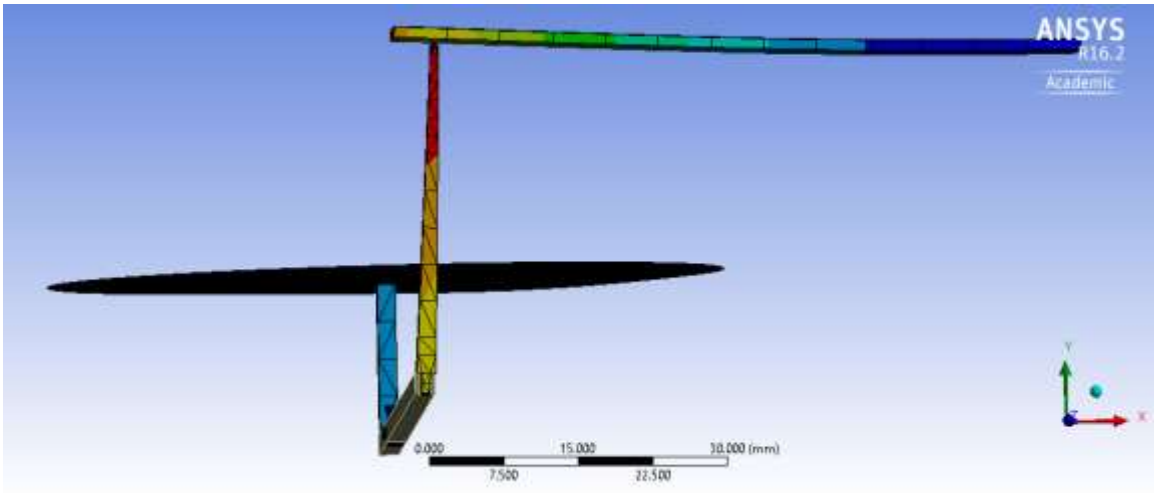

Figure 5.5: The altered design with tapered end of the vertical link

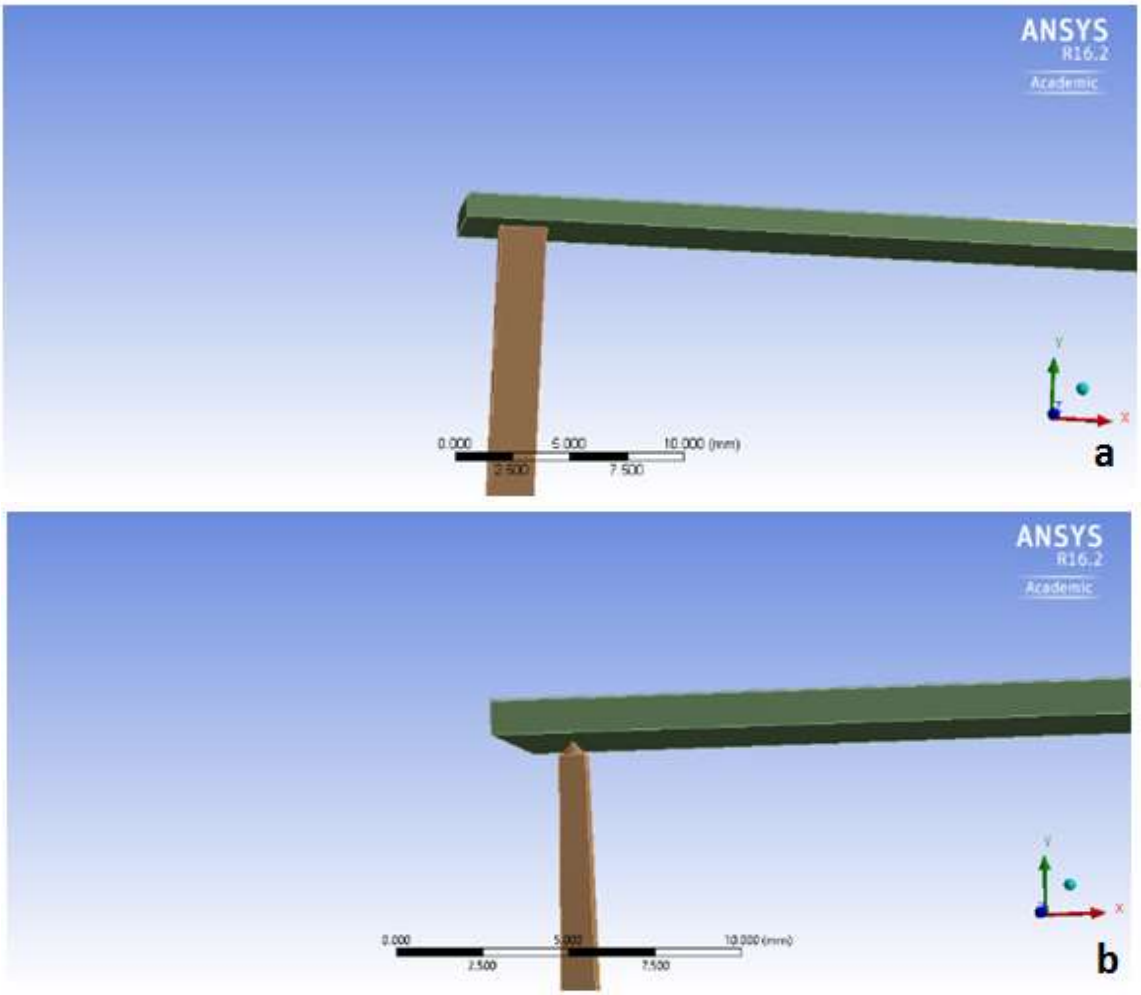

Figure 5.6: a: Zoomed comparison of the flat end of the link; b: Zoomed comparison of the tapered end of the link

The deformation and the stress distribution of the structure with the tapered end of the vertical link for planar and translational joints between the vertical link and free end of the beam are shown in Figure 5.7. Due to the tapered tip, the magnitude of the deformation and stress has increased. The buckling effect for both the planar and translational joints have reduced.

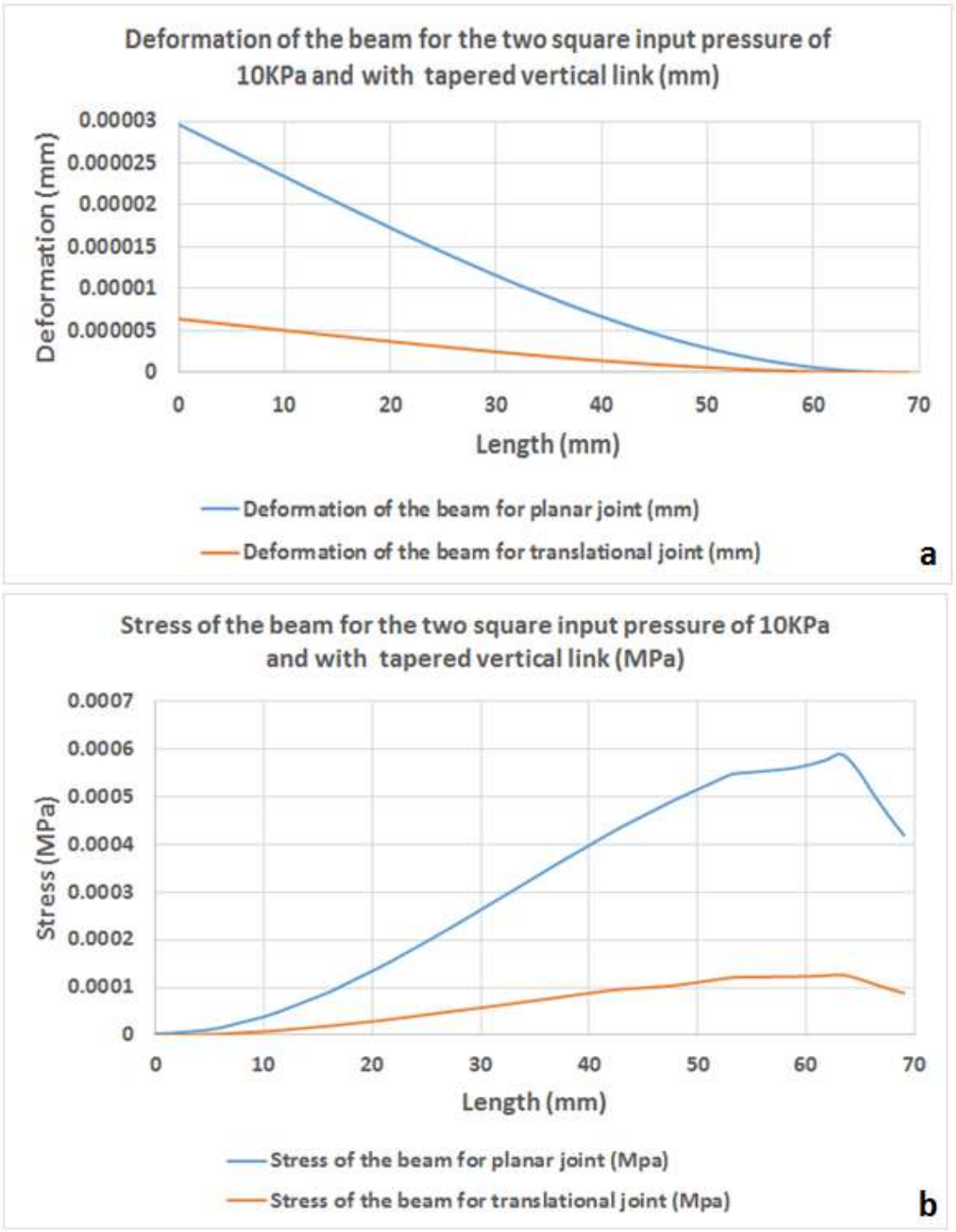

Figure 5.7: a: Deformation and b: stress curves - for input square pressure waves for different joints between the tapered end of the vertical link and the free end of the beam

The deformation curves for both the joints are linear and have magnitudes increased by 100 times. The stress curves for both the joints have become more linear when compared to the flat end vertical link. The buckling effect has also reduced to a great extent. The translational joint structure although has lower magnitude signal than planar joint, is more linear than planar joint. The stress curves for both the joints have increased their magnitude by 10 times when compared to the flat vertical linked beam.

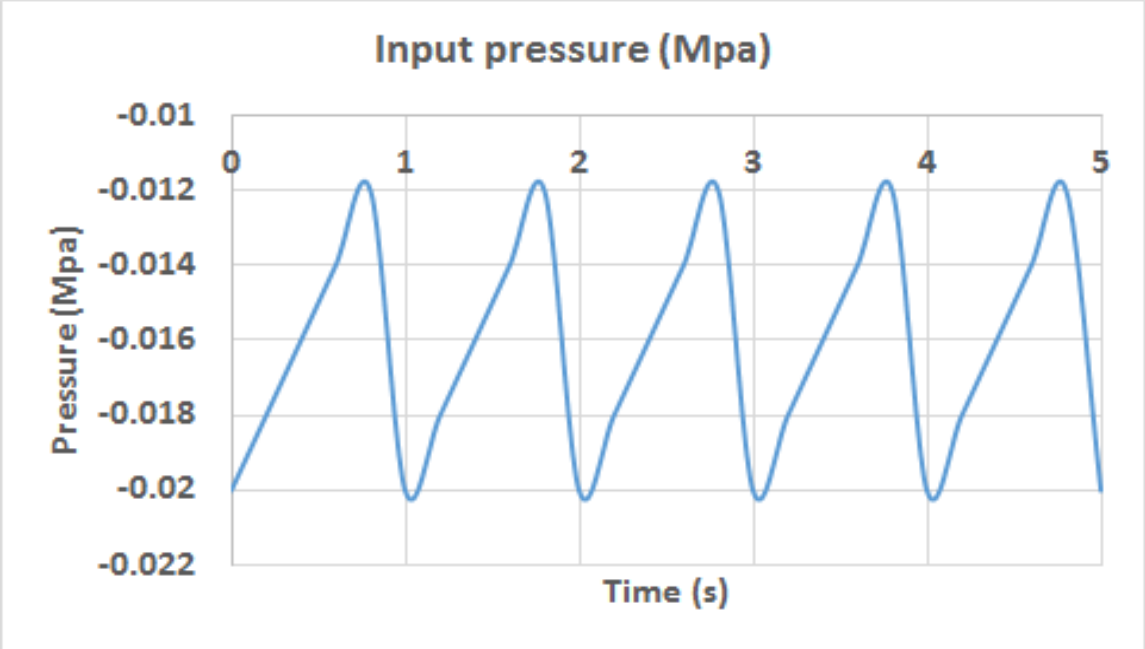

Figure 5.8: Input saw-tooth pressure wave

To study the response of this altered design, with tapered vertical link and translational joint between vertical link and beam, we input a saw-tooth pressure wave of 10-20KPa, which corresponds to 75-150mmHg of blood

pressure, on a 5-second interval. The input is shown in Figure 5.8. Figure 5.9 shows the deformation and stress of the beam along its length.

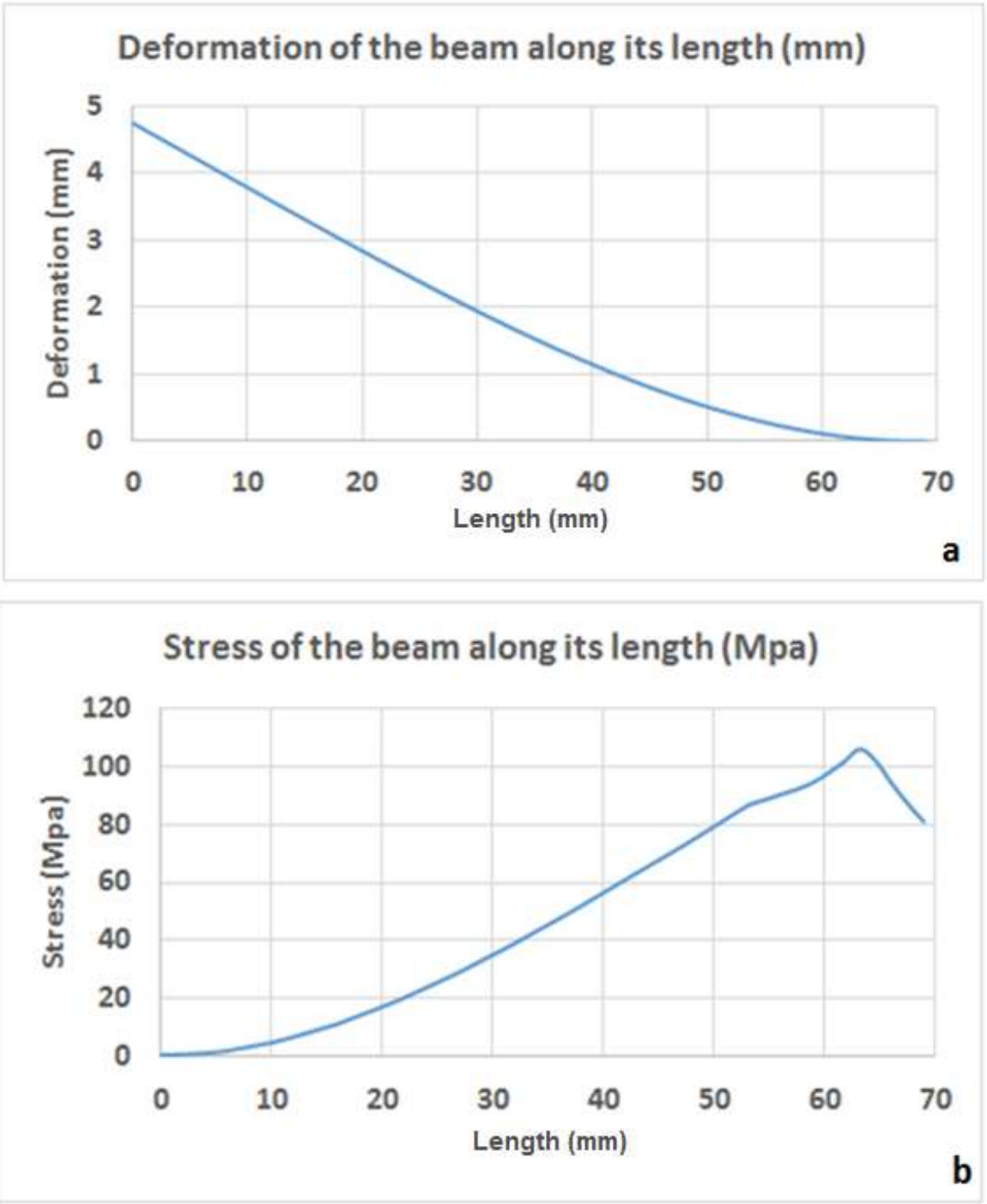

Figure 5.9: a: Deformation and b: stress curves - for the saw-tooth input pressure along the beam length

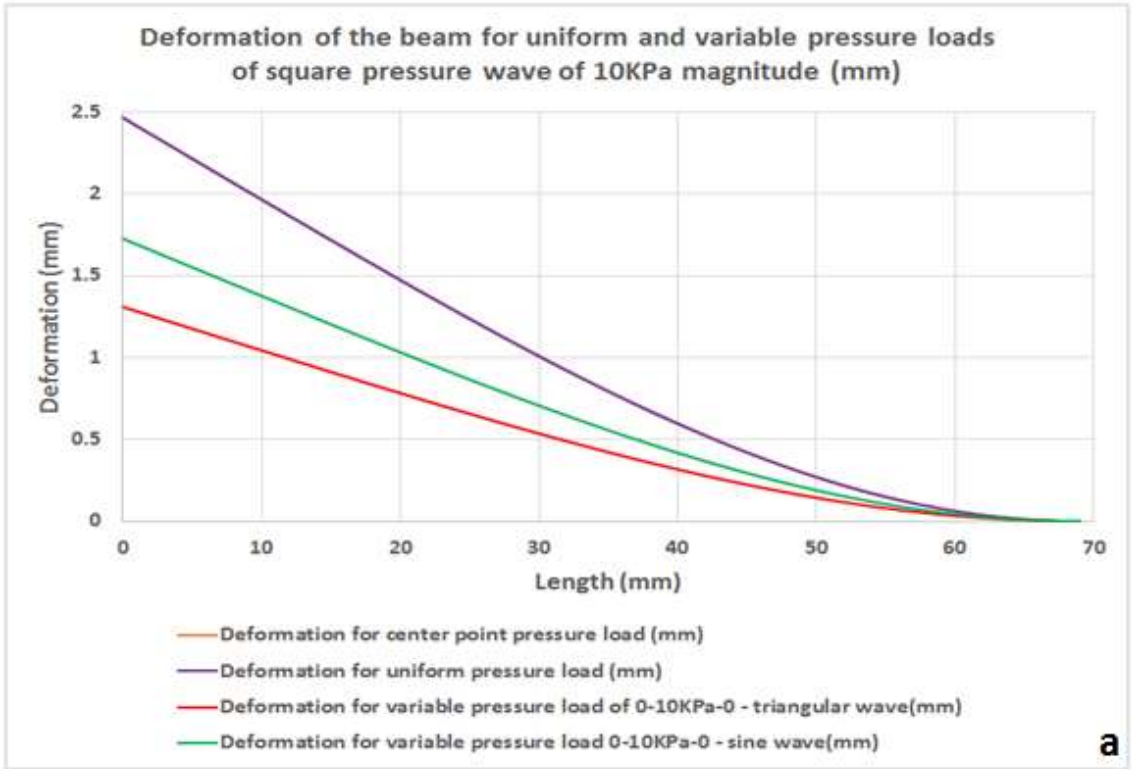

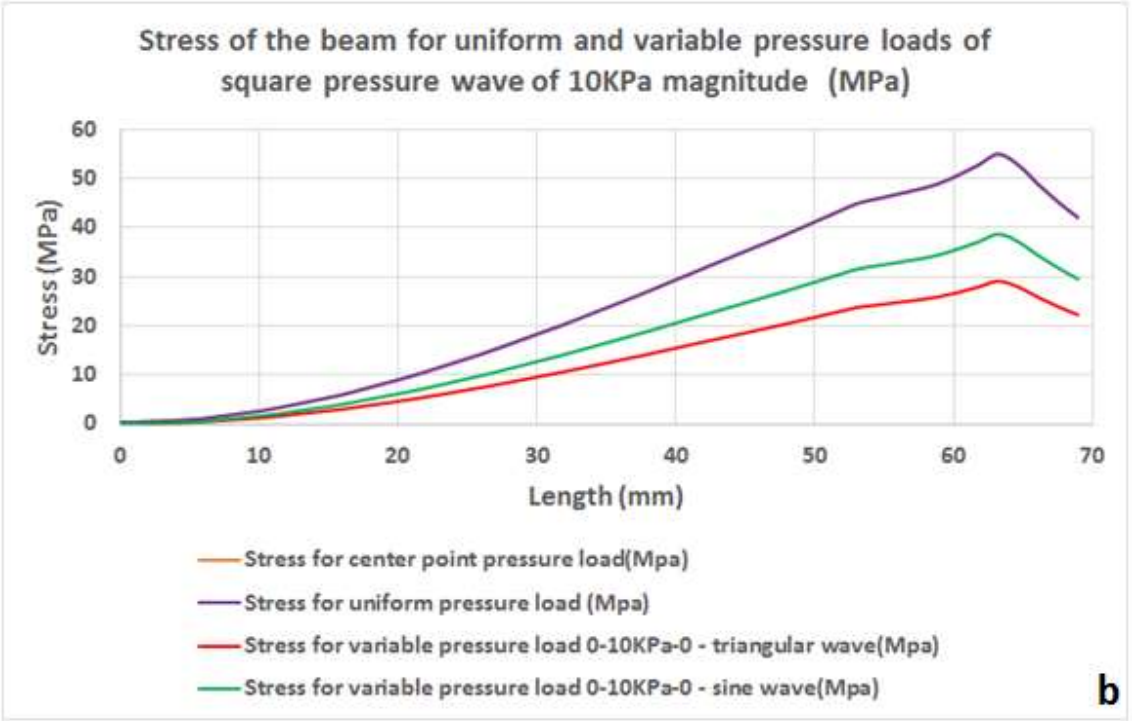

Figure 5.10: a: Deformation and b: stress curves - for uniform and variable pressure loads of 10 KPa magnitude for translation joint between the vertical link and the beam

The curves show that the deformation and stress of the whole beam follow the input pressure and so are the curves along the length of the beam, where they show minimal bucking effect towards the clamped end.

To further study its dynamics in more realistic input environment, uniformly distributed load and point loads are applied and results are recorded. The deformation and stress distribution curves are shown in Figure 5.10. Maximum and similar output is attained for the uniformly distributed and point center loads. This coincides with the deformation-stress study conducted by Noon et al [56]. Lower magnitudes but similar pattern is seen for variable circular-patterned loads with peak pressure applied at the center and reducing towards the ends, in triangular and sine wave formats.

Chapter 6

Inner Striped Sensing Beams: Simulation, Experiment and Analysis

The design consists of testing and evaluating two types of sensors: piezoresistive sensors and piezoelectric sensors in strip format. The strip format design is incorporated for redundant and reliable output information, for lower or self-power and simpler digitalization. We start by using the sensors mounted in a cantilever beam form. Cantilever beam is utilized for higher sensitivity. The work focuses on testing and verifying the principle of the piezoresistive material, followed by piezoelectric sensor to analyze which sensor is better suited for the design.

6.1 Simulation on Piezoresistive Sensing Beam

The active part of the sensor is modeled in Ansys and 10mN of

concentrated downward force is applied on the tip to study the static and kinematics of the beam and to compare it with the experimental results. The specification with which the sensor's active area is built on Ansys 16.2 is shown below in Figure 6.1.

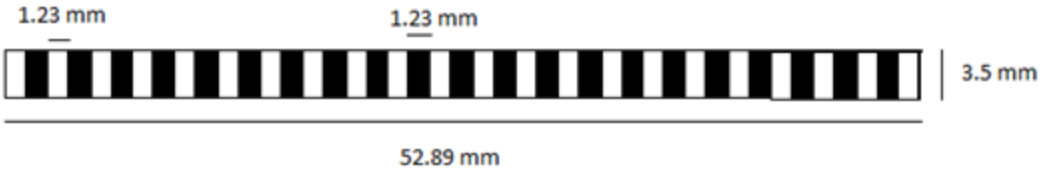

Figure 6.1: Sensor dimensions

The simulation design specifications are done in a way to close replicate the actual sensor's active area. The simulated sensor's dimensions are 52.89 mm in length, 3.5 mm in width and 0.56 mm in thickness (all three layers' thickness together). The active area (52.89 mm) is divided into 43 small strips that are 1.23 mm in length to replicate the actual sensor's resistance and conductive strips. However, since the actual material of each layer of the sensor is unknown, the sensor is designed with three layers of polyethylene one on top of another, with the bottom layer having a density of 950 kg/m^3 and thickness 0.5 mm and trying to replicate the plastic layer of the sensor. The layer above it, which is the resistance layer, is also considered as polyethylene with a density of 2000 kg/m^3 and thickness of 0.05 mm and tries to replicates the active resistance area of the sensor. The top layer, which is the conductive strips on the resistance layer, is also considered as polyethylene with a density of 2300 kg/m^3 and

thickness of 0.01 mm. The simulations show maximum stress and strain on the fixed end and minimum stress and strain on the free end for 10mN of downward force in Figure 6.2.

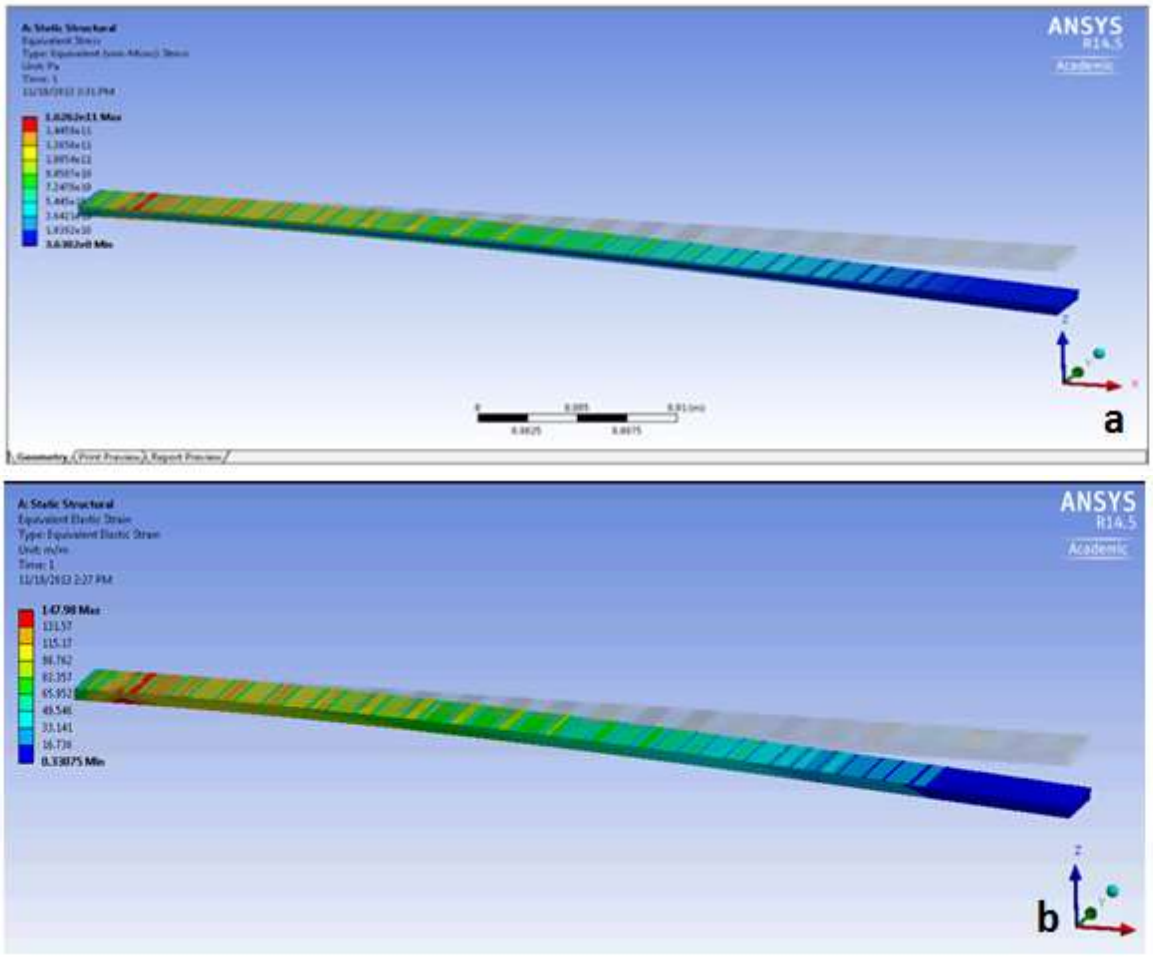

Figure 6.2: a: Stress, and b: strain characteristics for 10mN of downward force

6.2 Experiments on the Piezoresistive Sensing beam

Each channel (a 1Kohm resistance strip sandwiched between two

conductive strips) is connected as a variable resistor to a Wheatstone bridge and in turn connected to an operational amplifier AD620 along with the sensor as shown below in Figure 6.3.

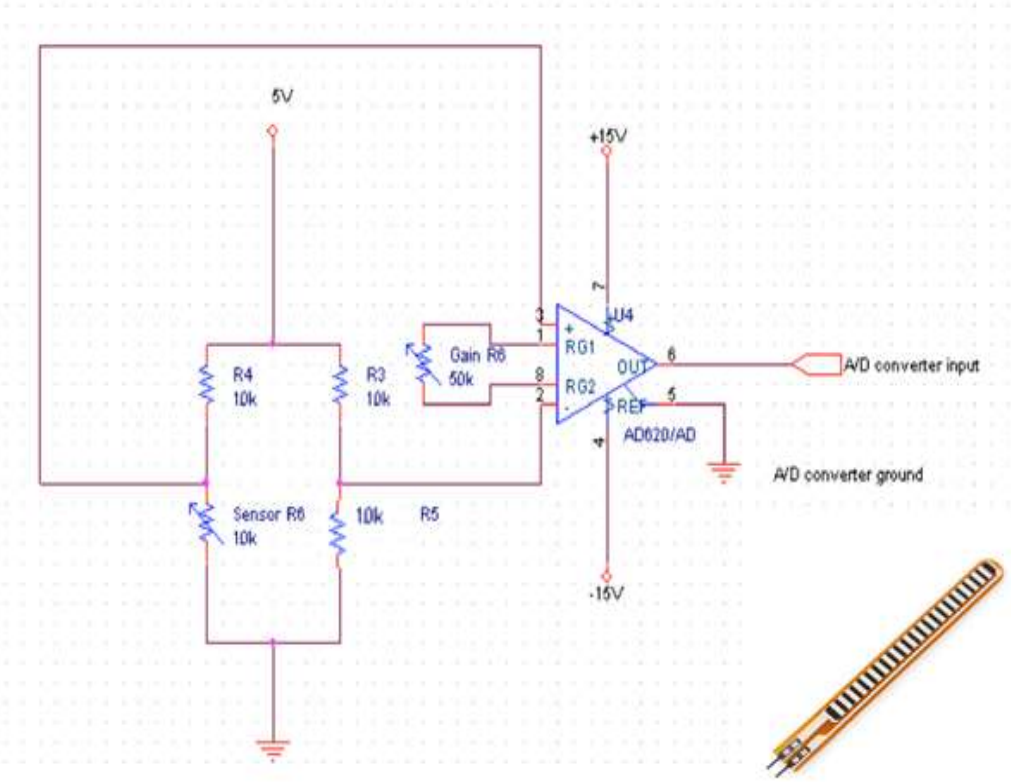

Figure 6.3: Circuitry for each channel of the piezoresistive sensor

The block diagram for the experimental setup is shown in the next Figure 6.4. In the design, the resistive (black) part is coated with a conductive (white) layer which divides the resistive parts in smaller channels of 1Kohms resistance. These are divided into isolated channels and are connected to the Wheatstone bridge. The above circuitry is shown only for one channel. For testing, 6 channels are isolated and 6 independent

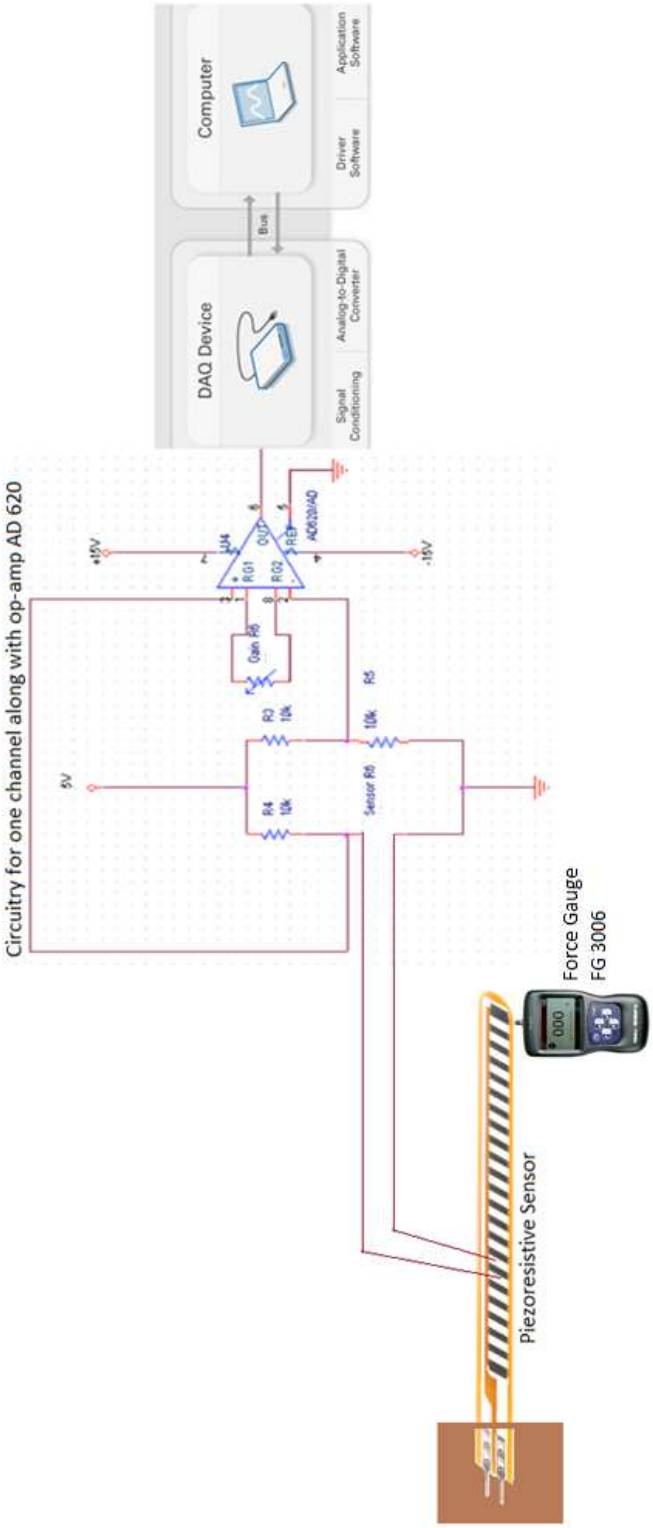

Figure 6.4: Block diagram of the experimental setup for one channel of the piezoresistive sensor

circuits are connected to the 6 channels. A manual concentrated transversal force from 0 to 21mN is applied to the sensor using the Digital Force Gauge Shimpo FG-3006 (Shimpo Instruments) and as the sensor gets bent, the resistance increases. This causes a change in the balance of the Wheatstone bridge and that imbalance develops a voltage. An increase in resistance causes a noted increase in voltage and when the force is reduced the voltage also reduces. The developed output voltage is connected to the low input bias current, high accuracy instrumentation amplifier AD620 (Analog Devices Inc.) and then is interfaced with USB-231 analog/digital input/output board (Measurement Computing Corporation) for signal conditioning and analog-to-digital conversion and later processed in MATLAB. The entire process is shown in Figure 6.4.

To test its sensitivity, forces in the order of mN were applied. Below Figure 6.5 is a plot for 6 channels with voltage over time. As force is increased, the resistance and so the voltage increases and when the force is decreased the resistance and hence the voltage decreases. It is also seen that the increase in resistance (strain) is seen to be more as we move from free end (channel) to the fixed end (channel 6). Below Figure 6.6 is the result for the same sensor with 3 times gain factor applied across the amplifier. Below figure is a plot for 6 channels with voltage over time. As force is increased, the resistance and so the voltage increases and when the force

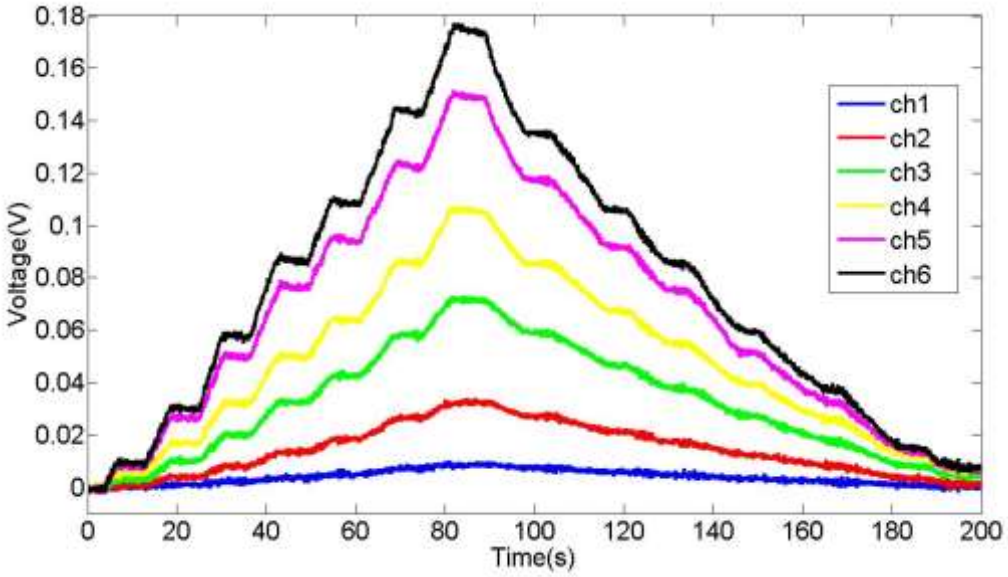

Figure 6.5: Voltage vs Time curve for 6 channels with ch1 on free end and ch6 on clamped end, and with manual force from 0 to 21mN

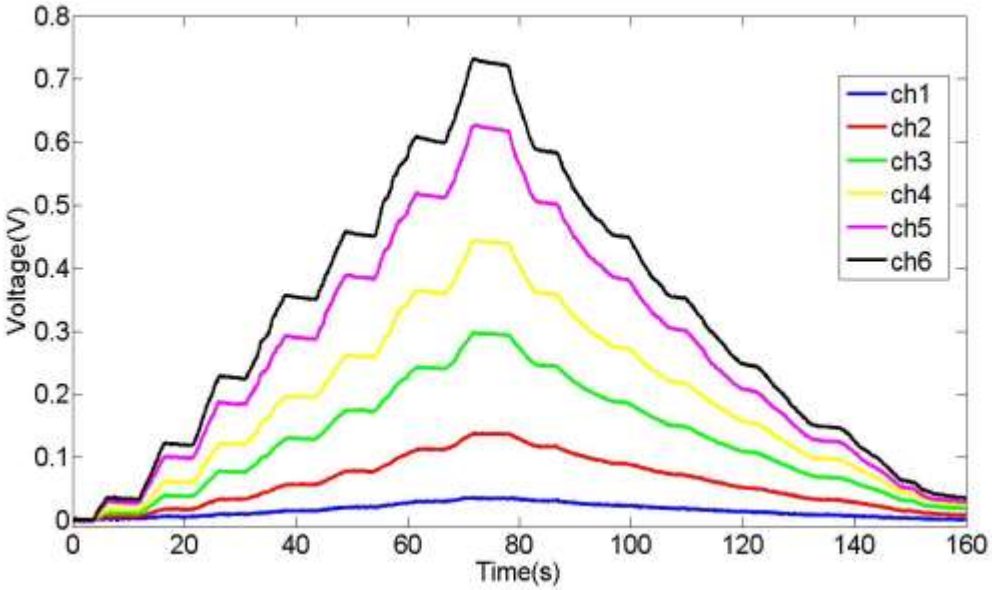

Figure 6.6: Voltage vs Time curve for 6 channels with ch1 on free end and ch6 on clamped end, with manual force from 0 to 21mN, and with 3 times amplification

is decreased the resistance and hence the voltage decreases. It is also seen that the increase in resistance (strain) is seen to be more as we move from

free end (channel) to the fixed end (channel 6). The consistency of the above results was tested with more than one sensor, and testing was done several times. The below Figure 6.7 shows the actual setup for the experiment conducted in testing the sensor's principle.

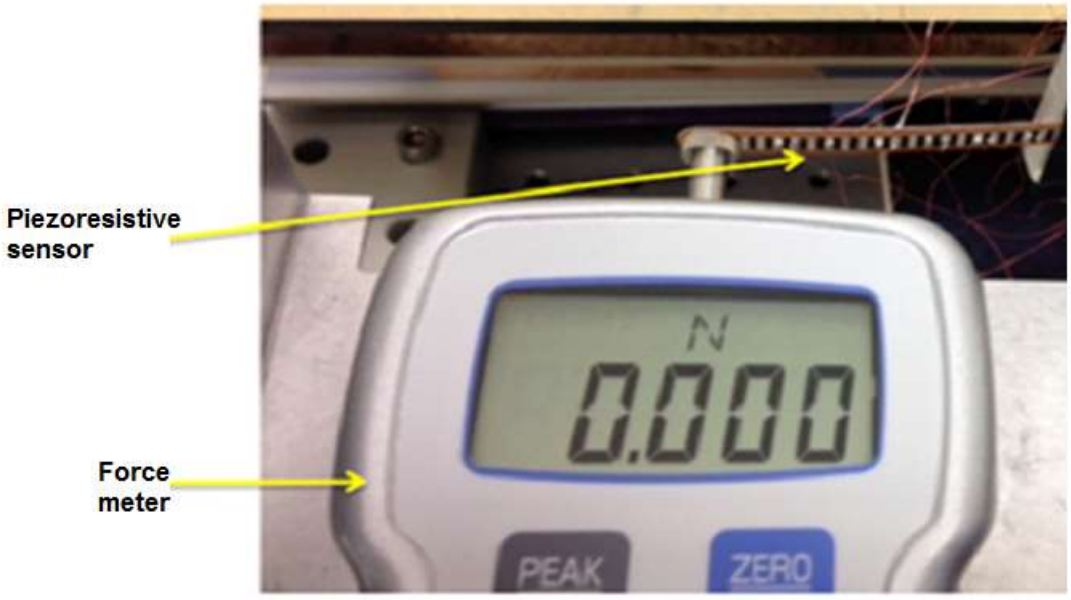

Figure 6.7: Actual experimental setup for the piezoresistive sensor

With these preliminary results being promising, the work continues with piezoelectric sensors.

6.3 Dynamic behavior of the Striped Sensing Beam

To analyze the sensor dynamics and test its correlation with the experimental results, the deflection of the sensor is detected with a laser

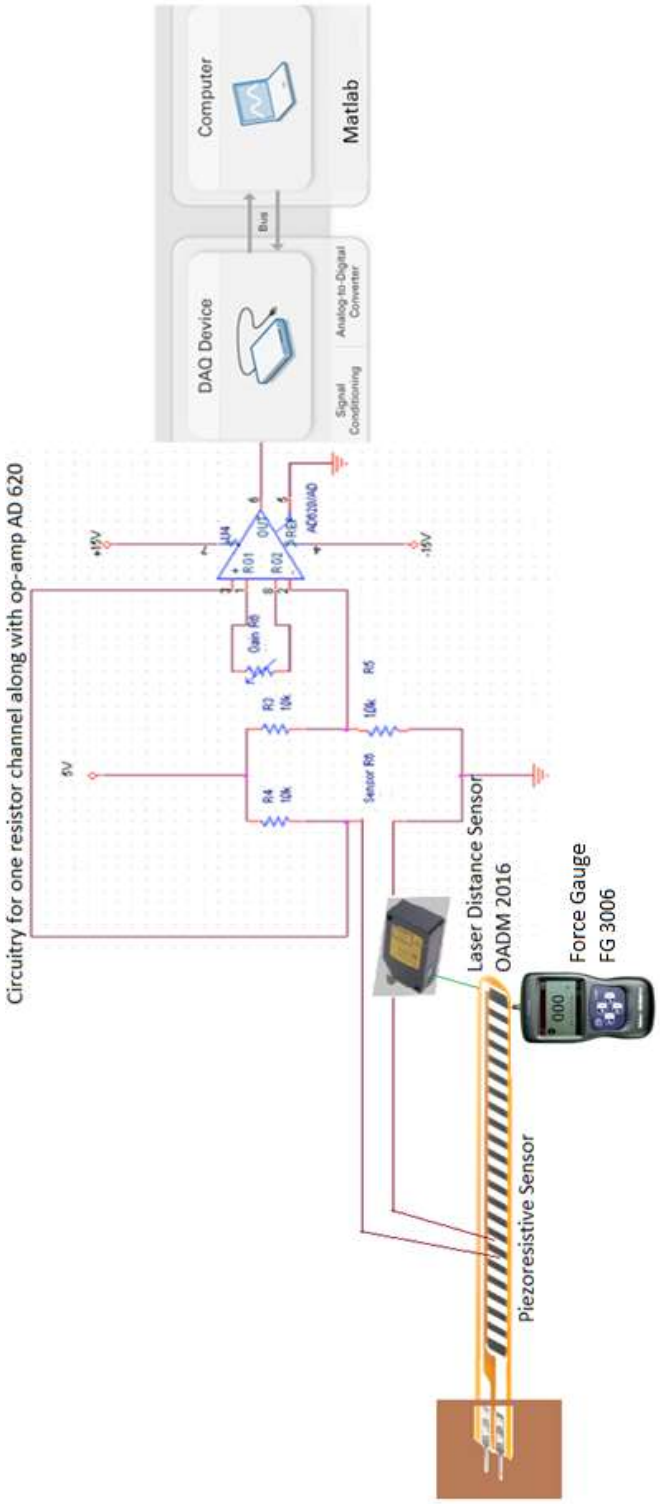

Figure 6.8: Block diagram of the experimental setup to test the sensor dynamics

distance sensor (OADM 2016 series) when the force is applied with a force meter. The laser distance sensor is placed behind the piezoresistive sensor and the force meter is placed at the same position, in front of the piezoresistive sensor. The entire experimental setup is shown in the below Figure 6.8. The laser distance sensor is based on the triangulation principle [63]. The emitted laser beam falls on the sensor tip where the force is applied by the force meter. The laser beam falls on the sensor as a small light spot and is reflected back diffusely. The position of the received spot on the receiver (a diode line) defines the received angle. When the piezoresistive sensor is further away from the laser sensor, the received

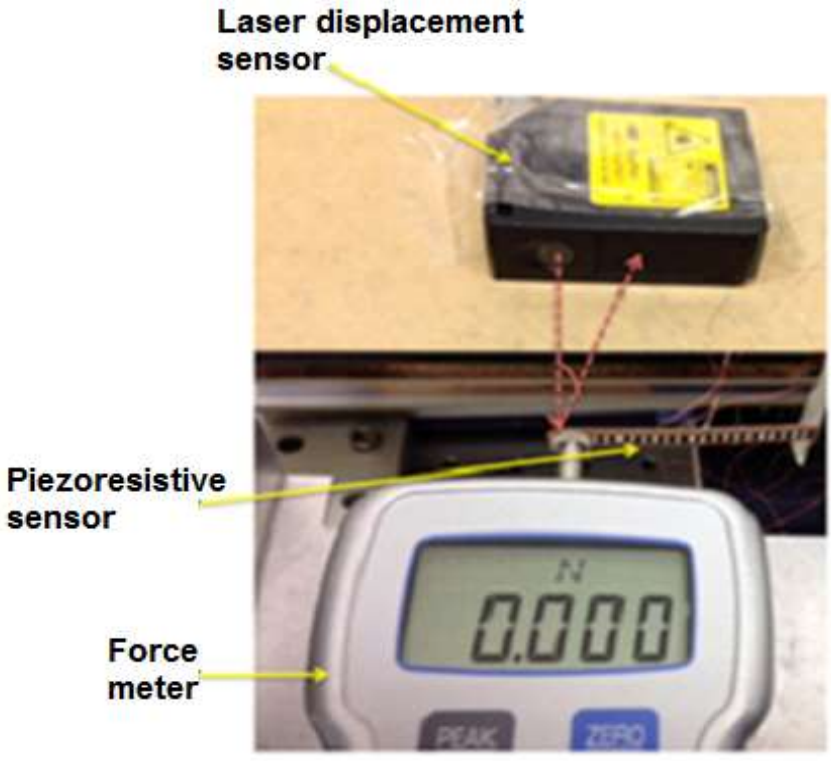

Figure 6.9: Actual experimental setup to test the sensor dynamics

angle will be smaller and when it is closer (on deflection), the received angle will be larger.

The output signal is linearly proportional to the distance. Upon no deflection, the laser sensor's signal will be at a particular voltage and when deflected the amplitude increases as the piezoresistive sensor is closer to the laser sensor. The dynamics of the piezoresistive sensor is obtained by applying random forces and by finding the correlation between the input (displacement - laser sensor) and output (voltage – piezoresistive sensor). Figure 6.8 shows the block diagram of the experimental setup and Figure 6.9 shows the actual experimental setup with the force meter in front of the sensor and laser sensor, which detects the displacement of the piezoresistive sensor by the reflection angle of the laser, behind the sensor.

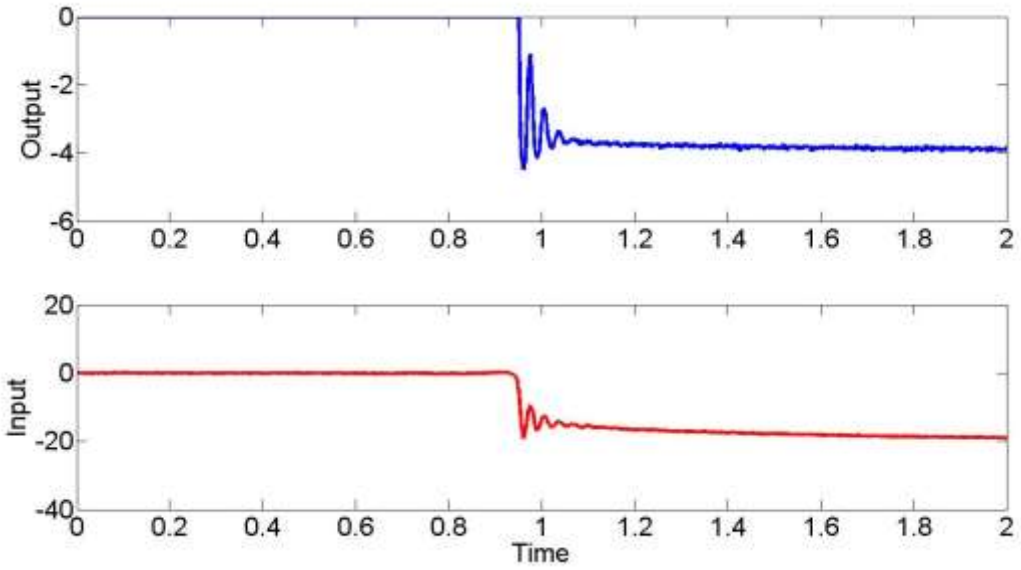

Figure 6.10: Random vibrations recorded in the laser sensor as input and voltage from one channel from the piezoresistive sensor

Figure 6.10 is the plot of random vibrations recorded in the laser sensor as input and voltage from one channel from the piezoresistive sensor.

The best fit transfer function (94.55%) is,

$$G(s) = \frac{0.2457*s+0.1884}{0.0004853*s^2+1.053*s+1} \quad (6.1)$$

It is found using system identification toolbox in MATLAB, which finds the best fit transfer function depending on the input vs output data that was obtained experimentally. The transfer function is a second order under damped transfer function with a zero. The input is physical displacement of the sensor in millimeters and the output is the response of the input in voltage. To verify transfer function, the output should follow the input of this second experiment.

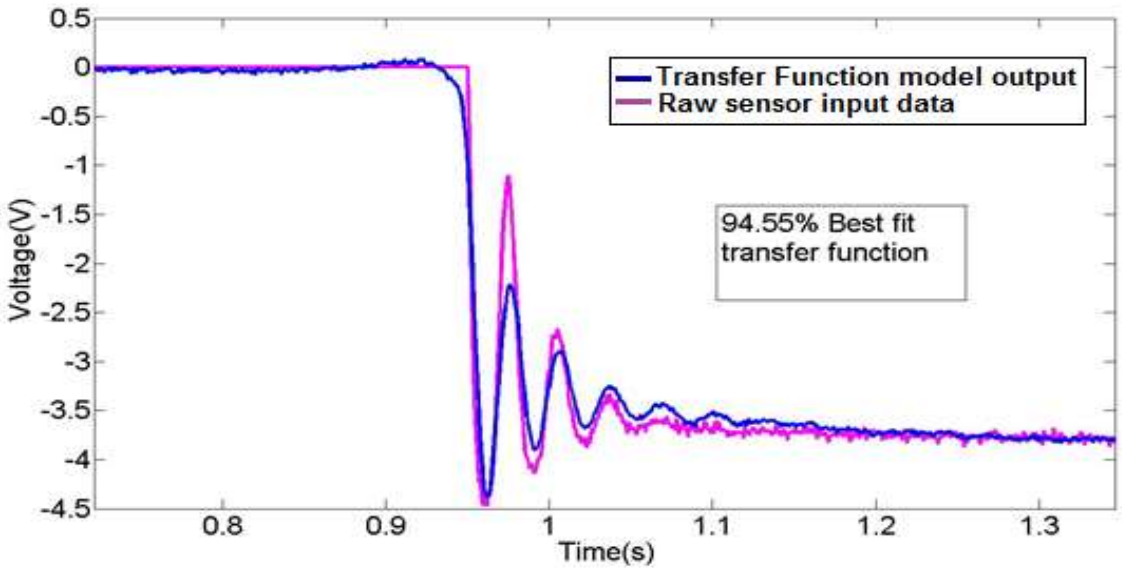

Figure 6.11: Transfer Function vs sensor output for the piezoresistive channel

Figure 6.11 is used (Figure 6.12 with Simulink) to test how the transfer function follows the input.

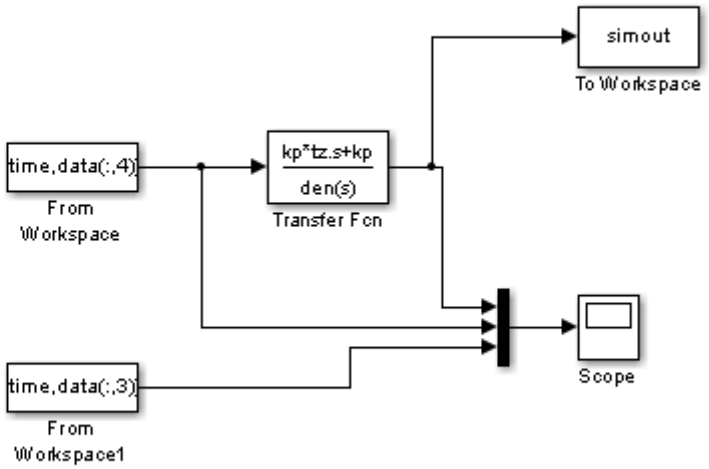

Figure 6.12: Simulink model to examine the TF performance

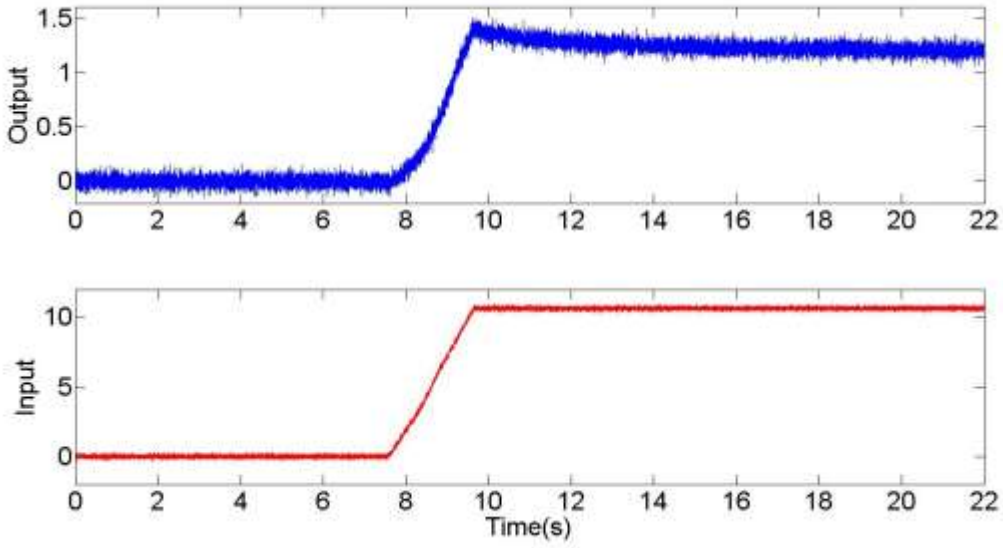

Figure 6.13: Input and output using the TF in equation 6.1

The data from a different channel on the sensor and the original sensor channel is used and the simulation along with the actual measured data from the DAQ is plotted. As seen, the transfer function closely fits the approximate step response.

Verification of the transfer function is shown in Figure 6.14.

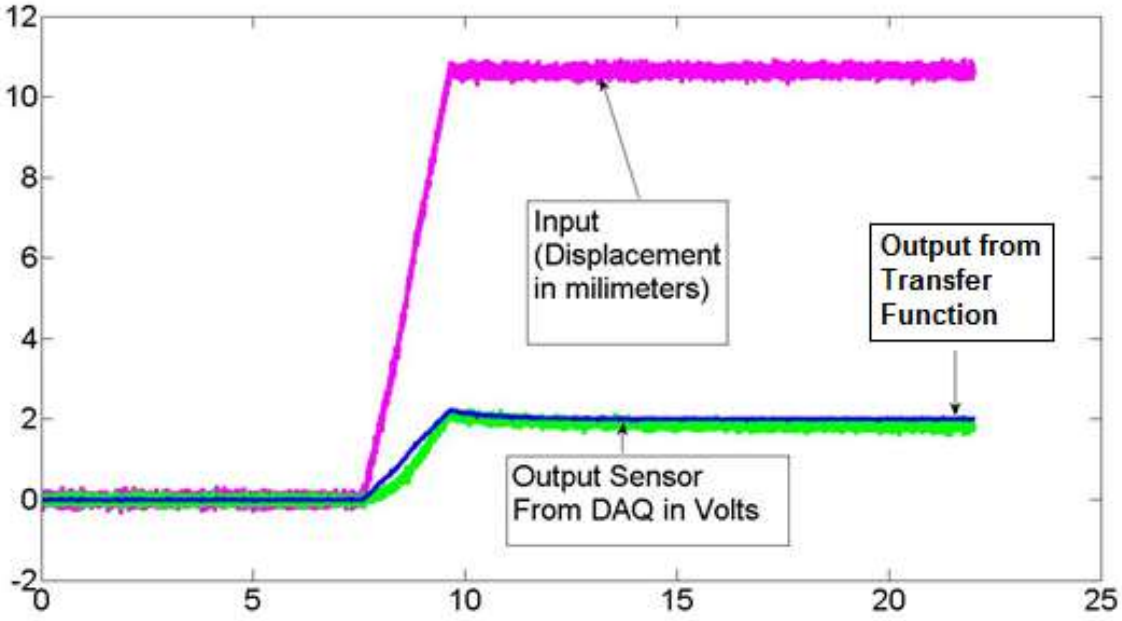

Figure 6.14: Verification that TF follows the input using Simulink

6.4 Simulation on Piezoelectric Sensing Beam

The composite cantilever beam structure with the sensing area strips of the sensor is modeled in ANSYS and concentrated downward forces of 10mN, 30mN and 50mN are applied on the tip to study the static and

kinematic characteristics. The specification with which the composite beam structure is built on ANSYS is shown below in Figure 6.15.

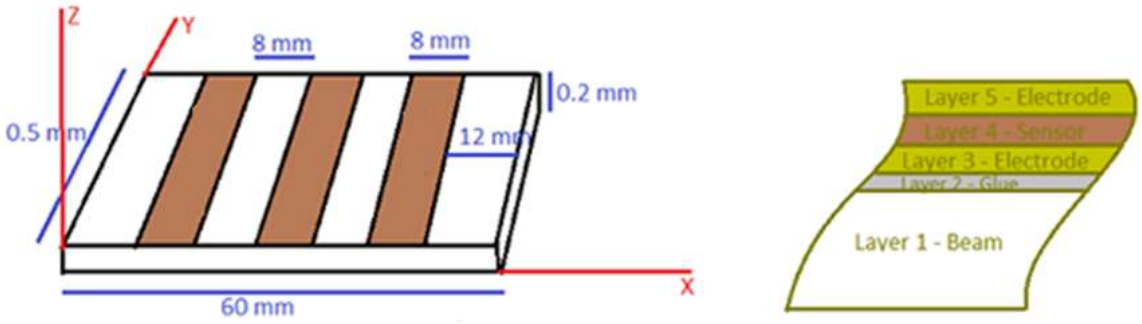

Figure 6.15: Illustration of composite beam specifications

The simulation design specifications are done in a way to close replicate the actual sensor's active area. The simulated composite beam's dimensions are 60 mm in length, 0.5 mm in width and 0.2 mm in thickness (all five layers' thickness together). Three PVDF sensor strips along with electrode layers are glued in equal distance on the beam. The strips are 8 mm wide each. The layers are designed with polyethylene one on top of another, with different density (ρ), elastic modulus (Y) and Poisson ratio (γ) values. The beam layer with ρ as $1.35 * 10^3 kg/m^3$, Y as $3.8 * 10^9 Pa$ and γ as 0.4 , similar to Polyster. The electrode layers with ρ as $3 * 10^3 kg/m^3$, Y as $0.1 * 10^9 Pa$ and γ as 0.37, similar to that of silver ink. The PVDF sensor layer with ρ as $1.78 * 10^3 kg/m^3$, Y as $3 * 10^9 Pa$ and γ as 0.34. the glue layer with ρ as $1.01 * 10^3 kg/m^3$, Y as $5 * 10^9 Pa$ and γ as 0.49, similar to that of acryl pressure sensitive adhesive.

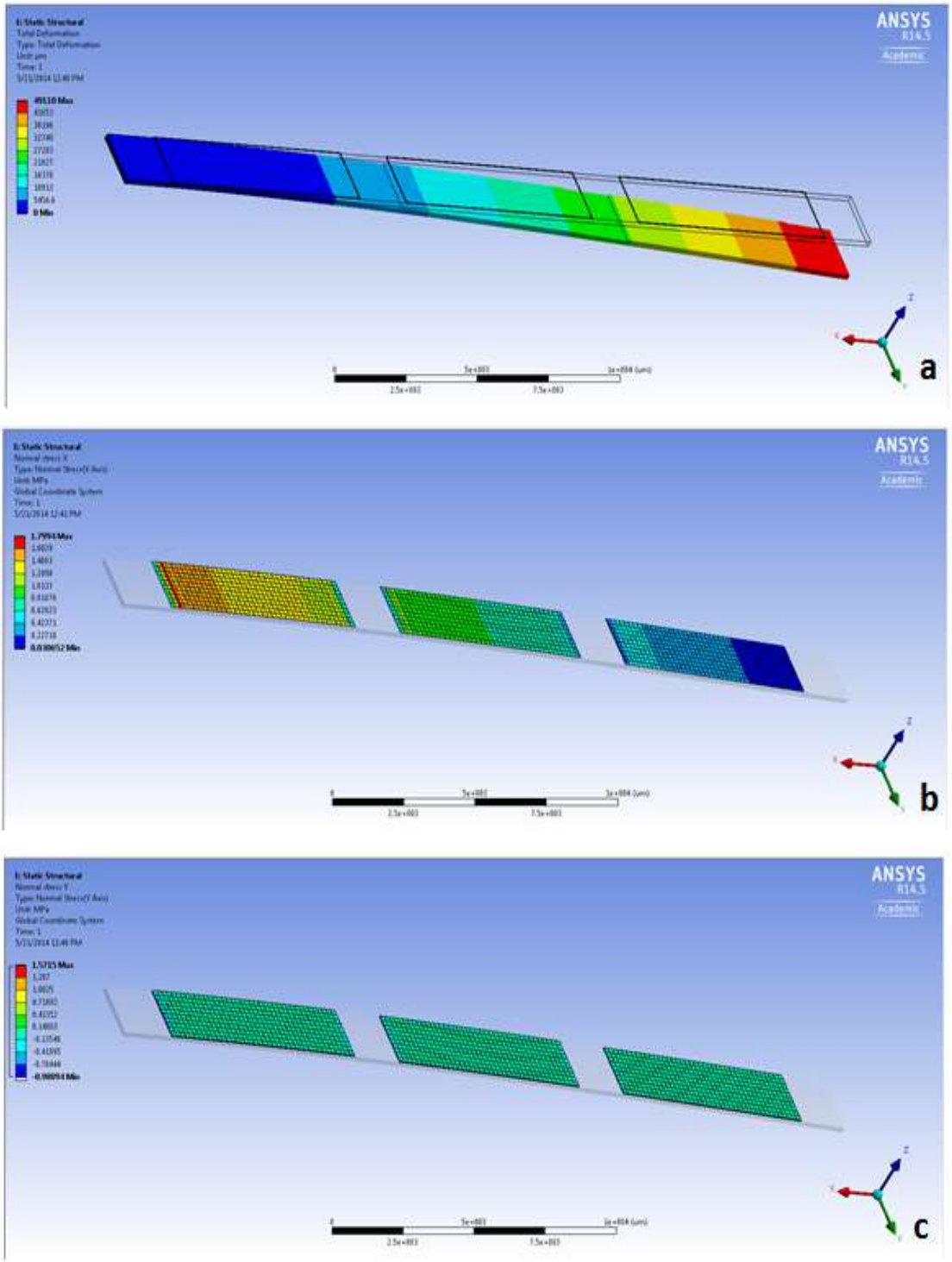

Figure 6.16: a: Total deformation, b: stress along x direction, and c: stress along y direction – Simulation

The simulations in the Figure 6.16 show the total deformation and normal stress along x and y directions for 30mN downward force showing maximum deformation on the free end and maximum stress on the fixed end.

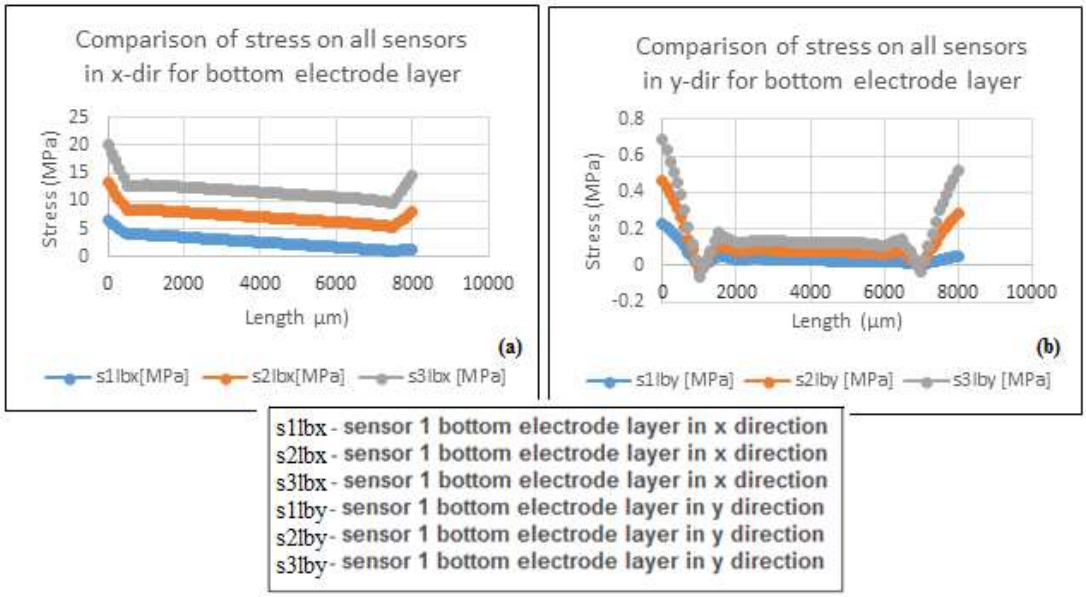

Figure 6.17: Comparison of stress on all sensors on the bottom electrode layer for 10 mN of downward force for – a: x direction and b: y direction

The graphs on Figure 6.17 show the comparison of stress on all sensors (sensor 1 on free end and sensor 3 on fixed end) on the bottom electrode layers along x and y direction for 10mN of downward force. Similar simulations and comparisons are done for 10mN and 50mN of downward forces and it follows the above curves. The graphs on Figures 6.18 and 6.19 show the comparison of stress on all sensors (sensor 1 on free end

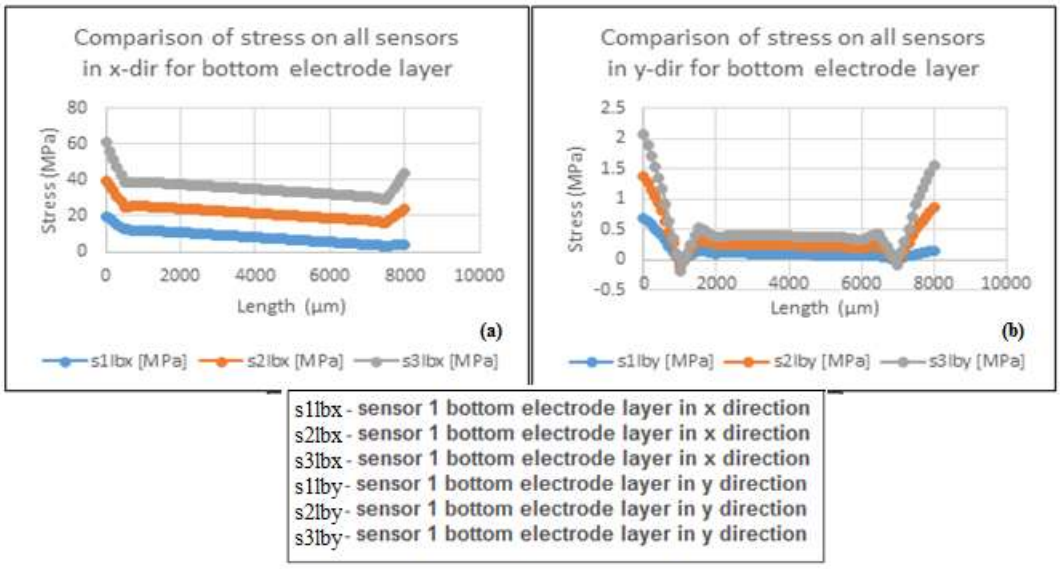

Figure 6.18: Comparison of stress on all sensors on the bottom electrode layer for 30 mN of downward force for a: x direction and b: y direction

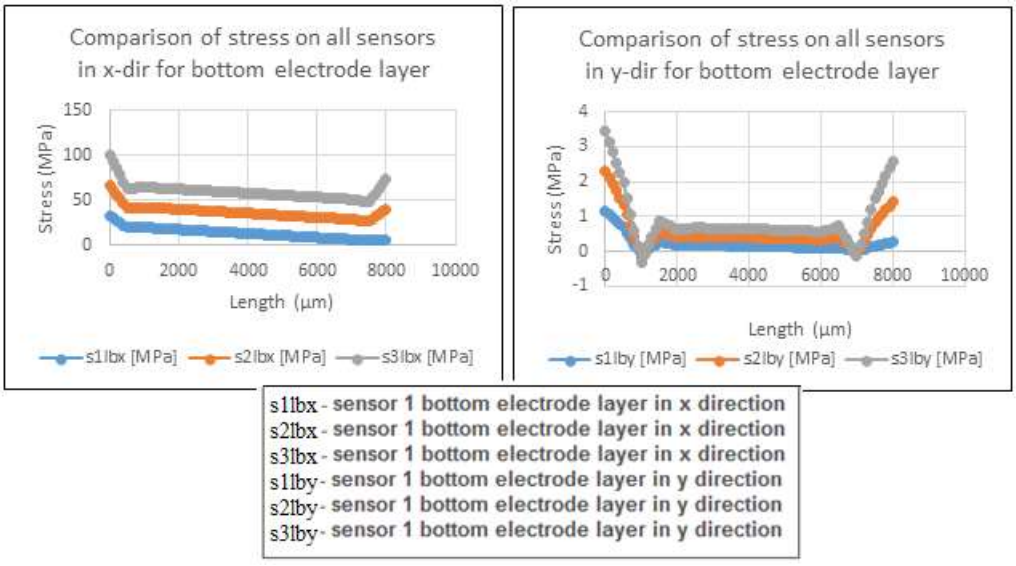

Figure 6.19: Comparison of stress on all sensors on the bottom electrode layer for 50 mN of downward force for a: x direction and b: y direction

and sensor 3 on fixed end) on the bottom electrode layers along x and y direction for 30mN and 50mN of downward forces respectively. All the stress curves show maximum stress towards the clamped end and more stress in x direction when compared to y direction. Simulation was also done to see the percentage of strain levels transferred between each layer on the composite beam with sensor 3 on free end and sensor 1 on fixed end. The graph on Figure 6.20 shows the strain percentage difference experienced by the top electrode sensor layer and by the respective beam area. Data analysis show the percentage of strain effect transfer from beam

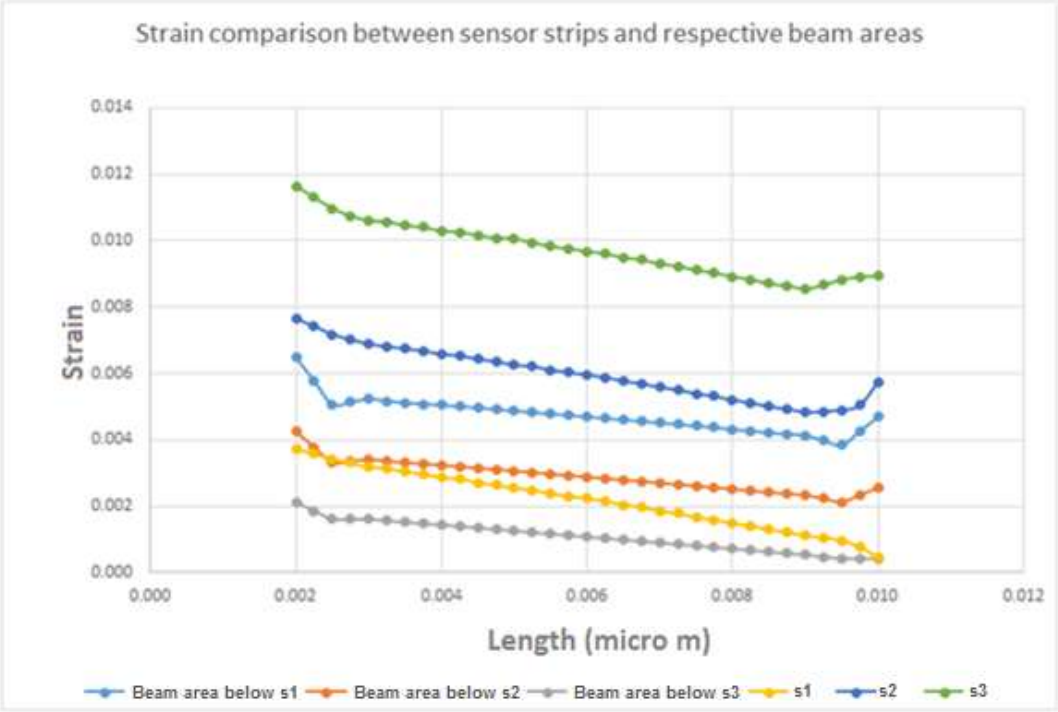

Figure 6.20: Strain transfer rate between the beam layer and sensors' top electrode layers

to the sensor's top electrode layer are around 75% for sensor 1 (fixed end), around 80-85% for sensor 2 and around 85-90% for sensor 3 (free end) [59,60].

6.5 Experiments on the Piezoelectric Sensing Beam

For initial work, a cantilever beam is designed with a 14-cm length plastic rod with the piezo films glued on top of the beam. The piezo film used for the experimental setup is piezo vibration sensor from Sparkfun Electronics. The film is almost 25mm long. The film along with its dimensions are shown in the below Figure 6.21.

The piezoelectric film, PVDF, comes in various thickness and lengths and is extremely light weight and flexible plastic. Its mechanical and electrical properties [56] allow it to be used a transducer with a wide frequency and dynamic range ranging between 0.001 – 109 Hz and 10.8 to 106 psi to Mbar respectively. It has a low acoustic impedance, very similar to water and human tissue, has higher output voltage than piezo ceramics, 10 times more for the same input, high elastic compliance, high mechanical and dielectric strength, high impact resistance and highly stable. It resists moisture, most chemicals and oxidants, UV and nuclear radiation. It can

be fabricated [56] in any design and can be glued using any commercially available adhesives.

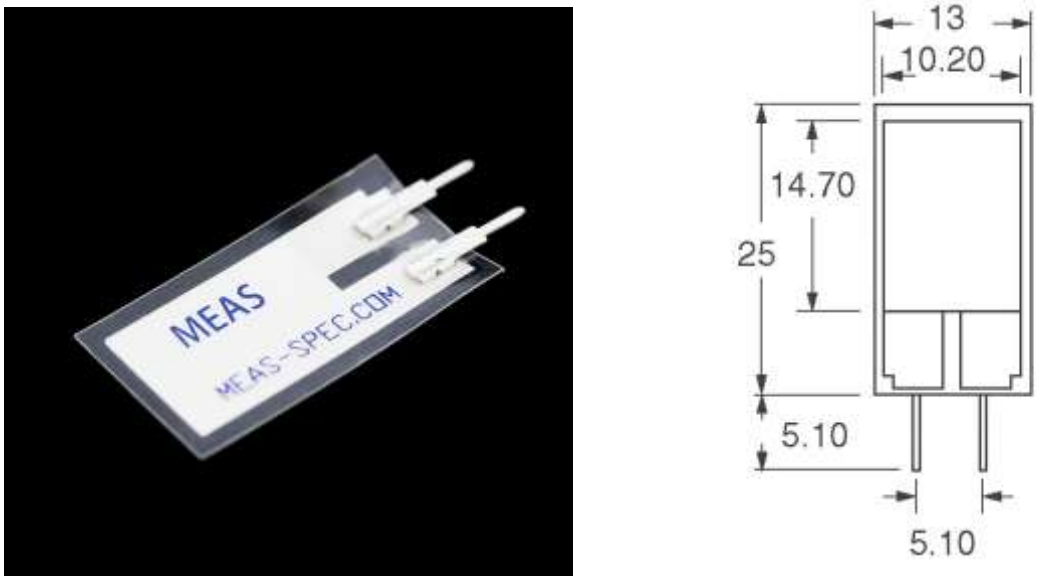

Figure 6.21: Piezoelectric film used for experiments and its dimensions (adopted from Sparfun Electronics)

Five piezo films are glued on top of the plastic 14 cm beam with a gap length of 1 cm in between them. These five piezo films are the five sensors on top of the cantilever beam. The input is applied at the tip of the cantilever beam. The input is through a vibration shaker, which is an electro-dynamic vibration generator from Ling Dynamic Systems that is connected to a function generator. Sine wave input is applied through the shaker. The output from each piezoelectric sensor is interfaced with USB-231 board (Measurement Computing Corporation) through the electronic buffer.

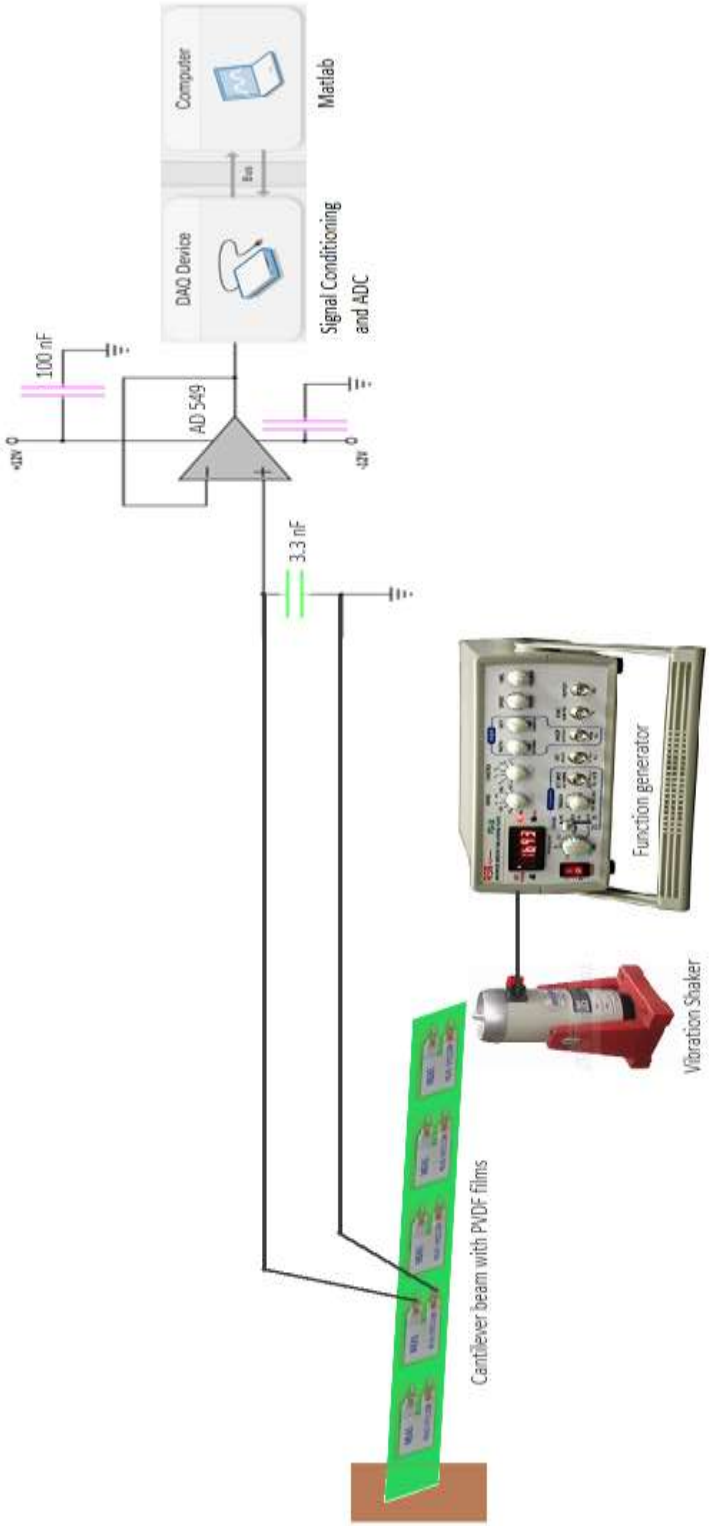

Figure 6.22: Block diagram of the experimental setup to test piezoelectric sensors on the cantilever beam

The circuit is constructed using the ultralow-input bias current operational amplifier AD549 (Analog Devices, Inc.) with high input impedance Rin= 10^{13} Ω and low-bias current 150fA. AD 549 is connected as a voltage follower to account for charge leak in piezoelectric sensors.

The experimental setup is shown in the Figure 6.22. The figure shows the circuit connection for only one PVDF sensor film. The actual setup is shown in the below Figure 6.23.

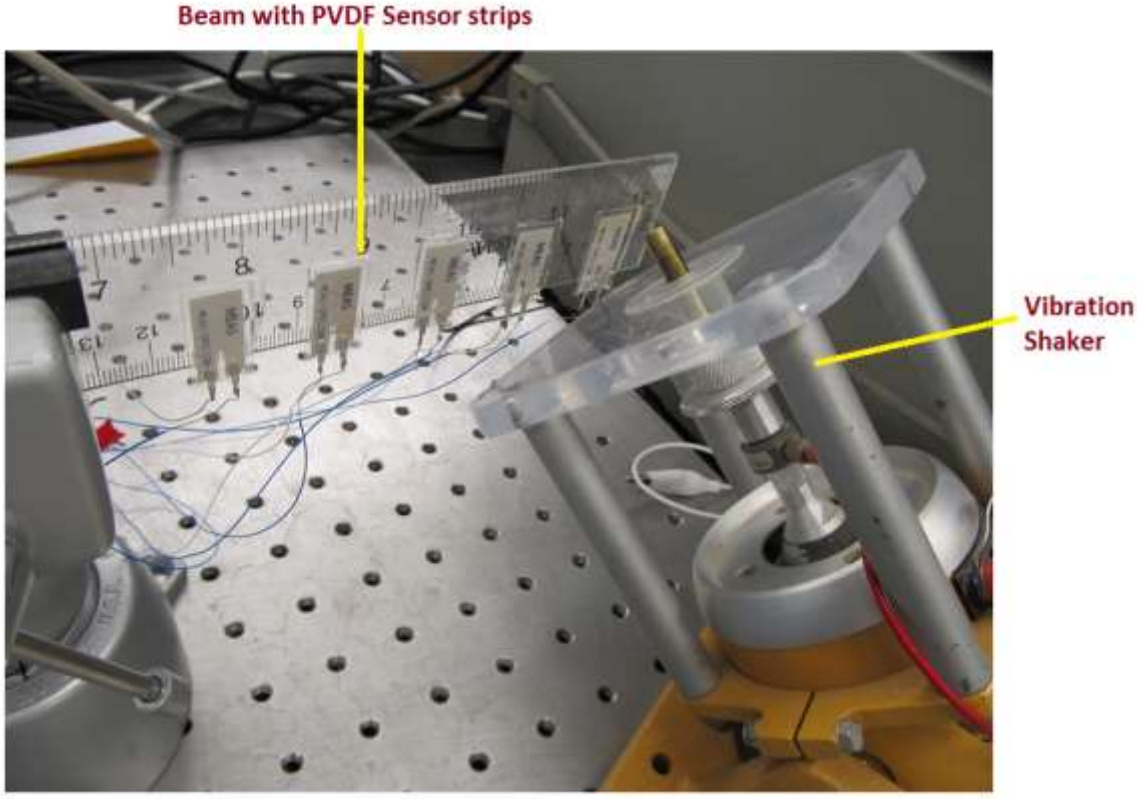

Figure 6.23: Experimental setup to test piezoelectric sensors on the cantilever beam

A concentrated transversal force in terms of voltage from function generator of up to 1.5 V, peak-to-peak, is applied to the shaker (Figure 6.24) and as the sensor gets bent, the stress increase with a noted increase in voltage and when the force is reduced the voltage also reduced. As force is increased, the stress and so the voltage increases and when the force is decreased the stress and hence the voltage decreases. It is also seen that the increase in stress is seen to be more as we move from free end to the fixed end. The output is shown in Figure 6.25.

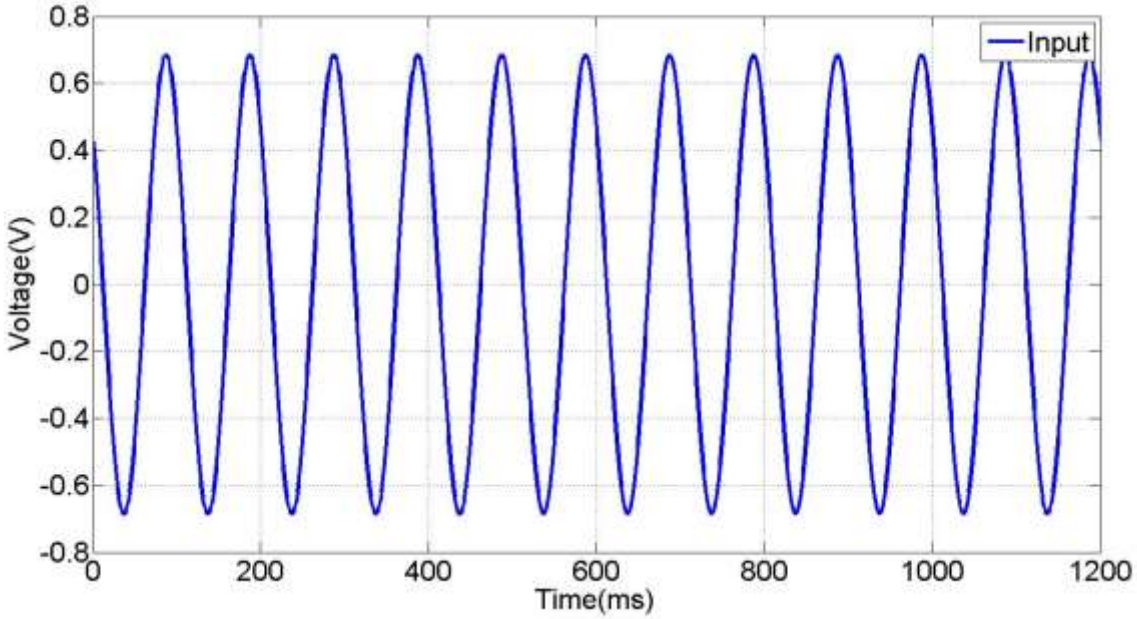

Figure 6.24: Input applied to the beam with the vibration shaker signaled by function generator

The data is processed in MATLAB. The same is repeated for square and triangular waveforms to check the consistency and redundancy. The

consistency of the above results was tested with more than one sensor, and testing was done several times.

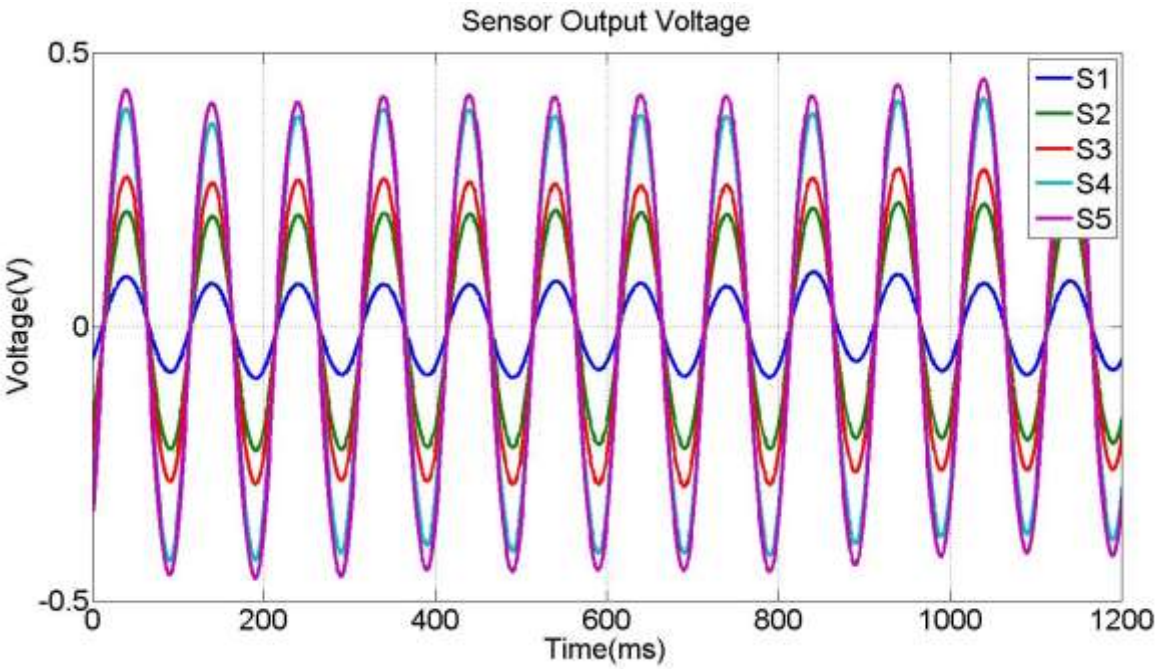

Figure 6.25: Output Sensor voltages from the 5 sensing strips with S1 on free end and S5 on clamped end

Based on the simulation and experimental results, and based on the principle of operation of piezoresistive and piezoelectric sensors, piezoelectric sensors are a better fit for the current pressures sensor unit design due to their passive nature. The inherent property of piezoelectricity that generates charge on deflection, is a superior property against the power required to measure the change in resistance for the piezoresistive

sensors. So piezoelectric sensors are incorporated in the proceeding work.

The work can be extended to also find a sensor beam design that is more sensitive to changes in force. To do so, the sensor can be divided into varying length sensor strips areas as shown below in Figure 6.26, in future work. This unequal sensing design can sense output with similar voltage, thereby having a similar sensitivity. The design is simulated in the modeling that is discussed in the next Chapter; Chapter 7, session 7.2.2.

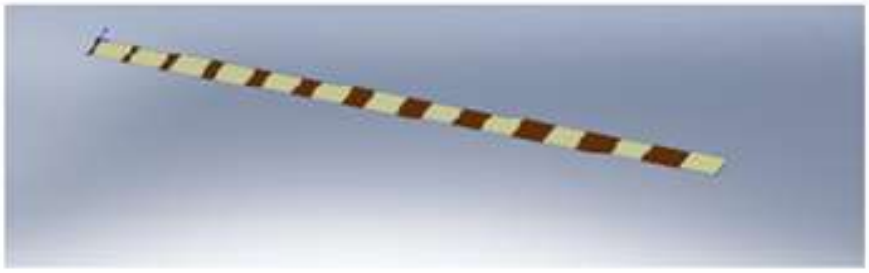

Figure 6.26: Beam with varying sensor strips

Chapter 7

Modeling of PVDF Striped Sensing Beam and Verification

The PVDF sensors due to its inherent passive property is used as the sensing strip on the pressure sensor unit. The PVDF sensing strips on the sensing beam are modeled in this chapter by incorporating the constitutive direct piezoelectric sensor equation and Euler Bernoulli beam theory for equation of motion of the sensing beam, to derive the transfer function, as in below Session 7.1.

7.1 Modeling of the PVDF Striped Sensing Beam

The constitutive sensor equation for the piezosensor [58] is,

$$D_i = \varepsilon_{ij} E_j + d_{im} \sigma_m \tag{7.1}$$

where D_i is the electric displacement generated on the i^{th} direction, ε_{ij} is the dielectric permittivity, d_{im} is the piezoelectric coefficients which

describes the electric displacement per unit stress at constant electric field E_j and σ_m is the stress vector. Figure 7.1 shows the composite cantilever beam structure with equal PVDF sensor strips spaced equally.

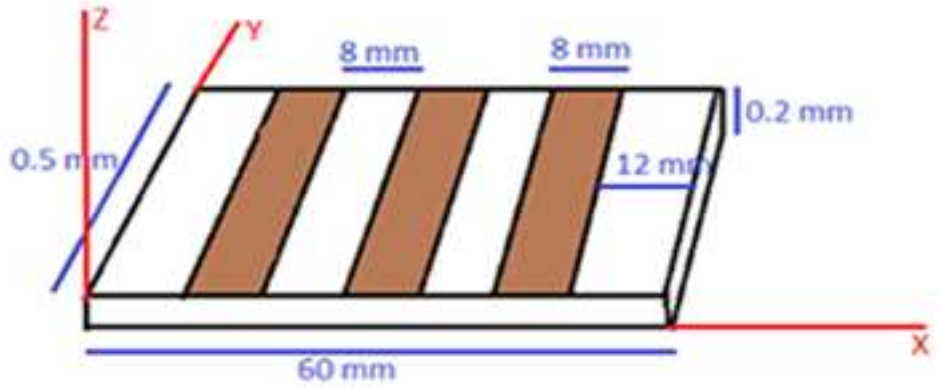

Figure 7.1: Composite cantilver beam structure with sensing strips

Since the electric displacement D_i is caused due to the stress generated by the force on the sensor the first term due to application of electric field E_j is neglected. So, the above equation reduces to the form,

$$D_i = d_{im}\sigma_m \tag{7.2}$$

A force acting downward at the sensor beam tip, as shown on figure 13, will cause stress on the x and y direction in each sensor k, k=1,2,3. So the generated electric displacement D_{3k} will take strain from both the directions into account. Thus,

$$D_{3k}(r,t) = d_{31k}\sigma_{1k}(r,t) + d_{32k}\sigma_{2k}(r,t),\ s_{k1} \le r \le s_{k2} \tag{7.3}$$

Also, Young's modulus Y is given by,

$$Y = \frac{stress}{strain} = \frac{\sigma}{\varepsilon} \tag{7.4}$$

So,

$$D_{3k}(r,t) = d_{31k} Y_4 \varepsilon_{1k}(r,t) + d_{32k} Y_4 \varepsilon_{2k}(r,t) \tag{7.5}$$

where Y_4 is the Young's modulus of the sensor layer. Also, Poisson ratio is given by the ratio of lateral to longitudinal strain for a longitudinal stress as,

$$\gamma = -\frac{\varepsilon_2}{\varepsilon_1} \text{ which is also, } \gamma = -\frac{\varepsilon_2}{\varepsilon_1} = -\frac{\sigma_2}{\sigma_1} \tag{7.6}$$

For a PVDF sensor layer, the correction factor that has to be included to account for all strains will be,

$$K_p = (1 - \gamma \frac{d_{32}}{d_{31}}) \tag{7.7}$$

When an external force f acts on the sensor beam tip, the cantilever beam deflects in the x direction and causes a stress on the sensor layer,

$$\sigma_k (r,t) = -c_4 Y_4 \frac{\partial^2 w_k(r,t)}{\partial r^2} \tag{7.8}$$

Where c_4 is the distance between the neutral axis of the beam and center of the sensor, Y_4 is the Young's modulus of the PVDF sensing layer and $w_k(r,t)$ is the deflection caused in the x direction by the force f on the tip of the beam. Thus, the charge generated on the electrodes is given by,

$$Q_k(t) = \int_{\Omega_k} D_{3k}(r,t) = \int_{s_{k1}}^{s_{k2}} D_{3k}(r,t) \tag{7.9}$$

where Ω_k is over the k^{th} sensor domain,

$$Q_k(t) = c_{4k} Y_4 \left(1 - \gamma \frac{d_{32}}{d_{31}}\right) \int_{s_{k1}}^{s_{k2}} \frac{\partial^2 w_k(r,t)}{\partial r^2}\, dr \tag{7.10}$$

By separate variable method, $w_i(r,t)$ can be separated as,

$$w_{ki}(r,t) = \sum_{i=1}^{\infty} \varphi_{ki}(r)\, q_{ki}(t) \tag{7.11}$$

where $\varphi_{ki}(r)$ are the eigen functions corresponding to the modal shapes and $q_{ki}(t)$ represent the modal displacement amplitudes caused by the force f(t). Applying Laplace transform and inserting the above terms on the charge equation,

$$Q_k(t) = \sum_{ki=1}^{3} c_{4k} Y_4 \left(1 - \gamma \frac{d_{32}}{d_{31}}\right) \left[\int_{s_{k1}}^{s_{k2}} \varphi''(r) dr\right] q_{ki}(t) \tag{7.12}$$

$$Q_k(s) = a \sum_{ki=1}^{3} \left[\left(\varphi_{ki}'(r)\Big|_{s_{k1}}^{s_{k2}} q_{ki}(s)\right)\right] \tag{7.13}$$

Where $a = c_{4k} Y_4 \left(1 - \gamma \frac{d_{32}}{d_{31}}\right)$

$$Q_k(s) = a \sum_{ki=1}^{3} [\varphi'_{ki}(s_{k2}) - \varphi'_{ki}(s_{k1})]\, q_{ki}(s) \tag{7.14}$$

The output voltage from the k^{th} sensor will be

$$V_k(s) = \frac{Q_k(s)}{C_k} \tag{7.15}$$

Where C_k is the equivalent circuit capacitance of the PVDF sensing layer. Thus,

$$V_k(s) = C_{sk} \sum_{ki=1}^{3} [\varphi'_{ki}(s_{k2}) - \varphi'_{ki}(s_{k1})] q_{ki}(s) \quad (7.16)$$

where $C_{sk} = \frac{c_{4k} Y_4 \left(1 - \gamma \frac{d_{32}}{d_{31}}\right)}{C_k}$

$$q_{ki}(s) = \frac{V_k(s)}{C_{sk} \sum_{ki=1}^{3} [\varphi'_{ki}(s_{k2}) - \varphi'_{ki}(s_{k1})]} \quad (7.17)$$

To find the transfer function between the output voltage and the deflection of the beam to a force applied, we take the dynamics of beam motion into account. Euler-Bernouli equation [64] for dynamic free motion / deflection of the beam with no load is given by the fourth-order differential equation [24],

$$-YI \frac{\partial^4 w_i(r,t)}{\partial r^4} + \rho A \frac{\partial^2 w_i(r,t)}{\partial t^2} = 0, \; 0 \leq r \leq L \quad (7.18)$$

where YI is the flexural rigidity, ρA is the mass per unit length. Considering synchronous motion, separation of variables can be applied to the deflection; such that, $w_i(r,t) = \sum_{i=1}^{\infty} \varphi_i(r) q_i(t)$ the above differential equation simplifies to the below,

$$\frac{d^2}{dr^2}\left[YI \frac{d^2\varphi}{dr^2}\right] = \omega_n^2 \rho A \varphi \quad ====> \quad \frac{d^4\varphi}{dr^4} - \beta^4 \varphi = 0 \quad (7.19)$$

$$\frac{d^2 Q}{dt^2} + \omega_n^2 Q = 0 \quad (7.20)$$

where $\beta^4 = \frac{\omega_n^2 \rho A}{YI}$

When a force f(t) is applied on the free end tip of the beam, the above partial differential equations for the dynamics of motion become,

$$-YI \frac{\partial^4 w_i(r,t)}{\partial r^4} + \rho A \frac{\partial^2 w_i(r,t)}{\partial t^2} = -f(t) \quad (7.21)$$

which lead to,

$$\frac{d^4\varphi}{dr^4} - \beta^4 \varphi = 0 \text{ and} \quad (7.22)$$

$$\frac{d^2 Q}{dt^2} + \omega_n^2 Q = -f(t) \quad (7.23)$$

By solving the eigenvalue problem in equation (7.22) with the appropriate boundary conditions, the eigen functions of the deflection of the beam can be obtained. $\varphi_i(r)$ represents the configuration of the beam profile. The solution to equation (7.23), $f(t)$, shows how the amplitude of the profile changes in time, with ω_n being the natural frequencies related to the infinite number of eigenvalues β. The general solution to $\frac{d^4\varphi}{dx^4} - \beta^4 \varphi = 0$ is,

$$\varphi(r) = A sin\beta r + B cos\beta r + C sinh\beta r + D cosh\beta r \quad (7.24)$$

where the constants A,B,C and D can be determined by substituting the below boundary conditions on the above general solution,

$$\varphi(0) = 0,\ YI\varphi'(0) = 0,\ YI\varphi''(L) = -f(t),\ YI\varphi'''(L) = 0 \quad (7.25)$$

Which leads to the characteristic equation,

$$cos\beta L cosh\beta L = -1 \tag{7.26}$$

which by solving numerically gives the values of βL from which ω_n^2 and the plot of the modes can be obtained. Thus, the eigen vectors with arbitrary scale are,

$$\varphi_i(r) = a_i\{(cosh\beta_i r - cos\beta_i r) - \left(\frac{(cosh\beta_i L + cos\beta_i L)}{(sinh\beta_i L + sin\beta_i L)}\right)(sinh\beta_i r - sin\beta_i r)\} \tag{7.27}$$

To derive the system's response to external forces, we consider that the eigen functions $\varphi(r)$ possess orthogonality property. Accompanied with the expansion theorem, modal analysis permits an efficient way for the derivation of the system response. To derive the orthogonality relations for the beam, we consider two distinct solutions of the eigenvalue problem, ω_p^2, $\varphi_p(r)$, ω_s^2, and $\varphi_s(r)$, that satisfy the differential equations,

$$\frac{d^2}{dr^2}\left[YI\frac{d^2\varphi_p(r)}{dr^2}\right] = \omega_p^2 \rho A \varphi_p(r)$$

and

$$\frac{d^2}{dr^2}\left[YI\frac{d^2\varphi_s(r)}{dr^2}\right] = \omega_s^2 \rho A \varphi_s(r) \tag{7.28}$$

Multiplying equation (7.27) by $\varphi_s(r)$ and integrating over the length of the beam,

$$\int_0^L \varphi_s(r)\frac{d^2}{dr^2}\left[YI\frac{d^2\varphi_p(r)}{dr^2}\right]dr = \int_0^L \varphi_s(r)\,\omega_p^2\rho A\varphi_p(r)dr \tag{7.29}$$

Integrating by parts the left side,

$$\int_0^L \varphi_s(r)\frac{d^2}{dr^2}\left[YI\frac{d^2\varphi_p(r)}{dr^2}\right]dr$$

$$= \left\{\varphi_s(r)\frac{d}{dr}\left\{YI\frac{d^2\varphi_p(r)}{dr^2}\right\}\Big|_0^L\right\} - \left\{\frac{d\varphi_s(r)}{dr}\left\{YI\frac{d^2\varphi_p(r)}{dr^2}\right\}\Big|_0^L\right\} + \int_0^L YI\frac{d^2\varphi_s(r)}{dr^2}\frac{d^2\varphi_p(r)}{dr^2}dr \tag{7.30}$$

Applying the boundary conditions from equation (7.25), we get,

$$YI\varphi_s'(L)\varphi_p''(L) + \int_0^L YI\frac{d^2\varphi_s(r)}{dr^2}\frac{d^2\varphi_p(r)}{dr^2}dx = \omega_p^2\int_0^L \rho A\,\varphi_p(r)\varphi_s(r)dr \tag{7.31}$$

Similarly, from equation (7.28) we get,

$$YI\varphi_p'(L)\varphi_s''(L) + \int_0^L YI\frac{d^2\varphi_s(r)}{dr^2}\frac{d^2\varphi_p(r)}{dr^2}dr = \omega_s^2\int_0^L \rho A\,\varphi_p(r)\varphi_s(r)dr \tag{7.32}$$

Subtracting equations (7.31) and (7.32),

$$\left(\omega_p^2 - \omega_s^2\right)\int_0^L \rho A\,\varphi_p(r)\varphi_s(r)dr = 0 \tag{7.33}$$

$$=== > \int_0^L \rho A\, \varphi_p(r)\varphi_s(r)dr = 0 \text{ ,p,s=1,2……,} \omega_p^2 \neq \omega_s^2 \quad (7.34)$$

(for two distinct solutions of the eigenvalue problem), represents the orthogonality relations for the beam in bending due to external force. Alternate orthogonality relations are also, $\int_0^L \varphi_s(r) \frac{d^2}{dr^2}\left[YI \frac{d^2\varphi_p(r)}{dr^2}\right] dr = 0$ and

$$YI\varphi_s'(L)\varphi_p''(L) + \int_0^L YI \frac{d^2\varphi_s(r)}{dr^2}\frac{d^2\varphi_p(r)}{dr^2} dr = 0 \quad (7.35)$$

The natural modes derived from the characteristic solution can be normalized so as to satisfy

$$\int_0^L \rho A\, \varphi_p^2(r)dr = 1, p = 1,2 \ldots\ldots \quad (7.36)$$

in which case, they are referred to as normal modes and they satisfy the orthonormality relations,

$$\int_0^L \rho A\, \varphi_p(r)\varphi_s(r)dr = \delta_{ps} \quad (7.37)$$

The alternate orthonormality relations are

$$YI\varphi_s'(L)\varphi_p''(L) + \int_0^L YI \frac{d^2\varphi_s(r)}{dr^2}\frac{d^2\varphi_p(r)}{dr^2} dr = \omega_p^2\delta_{ps} \text{ and}$$

$$\int_0^L \varphi_s(r) \frac{d^2}{dr^2}\left[YI \frac{d^2\varphi_p(r)}{dr^2}\right] dr = \omega_p^2\delta_{ps} \quad (7.38)$$

from which the expansion theorem can be used to state that the $\varphi(r)$ is continuous and can be expanded in the absolute and uniform convergent series of eigenfunctions,

$$\varphi(r) = \sum_{p=1}^{\infty} c_p \varphi_p(r) \tag{7.39}$$

where the constant coefficients are $c_p = \int_0^L \rho A \varphi_p(r) \varphi(r) dr$

Above forms the basis for modal analysis from which the system response for external force can be determined as below.

The partial homogenous differential equation of motion of the beam is,

$$-\frac{\partial^2}{\partial^2 r}\left[YI \frac{\partial^2 w(r,t)}{\partial^2 r}\right] = \rho A \frac{\partial^2 w(r,t)}{\partial t^2}, 0 \leq r \leq L \tag{7.40}$$

Since the concentrated external force F(t) applied at the beam tip has the nonhomogenous boundary condition, $YIw'(L,t) = F(t)$, modal analysis cannot be used. To solve this problem, the differential equation can be made nonhomogenous, thereby rendering the boundary condition homogenous ($YIw'(L,t) = 0$). This can be done by treating the concentrated force as distributed force over a small segment such that,

$$f(x,t) = F(t)\delta(a - L) \tag{7.41}$$

Where $\delta(a - L)$ is the Diral delta function. Rewriting the equation of motion with the external force,

$$-\frac{\partial^2}{\partial^2 r}\left[YI \frac{\partial^2 w(r,t)}{\partial^2 r}\right] + F(t)\delta(a - L) = \rho A \frac{\partial^2 w(r,t)}{\partial t^2}, 0 \leq r \leq L \text{ and } a_1 \leq a \leq a_2 \tag{7.42}$$

Using the orthonormality relations derived earlier and separation of variables, $w_i(r,t) = \sum_{i=1}^{\infty} \varphi_i(r)\, q_i(t)$, the equation of motion of the viscously damped infinite-degrees-of freedom system can be rewritten as,

$$\ddot{q_i}(t) + 2\zeta_i\omega_i\dot{q_i}(t) + \omega_i^2 q_i(t) = N_i(t), i = 1,2 \ldots . n \tag{7.43}$$

where $N_i(t) = \int_0^L \varphi_i(x)F(t)\,\delta(a-L)dx = \varphi_i(L)F(t)$ (7.44)

represent the modal forces and ζ_{ki} represent viscous damping factors. Then the solution of the modal equations in the form of convolution integrals is,

$$q_i(t) = \frac{1}{\omega_d}\int_0^t N_i(t-\tau)e^{-\zeta_i\omega_i\tau}sin\omega_d\tau d\tau = \frac{\varphi_i(L)}{\omega_d}\int_0^t F(t-\tau)e^{-\zeta_i\omega_i\tau}sin\omega_d\tau d\tau\,,$$

$$where\ i = 1,2 \ldots and\ \omega_{d=}(1\zeta_i^{\,2})^{1/2}\ \omega_i\ is\ the\ frequency\ of\ dampled\ oscillations \tag{7.45}$$

The deflection response to the external force is thus,

$$w_i(r,t) = \sum_{i=1}^{\infty}\varphi_i(r)\, q_i(t) = \sum_{i=1}^{\infty}\varphi_i(r)\frac{\varphi_i(L)}{\omega_d}\int_0^t F(t-\tau)e^{-\zeta_i\omega_i\tau}sin\omega_d\tau d\tau,$$

Where i=1,2….. (7.46)

Taking Laplace transform of $q_i(t)$ in equation (7.45),

$$q_i(s) = \frac{\sum_{i=1}^{\infty}\varphi_i(L)F(s)}{[s^2+2\zeta_i\omega_i s+\omega_i^2]} \tag{7.47}$$

$$F(s) = \frac{q_i(s)\left[s^2+2\zeta_i\omega_i s+\omega_i^2\right]}{\sum_{i=1}^{\infty}\varphi_i(L)} \tag{7.48}$$

$$q_i(s) = \frac{\sum_{i=1}^{\infty}\varphi_i(L)F(s)}{\left[s^2+2\zeta_i\omega_i s+\omega_i^2\right]} \tag{7.49}$$

Equating equations (7.17) and (7.49),

$$\frac{V_k(s)}{C_{sk}\sum_{ki=1}^{3}[\,\varphi'_{ki}(s_{k2})-\,\varphi'_{ki}(s_{k1})]} = \frac{\sum_{i=1}^{\infty}\varphi_i(L)F(s)}{\left[\left[s^2+2\zeta_i\omega_i s+\omega_i^2\right]\right]} \tag{7.50}$$

Thus, the transfer function of the system is given by,

$$\frac{V_k(s)}{F(s)} = \frac{C_{sk}\sum_{ki=1}^{3}\sum_{i=1}^{\infty}\varphi_i(L)[\,\varphi'_{ki}(s_{k2})-\,\varphi'_{ki}(s_{k1})]}{\left[\left[s^2+2\zeta_i\omega_i s+\omega_i^2\right]\right]} \tag{7.51}$$

The piezoelectric sensors have high output impedance [58] and most of the measuring devices have much lower input impedance, in the order of megaohms. Also the output of the piezoelectric sensors are in the order of mVolts. So the output from the piezoelectric sensor must be interfaced with a signal conditioning system so as to accurately measure the output from the sensor. The main purpose of this signal conditioning interface is to provide high input impedance to the sensor and at the same time provide a signal with a low output impedance.

The signal conditioning unit consist of a voltage follower and an operational amplifier [59]; and since PVDF has high pass characteristic, the overall output from the k^{th} sensor $V_{ko}(s)$ is given by,

$$V_{ko}(s) = \frac{sRC_k}{1+sRC_k} * \left(1 + \frac{R_2}{R_1}\right) * \frac{V_k(s)}{F(s)} \quad (7.52)$$

where C_k is the equivalent capacitance of the PVDF layer and R is the input impedance of the operational amplifier, and R_1 and R_2 are the resistors involved in amplifier gain. The output voltage from the k^{th} sensor is derived as,

$$V_{ko}(s) = \frac{sRC_k}{1+sRC_k} * \left(1 + \frac{R_2}{R_1}\right) * \frac{C_{sk} \sum_{ki=1}^{3} \sum_{i=1}^{\infty} \varphi_i(L) \left[\varphi_i'(s_{k2}) - \varphi_i'(s_{k1}) \right]}{\left[s^2 + 2\zeta_i \omega_i s + \omega_i^2 \right]} * F(s) \quad (7.53)$$

Where $C_{sk} = \frac{c_{4k} Y_4 \left(1 - \gamma \frac{d_{32}}{d_{31}}\right)}{C_k}$

The above transfer function can be used to obtain the applied force (pressure) on the beam. For modelling verification, 5 modes for 3 sensor strips are implemented in this work.

7.2 Simulation

7.2.1 Equal Striped Sensing Beam

The above derived model of the cantilever sensing beam is simulated using MATLAB. The MATLAB code computes the deflection of the beam when a force is applied onto the free end of the beam. It further computes and

plots the voltage generated from each sensor strip when the force is applied. The input force applied is unit step function and analyses are done for three different dimensions' beams with 5 piezoelectric sensor strips placed on the beam. Further for each beam, the analyses are done with equal length sensor strips and gaps followed by varying sensor strips and gaps.

The simulation design specifications are done in a way to close replicate the actual sensor's active area. The first simulated composite beam's dimensions are 60 mm in length, 5 mm in width and 0.2 mm in thickness.

Five PVDF sensor strips are placed in equal distance on the beam. The strips are 5 mm wide each. The density (ρ), elastic modulus (Y) and Poisson ratio (γ) for the sensor and beam are the following values. The beam layer's values are ρ as $1.35 * 10^3 kg/m^3$, Y as $3.8 * 10^9 Pa$ and γ as 0.4 , similar to Polyster. The PVDF sensor layer's values are ρ as $1.78 * 10^3 kg/m^3$, Y as $3 * 10^9 Pa$ and γ as 0.34. For a force of unit step, the deflection response and the corresponding voltages on the 5 sensors are shown in the below Figures 7.2 and 7.3 respectively.

From the sensor voltage plot, it is seen that the sensor close towards the clamped end (sensor 5), produces higher voltage proportional to the stress generated along the beam. This also verifies the stress and strain analysis

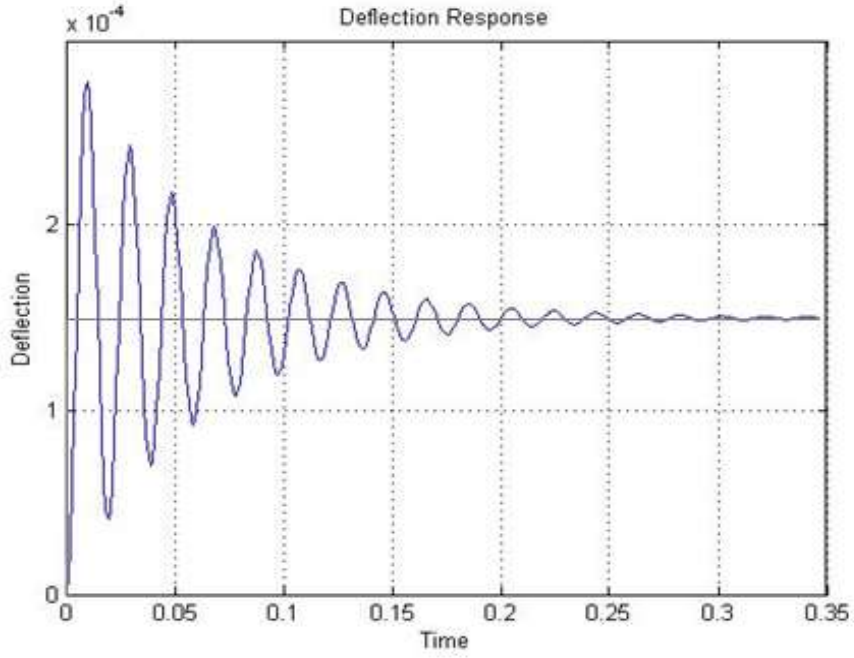

Figure 7.2: Deflection response of the beam to unit step force for beam dimensions: L:60 mm, W: 5 mm, T: 0.2 mm and 5 mm length sensor strips

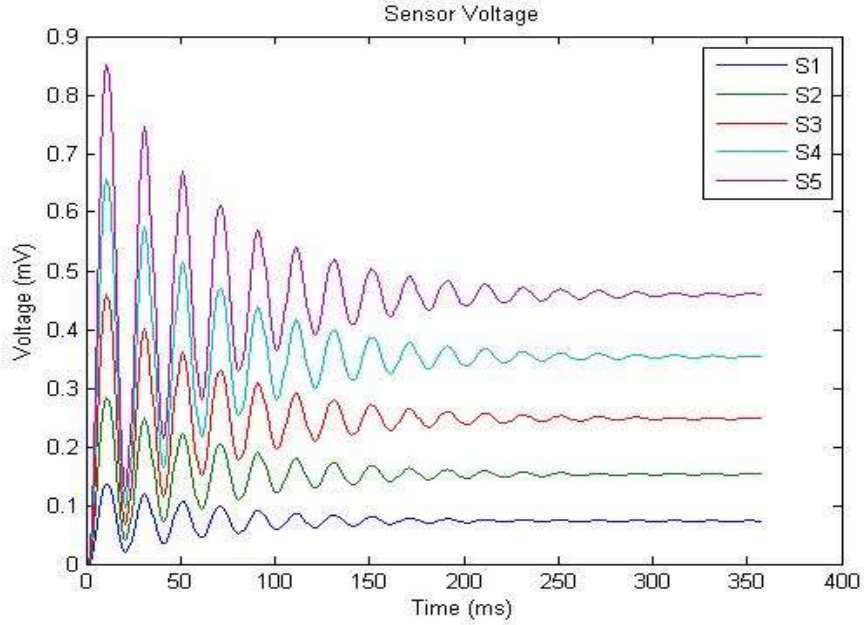

Figure 7.3: Voltage response of the Sensor Strips to unit step force from 5 sensors on the beam with S1 on free end and S5 on clamped end, and for beam dimensions: L:60 mm, W: 5 mm, T: 0.2 mm and 5 mm length sensor strips

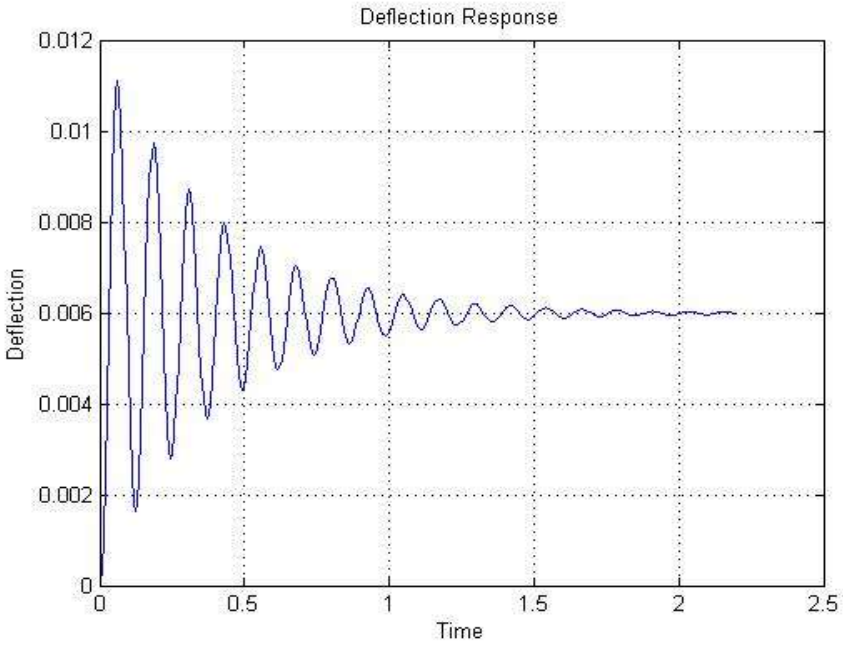

Figure 7.4: Deflection response of the beam to unit step force for beam dimensions: L:60 mm, W: 1mm, T: 0.1 mm and 5 mm length sensor strips

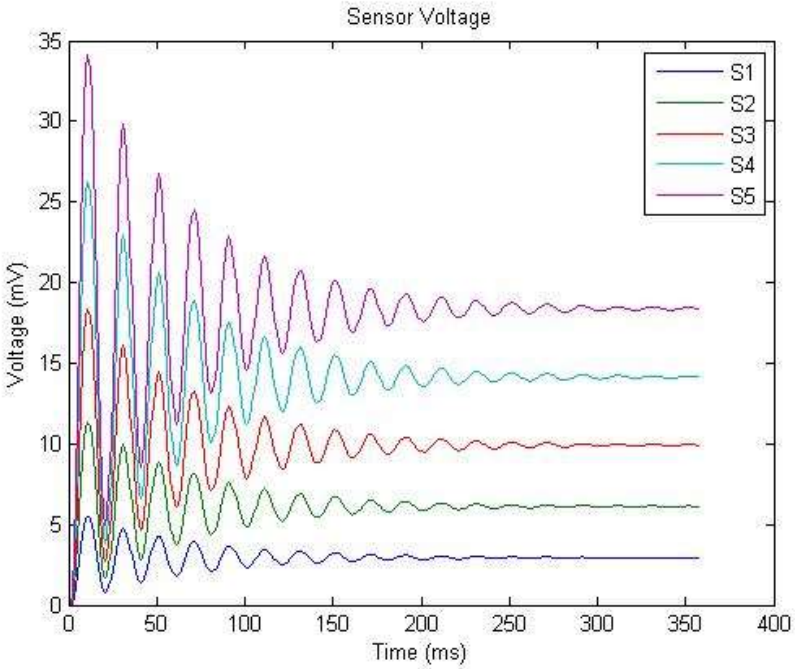

Figure 7.5: Voltage response of the Sensor Strips to unit step force from 5 sensors on the beam with S1 on free end and S5 on clamped end, and for beam dimensions: L:60 mm, W: 1 mm, T: 0.1 mm and 5 mm length sensor strips

of the beam done on Ansys which shows that more stress is seen on the clamped end, while deflecting. The analysis was done on the same 60mm length beam with 1mm width and 0.1 mm thickness. With a less thick beam, the deflection and the voltage increased as below in Figures 7.4 and 7.5 respectively. The same was repeated with different dimension beams to check the validity. The second set of beam's dimensions are 30 mm in length, 2 mm in width and 0.1 mm in thickness; and 30mm in length, 1mm in width and 0.05 mm in thickness. Five PVDF sensor strips are placed in equal distance on the beam. The strips are 3 mm wide each. The third set of beam's dimensions are 10 mm in length, 0.5 mm in width and 0.05 mm in thickness; and 10 mm in length, 0.2 mm in width and 0.02 mm in thickness. Five PVDF sensor strips are placed in equal distance on the beam. The strips are 1 mm wide each. Deflection and voltage response are shown in Figures 7.6 and 7.7 respectively. As the dimensions decreased the deflection and voltage increased. For comparison, the plots for the third set of beam dimensions are shown in the Figures 7.8 and 7.9 respectively. Once again, lower dimensions produce higher voltages. Longer, narrower and thinner beam produce more deflection and is more sensitive, thereby producing higher sensor output voltages.

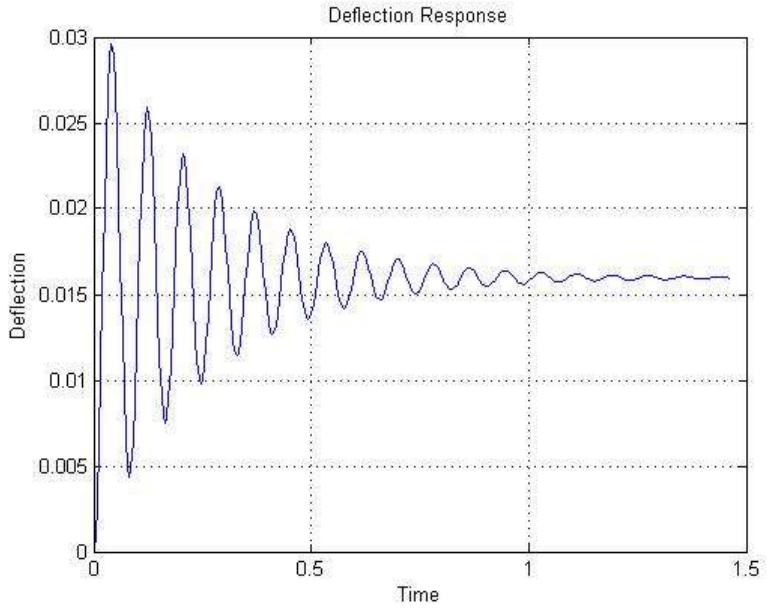

Figure 7.6: Deflection response of the beam to unit step force for beam dimensions: L:10 mm, W: 0.5 mm, T: 0.05 mm and 1 mm length sensor strips

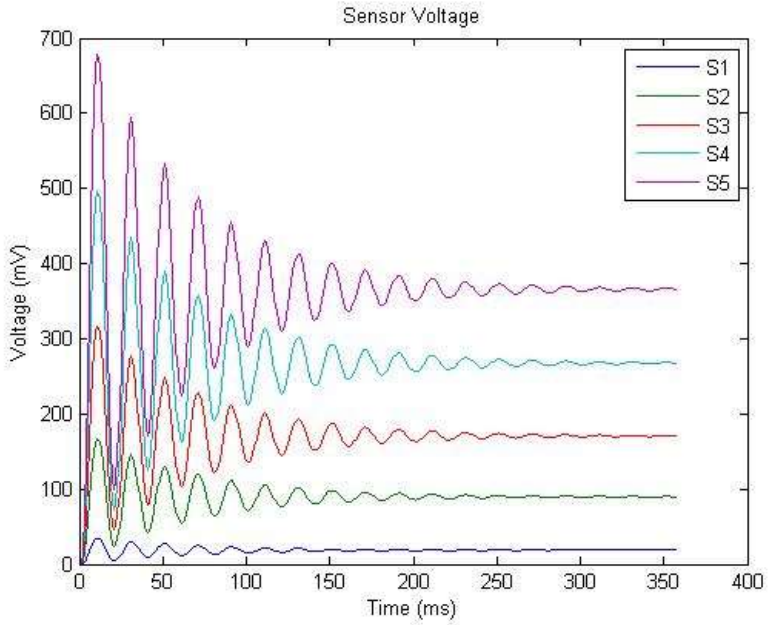

Figure 7.7: Voltage response of the Sensor Strips to unit step force from 5 sensors on the beam with S1 on free end and S5 on clamped end, and for beam dimensions: L:10 mm, W: 0.5 mm, T: 0.05 mm and 1 mm length sensor strips

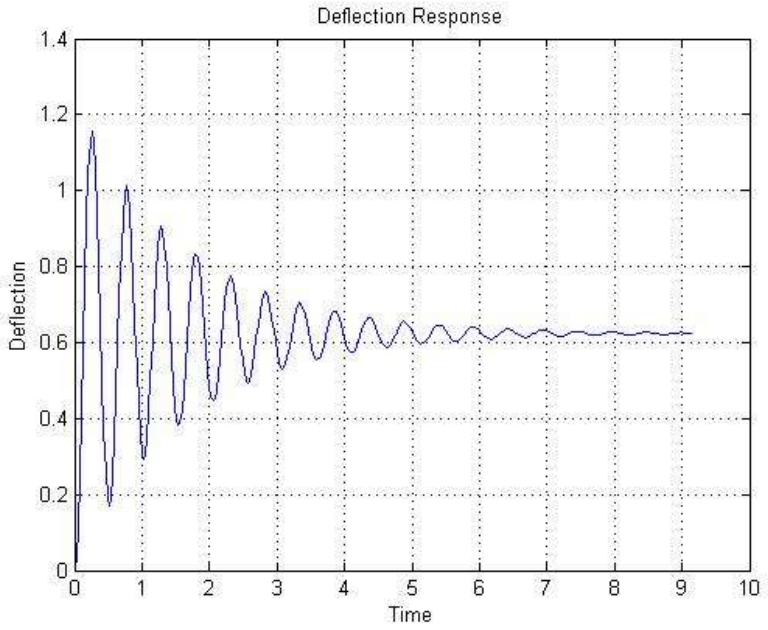

FFigure 7.8: Deflection response of the beam to unit step force for beam dimensions: L:10 mm, W: 0.2 mm, T: 0.02 mm and 1 mm length sensor strips

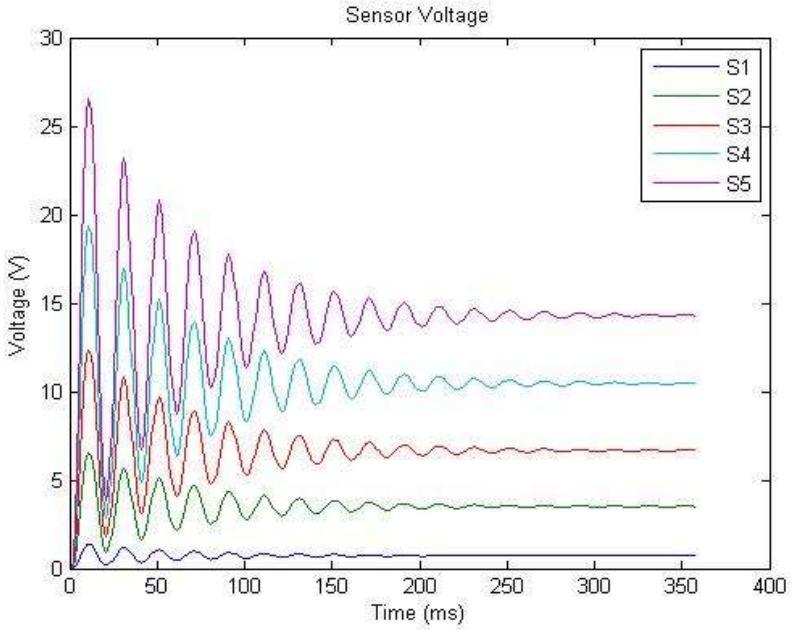

Figure 7.9: Voltage response of the Sensor Strips to unit step force from 5 sensors on the beam with S1 on free end and S5 on clamped end, and for beam dimensions: L:10 mm, W: 0.2 mm, T: 0.02 mm and 1 mm length sensor strips

7.2.2. Unequal Striped Sensing Beam

In order to match the sensitivity of all sensors along the beam, sensing strip area is varied. This is done to identify an optimal design configuration for a beam that can have sensors producing a similar voltage along the length thereby having a similar sensitivity. By using a varying length sensor design with the narrowest sensor towards the clamped end and broadest one towards the free end, as shown in figure 6.26, similar voltage generation from all 5 sensors are obtained. Below in Figures 7.10, 7.11, 7.12 and 7.13, are the plots for the varying length beams with varying sensor lengths.

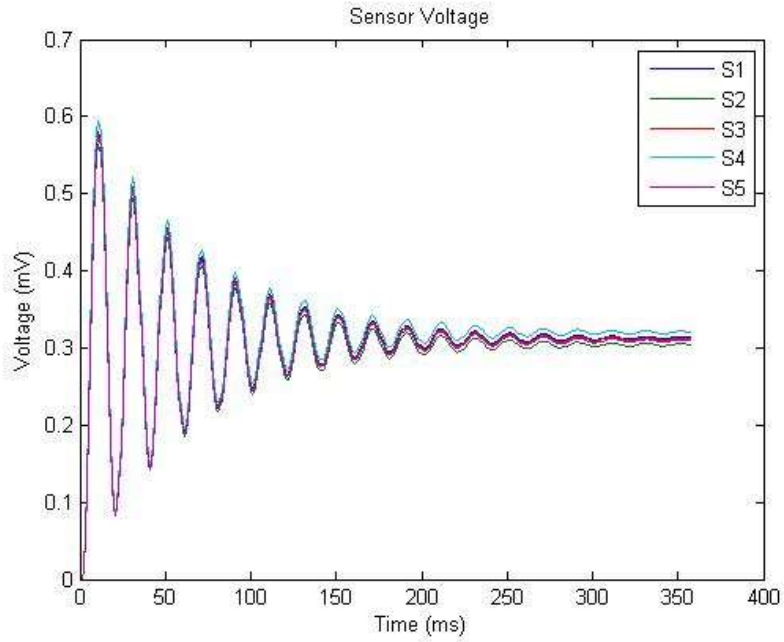

Figure 7.10: Output sensor voltages from 5 sensors of varying length (narrowest to clamped end) for L: 60 mm, W: 5 mm and T:0.2 mm

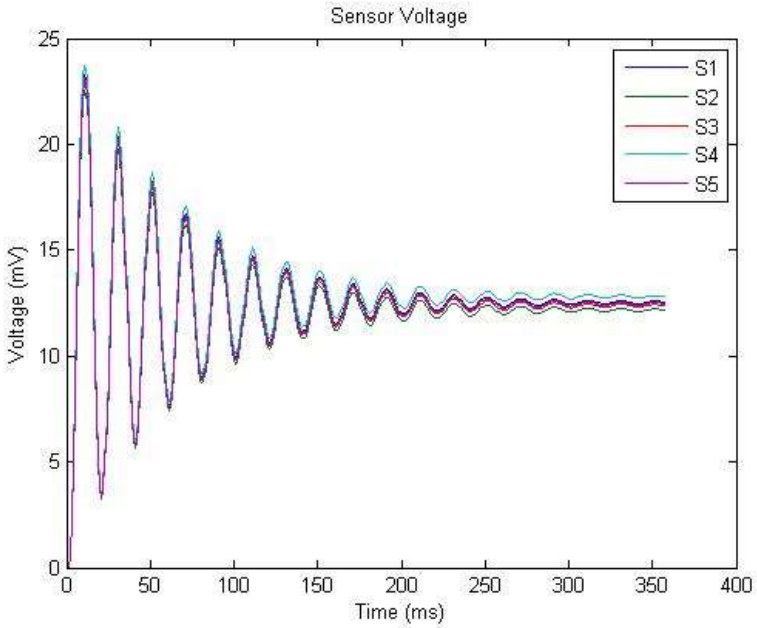

Figure 7.11: Output sensor voltages from 5 sensors of varying length (narrowest to clamped end) for L: 60 mm, W: 1 mm and T:0.1 mm

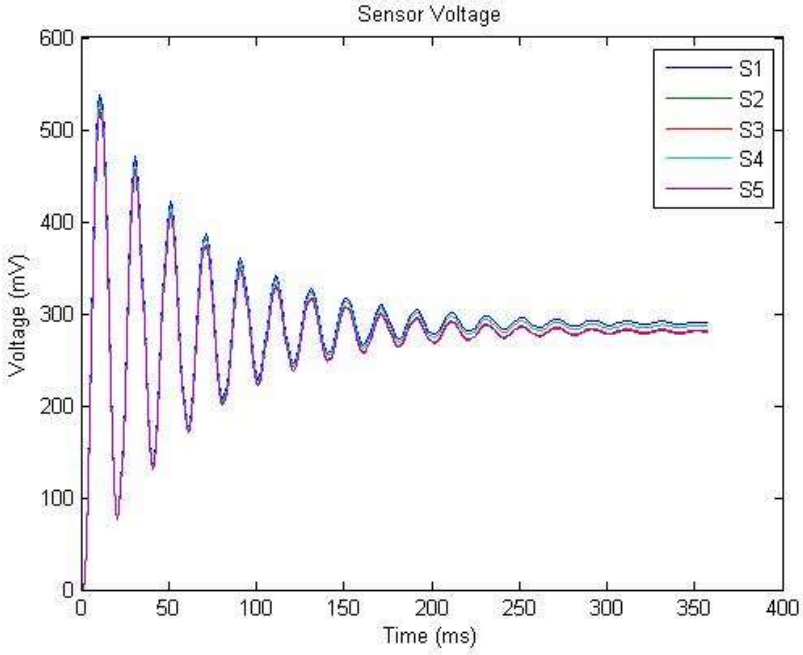

Figure 7.12: Output sensor voltages from 5 sensors of varying length (narrowest to clamped end) for L: 10 mm, W: 0.5 mm and T:0.05 mm

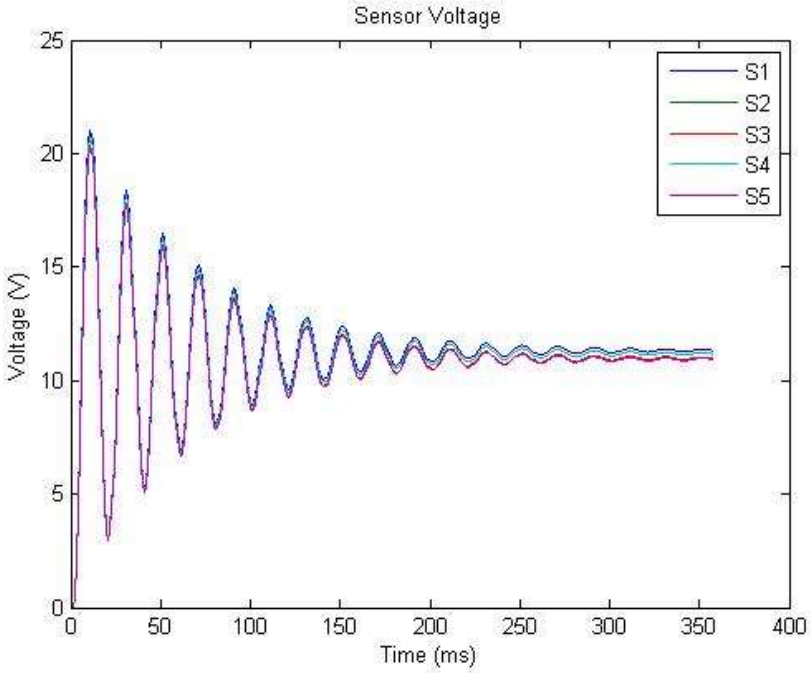

Figure 7.13: Output sensor voltages from 5 sensors of varying length (narrowest to clamped end) for L: 10 mm, W: 0.2 mm and T:0.02 mm

Longer, narrower and thinner beam produce more deflection and is more sensitive, thereby producing higher, yet similar sensor output voltages.

Chapter 8

Bio-Inspired Pressure Sensor: Experiments and Analysis

With the simulation work showing convincing results, the work extends in structuring the setup for experimental analysis. For this work, the structure is designed in macro-scale. It can be made in micro-scale for future work, but, however, it is not within the scope of this work.

8.1 Mechanical Amplification Structure and Sensing Beam

The mechanical structure and the beam parts are designed in Solidworks. The 3D printing of the parts is done using Shapeways manufacturers. The parts are shown in the below Figure 8.1. All parts are made with strong and flexible plastic. The mechanical and tensile properties include bulk density of 0.45 g/cm^3, tensile modulus of 1700 MPa and tensile strength of 48 MPa. The pole has a dimension of 1 cm * 0.998 cm, material volume of 0.1875 cm^3 and surface area of 3.6649 cm^2. The horizontal link has a

dimension of 0.5 cm * 0.35 cm * 4.6 cm, material volume of 0.5405 cm^3 and surface area of 7.4975 cm^3. The vertical link has a dimension of 0.27 cm * 0.3 cm * 2.35 cm, material volume of 0.0574 cm^3 and surface area of 1.3434 cm^3. The beam has a dimension of 12 cm * 0.1 cm * 1.3 cm, material volume of 1.5340 cm^3 and surface area of 33.6235 cm^3.

The entire mechanical structure along with the beam on which the PVDF sensor strips are to be glued, in assembled form, is shown in below Figure 8.2.

The cross-sectional surface area of the circular part of the pole is made approximately 2.7 times larger than the cross-sectional surface area of the top of the vertical link. This corresponds to the area ratio transformation of the tympanic membrane verses the stapes of the middle ear amplification part.

Along with that, the horizontal link is mounted for support in 1:3 ratio part, so that it has a lever mechanism with an increase in displacement by 3 times on the vertical link end. This corresponds to the lever mechanism between the three middle ear bones'; malleus, incus and stapes.

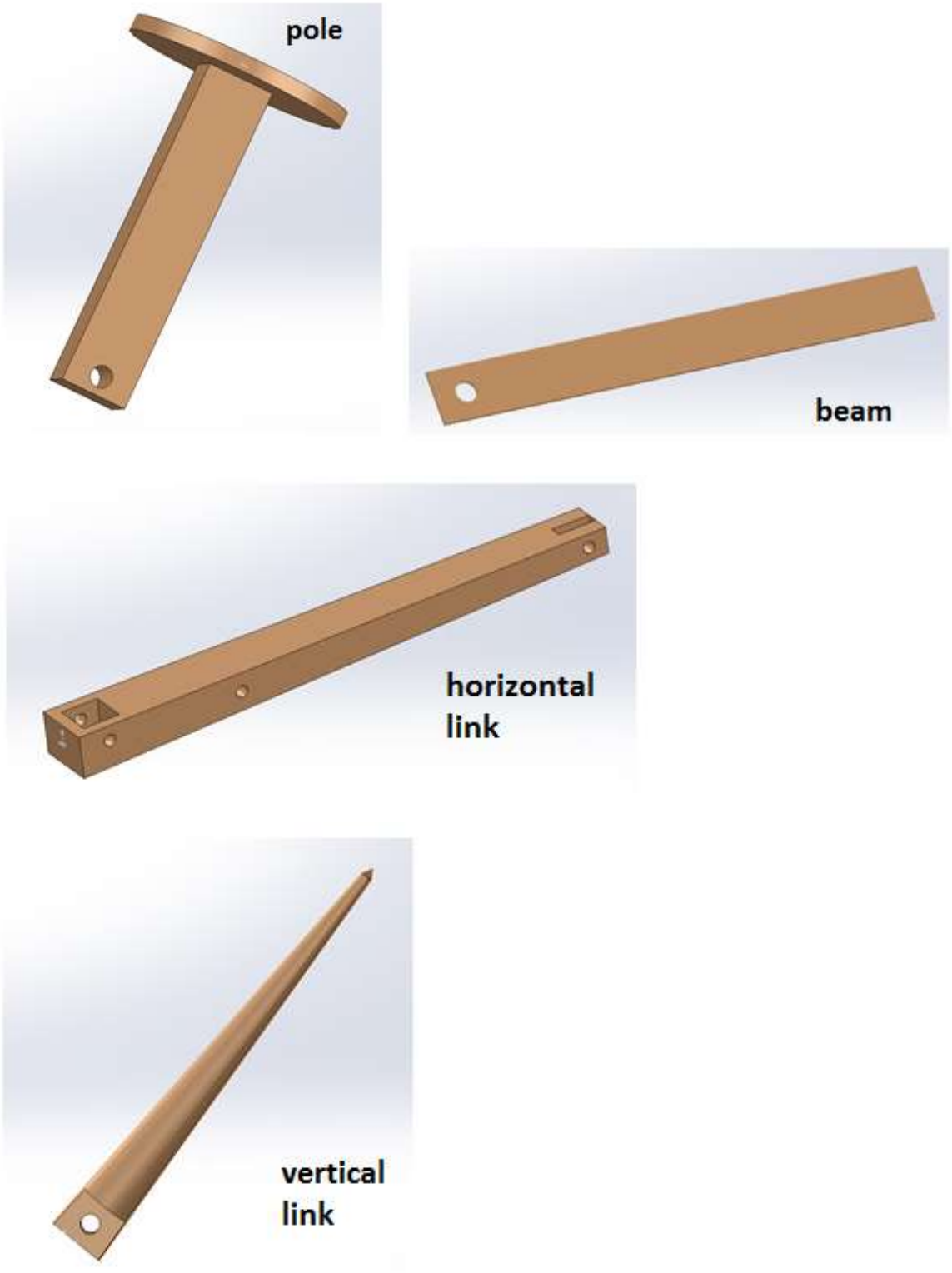

Figure 8.1: Parts that form the mechanical structure of the design

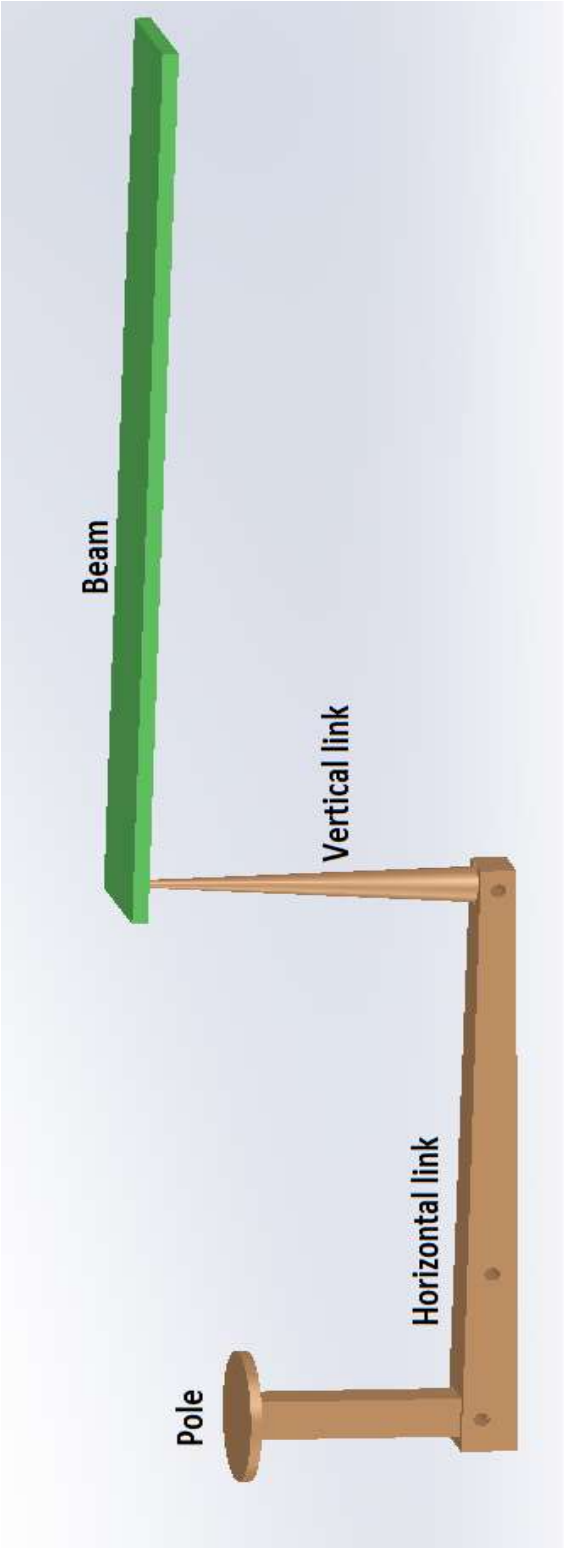

Figure 8.2: Block diagram of the entire mechanical structure in assembled form with the beam

Overall amplification of the designed mechanical structure thus adds up to approximately 6 times amplification, which is given by the below mechanical amplification (MA) equation,

$$MA = \left[\left(\frac{SA\ of\ pole}{SA\ of\ vertical\ link\ tip}\right) + \left(\frac{Distance\ from\ mount\ to\ right\ end\ of\ horizontal\ link}{Distance\ from\ left\ end\ of\ horizontal\ link\ to\ mount}\right)\right] \quad (8.1)$$

Thus, the model transfer function in Chapter 6 now leads to another term to incorporate the amplification part due to the mechanical structure design.

The model transfer function without the mechanical structure design from chapter 6 is,

$$V_{ko}(s) = \frac{sRC_k}{1+sRC_k} * \left(1+\frac{R_2}{R_1}\right) * \frac{C_{sk}\sum_{ki=1}^{\infty}\sum_{i=1}^{\infty}\varphi_i(L)\left[\ \varphi_i'(s_{k2}) - \ \varphi_i'(s_{k1})\right]}{\left[\left[s^2 + 2\zeta_{ki}\omega_{ki}s + \omega_{ki}^2\right]\right]} * F(s) \quad (8.2)$$

where $C_{sk} = \frac{c_{4k}Y_4\left(1-\gamma\frac{d_{32}}{d_{31}}\right)}{C_k}$

Equation (8.2) is the model transfer function equation for without the mechanical structure design.

Incorporating the mechanical amplification to the above equation,

$$V_{ko}(s) = MA * \frac{sRC_k}{1+sRC_k} * \left(1+\frac{R_2}{R_1}\right) * \frac{C_{sk}\sum_{ki=1}^{\infty}\sum_{i=1}^{\infty}\varphi_i(L)\,[\ \varphi_i'(s_{k2}) - \ \varphi_i'(s_{k1})]}{\left[[s^2 + 2\zeta_{ki}\omega_{ki}s + \omega_{ki}^2]\right]} * F(s) \quad (8.3)$$

where $C_{sk} = \frac{c_{4k}Y_4\left(1-\gamma\frac{d_{32}}{d_{31}}\right)}{C_k}$ and

MA = $[\left(\frac{SA\ of\ pole}{SA\ of\ vertical\ link\ tip}\right) + \left(\frac{Distance\ from\ mount\ to\ right\ end\ of\ horizontal\ link}{Distance\ from\ left\ end\ of\ horizontal\ link\ to\ mount}\right)]$

Equation (8.3) is the model transfer function equation for with the mechanical structure design.

8.2 Amplification and Conditioning Circuitry

The piezoelectric sensors have high output impedance [58] and most of the measuring devices have much lower input impedance, in the order of megaohms. Also, the output of the piezoelectric sensors is in the order of mVolts. So the output from the piezoelectric sensor must be interfaced with a signal conditioning system so as to accurately measure the output from the sensor. The main purpose of this signal conditioning interface is to provide high input impedance to the sensor and at the same time provide a signal with a low output impedance.

The electrical representation of the piezoelectric sensor [58] is a charge generator parallel to a capacitor, which has a capacitance equal to that of

the sensor. The sensor generates a charge when mechanically stressed, but the charge leaks off, when it is deflected and held in place. This charge leak is also due to the presence of some finite leakage resistance in the piezoelectric material. Due to this charge leakoff, although the time constant can be made large to account for low frequency operations, piezoelectric sensors cannot be used in static condition. The piezoelectric capacitance is inversely proportional to the sensitivity of the circuit and therefore for a certain strain, when the capacitance is increased to increase the time constant, the output voltage becomes weaker in the order of mVolts and this makes piezoelectric sensors unsuitable for static conditions.

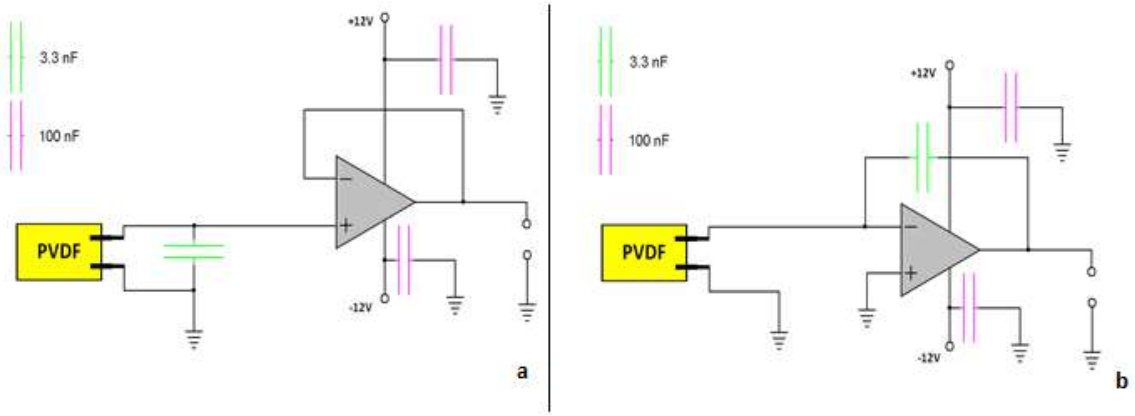

Figure 8.3: Circuitry in (a): voltage follower and (b): charge amplifier mode

Ricks and Shen [65] studied the interfacing circuitry for piezoelectric sensors by constructing the ultralow-input bias current operational amplifier AD549 (Analog Devices, Inc.) with high input impedance Rin=

10^{13} Ω and low-bias current 150fA, as a voltage follower and charge amplifier, as shown in Figure 8.3, both in static and dynamic mode.

The output voltage of the voltage follower, $V_{o,v}$, and charge amplifier, $V_{o,c}$, circuits can be determined using their respective equations as below,

$$V_{o,v} = \frac{Q}{C_o + C_{pvdf}} \quad \text{and} \quad V_{o,c} = \frac{Q}{C_o} \tag{8.4}$$

The static testing is performed by applying a constant deflection to a piece of PVDF film and measuring the voltage output over a period of approximately 100 seconds at a sampling rate of approximately 2.5 Hz. The output is measured using the GW-Instek GDS-2102 model oscilloscope and FreeWave software. The purpose of the static testing is to measure signal decay and to compare the performances of the voltage follower and charge amplifier circuitry.

Each test is performed with three identical circuit constructions at an ambient temperature of 20°C, as shown in Figure 8.4. Both the voltage follower and charge amplifier circuitry show an unexpected ability to maintain a steady output voltage. The voltage follower circuitry displayed slight initial signal decay over a period of approximately 20 seconds, before displaying a steady value. The charge amplifier circuitry did not exhibit the same trend of signal bleed off as the voltage follower, but displayed a higher degree of noise when compared to the voltage follower. To perform

the dynamic testing, the PVDF film is initially held in a deflected position then released at the onset of measurement. The dynamic test is done for the voltage follower circuit due to the reduced noise seen in the static test.

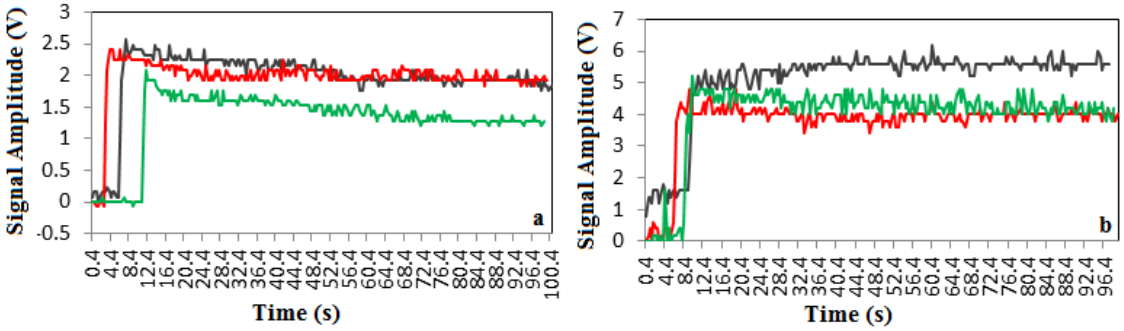

Figure 8.4: Static test for (a): voltage follower and (b): charge amplifier circuitry

The signal is measured using a data acquisition device from Measurement Computing, the PCI-DAS6025. After each deformation, the circuit displayed an offset value differing from the initial value at a relaxed state but is able to hold the charge, as shown in Figure 8.5.

The same group [65] also studied the hysteresis and temperature drift of the PVDF. Hysteresis is studies with the same 25mm PVDF for varying displacements. The output voltages generated for larger deflections of -3mm to +3 mm and smaller displacements of -0.2mm to +0.2 mm are

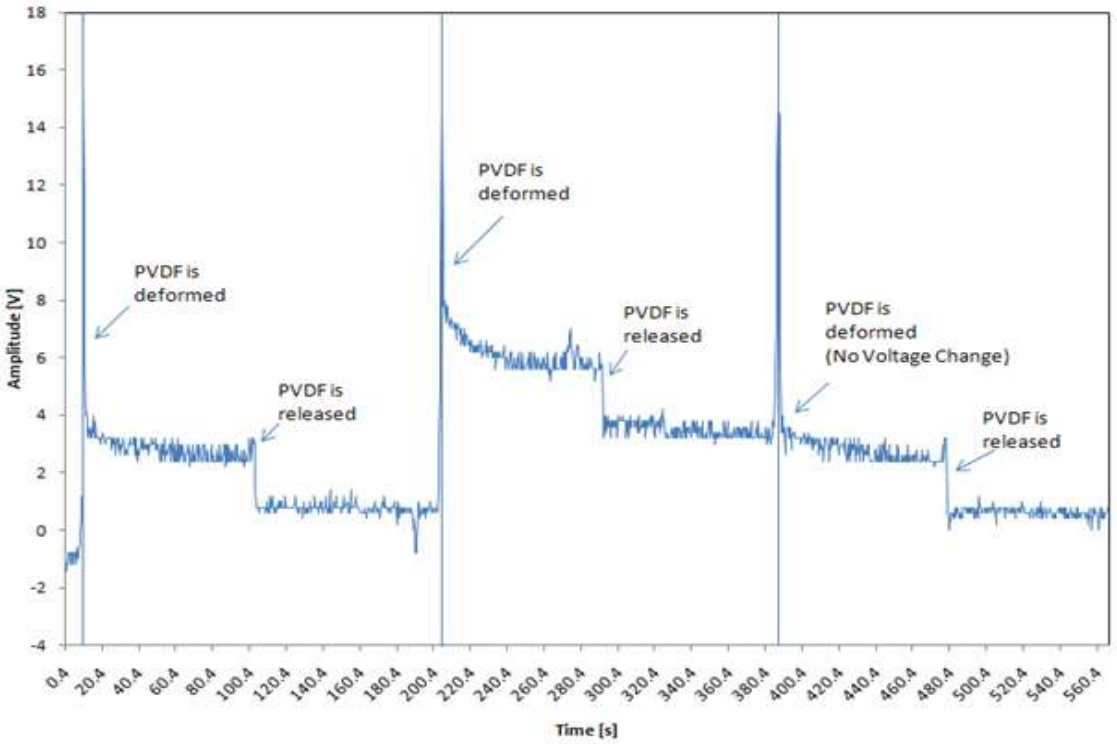

Figure 8.5: Dynamic test with voltage follower circuitry

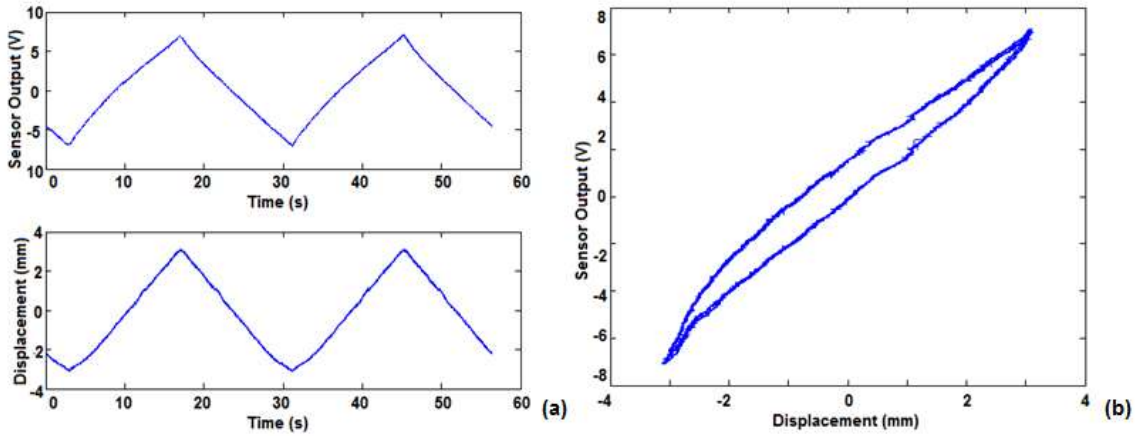

Figure 8.6: (a): Input displacement and output voltage for large displacement, (b): Input displacement – output voltage hysteresis curve for -3 - +3 mm deflection

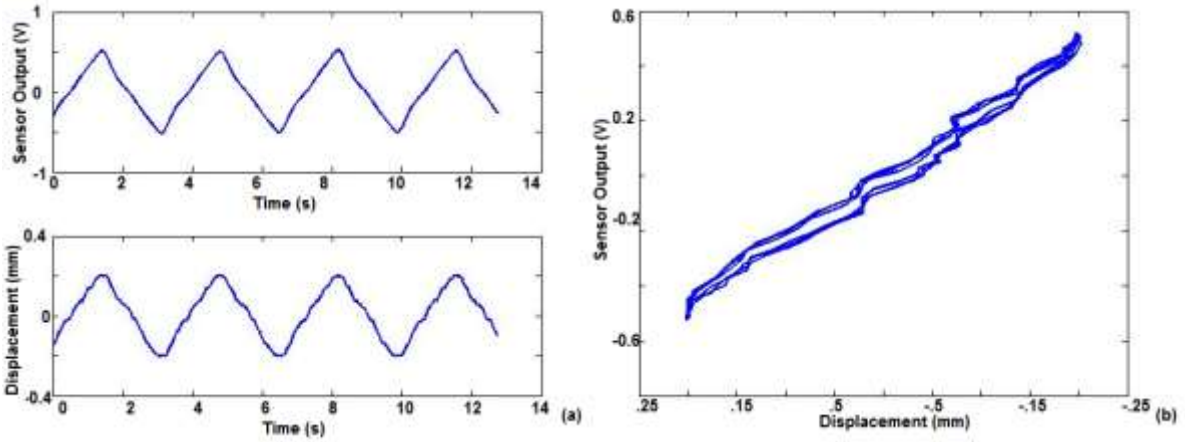

Figure 8.7: (a): Input displacement and output voltage for small displacement, (b): Input displacement – output voltage hysteresis curve for -0.2 - +0.2 mm deflection

shown in the Figures 8.6 and 8.7 respectively. Their corresponding input displacement to output voltage hysteresis curves are also shown. As seen, for less displacements the hysteresis is minimized and can be kept in an accepted range. This minimizing the hysteresis can be adopted in our application.

PVDF sensors also have their inherent temperature sensitive property of being pyroelectric, where the PVDF generates charge for temperature change. Ricks and Shen studied the charge generation for temperature change from 19 to 28°C and also used a differentiation circuit for temperature drift compensation. In order to account for the environmental noise, a differential circuit is introduced using a second piece of PVDF as a control for temperature disturbances, as shown in the following Figure

8.8. The PVDF circuitry used for control uses a potentiometer to allow for adjustment to its output voltage. The output voltage of the circuitry in its entirety is given by the following equation:

$$V_{out_{Differentiation}} = \frac{R_4}{R_3}\cdot\left[V_{signal}\cdot\left(1+\frac{R_2}{R_1}\right) - V_{control}\left(1+\frac{R_{POT}}{R_1}\right)\right] \tag{8.5}$$

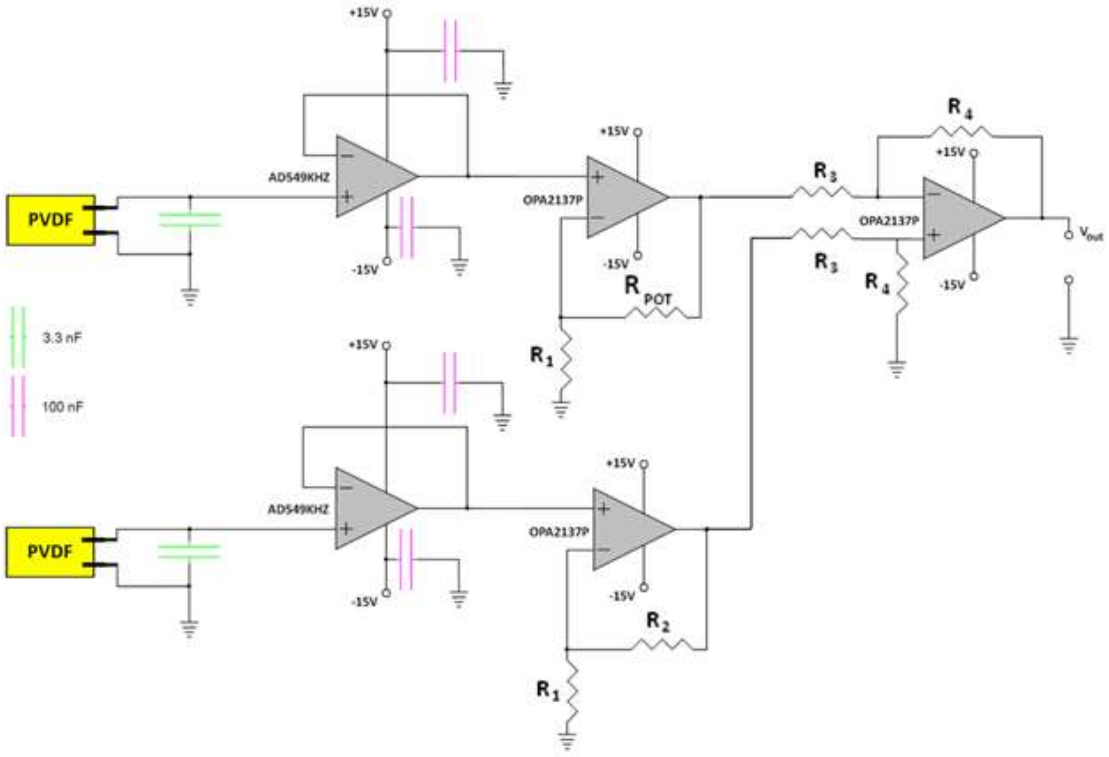

Figure 8.8: Temperature drift compensation differentiation circuitry

where R_1, R_2, R_3, R_4 represent constant arbitrary resistances to be decided upon for each application, R_{POT} is a variable resistance, V_{signal} represents the voltage input from the sensor PVDF, and $V_{control}$ represents the voltage

input from the control PVDF. Values for V_{signal} and $V_{control}$ are determined using Equation (8.4) for voltage follower circuitry.

Two operational amplifiers, the OPA2137P and the AD549KHZ, are implemented in the physical circuit. The AD549 is used for in the voltage follower circuitry; while the OPA2137P is used for the signal differentiation and simple signal scaling. The effects of temperature were performed using a metal heating element and FreeWave software. The signal and control PVDF films are placed in close proximity with the heating element situated in between the two. The circuitry is designed such that both PVDF pieces will have the same value of gain for this test. The heating element is set to four separate temperatures, allowing the PVDF to be heated from 19 to 28 degrees Centigrade, simulating a normal range of ambient temperatures. The purpose of this test is to assess the viability of a differential operational amplifier circuit as a noise compensator, as well as to establish a correlation between temperature and pyroelectric effects.

The results of the temperature test may be found in Figure 8.9. Data is measured for four separate PVDF temperatures: 19.1, 21.0, 22.5, and 28.0 °C. Without PVDF control to serve as compensation, an R^2 value of 0.8192 was found, demonstrated the expected pyroelectric effect. However, with the PVDF control present an R^2 value of 0.0043 was found, showing very little correlation between temperature and output voltage of

the circuitry. The differentiation circuitry can be adopted for temperature drift compensation.

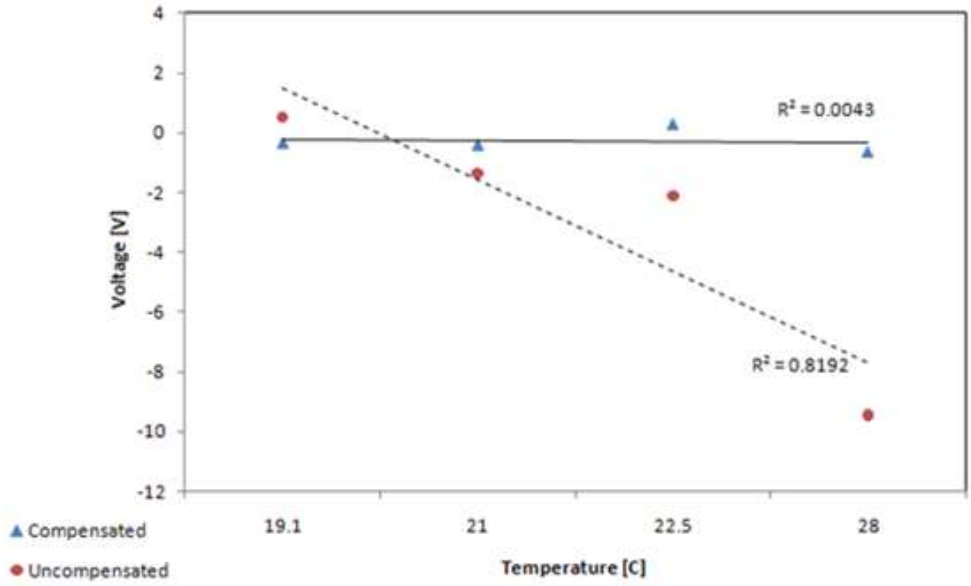

Figure 8.9: Pyroelectric effect in differentiated and non-differentiated circuits

In order to minimize the charge leak-off and account for the lower output voltage, the circuit [59] is passed through the ultralow-input bias current operational amplifier AD549 (Analog Devices, Inc.) with high input impedance Rin= 10^{13} Ω and low-bias current 150 fA. AD 549 as a voltage follower, followed by the low input bias current (5pA), low quiescent current (220μA/ channel), and high open-loop gain (94dB) operational amplifier OPA 2137P (Analog Devices, Inc.) as an operational amplifier with a gain of $1 + \frac{R_2}{R_1}$, as shown in Figure 8.10.

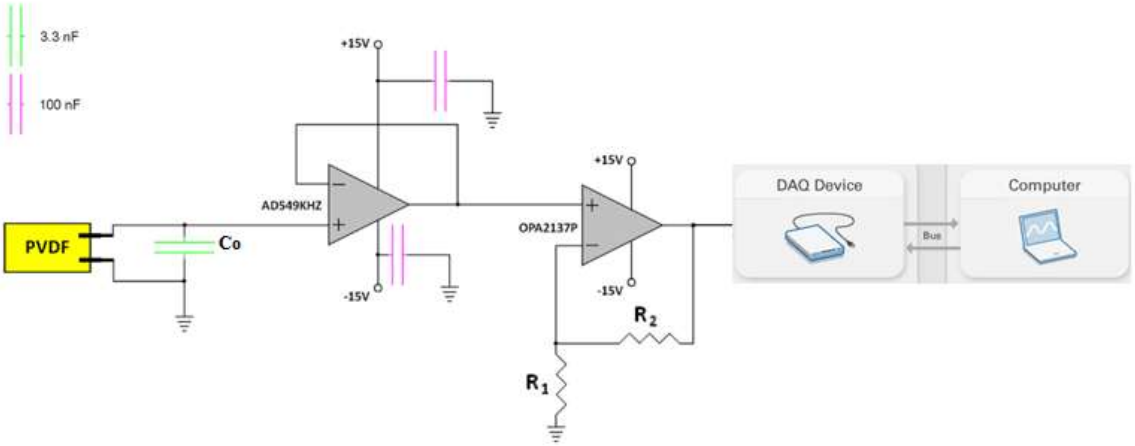

Figure 8.10: Amplification and conditioning circuitry

8.3 Artificial Pressurized Blood Vessels

The pressure in circulation of the blood through the blood vessels is referred to as blood pressure (BP). BP [66] usually refers to the pressure inside the large arteries of the circulation. Blood pressure is expressed by the two terms: systolic pressure (maximum pressure during one cardiac cycle) and diastolic pressure (minimum pressure in between two cardiac cycles). It is measured in (mmHg) millimeters of mercury, above the atmospheric pressure.

Along with heart rate, oxygen saturation, respiratory rate and body temperature; blood pressure is one of the vital signs. For every heartbeat, blood pressure varies between the systolic and diastolic pressure. The blood pressure in the blood circulation is mainly due to the pumping of

the heart. The mean blood pressure differences are primarily responsible for blood flow from one location to another in the circulation. The mean blood flow rate depends both on the blood pressure and the flow resistance presented by the blood vessels. The mean blood pressure [66] decreases as the blood moves away from the heart through the arteries due to viscous losses of energy. Gravity also affects the blood pressure through hydrostatic forces. Breathing and pumping from contracting of skeletal muscles also influence blood pressure. The normal resting blood pressure [66] in a healthy adult is approximately 120 mmHg (16KPa) over 80 mmHg (11KPa), abbreviated as "120/80 mmHg".

The blood arterial pressure is measured commonly with a sphygmomanometer. It uses the height of a column of mercury to measure the circulating blood.

For each heartbeat, the blood pressure varies between the systolic and diastolic pressure. Along with the systolic and diastolic pressure, the entire human body is maintained at 80 mmHg baseline. It behaves as pressurized system. So the pressure varies from 80 mmHg to 120 mmHg for every cardiac cycle.

The experimental setup to mimic the pressurized blood vessels is adopted by using the dual syringe setup as shown below Figure 8.11. Two 100 ml syringes are connected through a three-way valve as shown. The open ends of syringes are covered with latex material vibrating stretchable

membrane. It acts as the vibrating membrane of our design. The syringes are filled with water for our experimental analysis. The three-way valve is also connected to a sphygmomanometer. The two primary purposes of the sphygmomanometer are to directly measure the pressure of the liquid inside the syringes and to set any pressure inside the syringes. In the setup, the initial 80 mmHg of initial pressure is maintained by setting the pressure of the liquid inside the syringes using the sphygmomanometer. This causes the stretching of the latex membrane at the end of the syringes. This forms the initial setup.

The Digital Force Gauge Shimpo FG – 3006 (Shimpo Instruments) is used to apply force on one end of the latex membrane. The corresponding pressure change can be noted on the sphygmomanometer. Preliminary test is done to see the force-pressure relationship between the force applied by FG – 3006 and the pressure that is read on the sphygmomanometer.

Since the systolic/diastolic blood pressure values range around 80/120 mmHg for a normal adult and since the initial pressure inside is maintained at 80 mmHg, the change in pressure that is going to be applied is 0 – 40 mmHg which correspond to 80 – 120 mmHg. This force – pressure relationship and the corresponding voltage that is been developed by the PVDF sensor strips will help us tabulate the values.

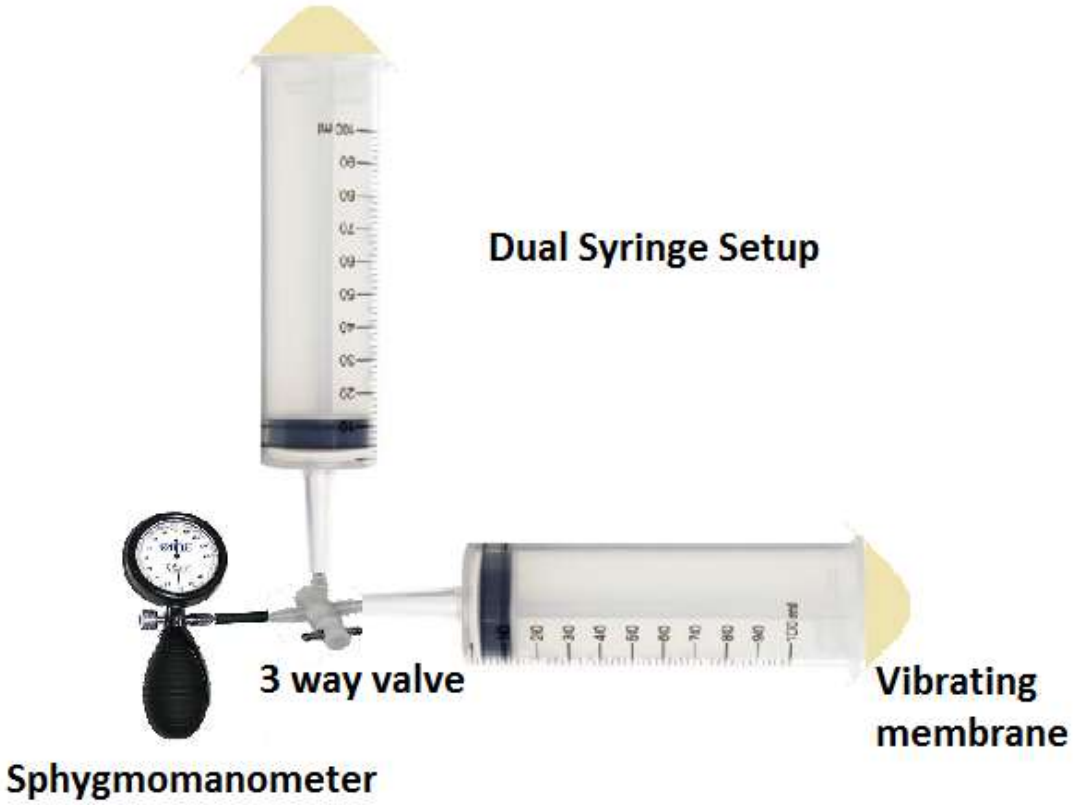

Figure 8.11: Experimental setup to mimic the pressurized blood vessels

8.4 Calibration of the Dual Syringes

Since the input force is applied on one end of the dual syringe and since it gets transmitted through the liquid to the other end of the dual syringe with the vibrating membrane, which is in actual contact with the mechanical structure, some of the energy will be lost within the syringe setup. As the syringe setup is only to depict the blood vessels, and as the actual design of the sensor unit starts from the vibrating membrane that is in contact with the mechanical structure, calibration of the dual syringe

setup to calculate the loss of the force from the place at it is applied to the actual vibrating membrane is required. This calculated reduced force should be the actual force that must be accounted for in the experimental analysis. Calibration of the dual syringe setup is done as shown in figure 8.12.

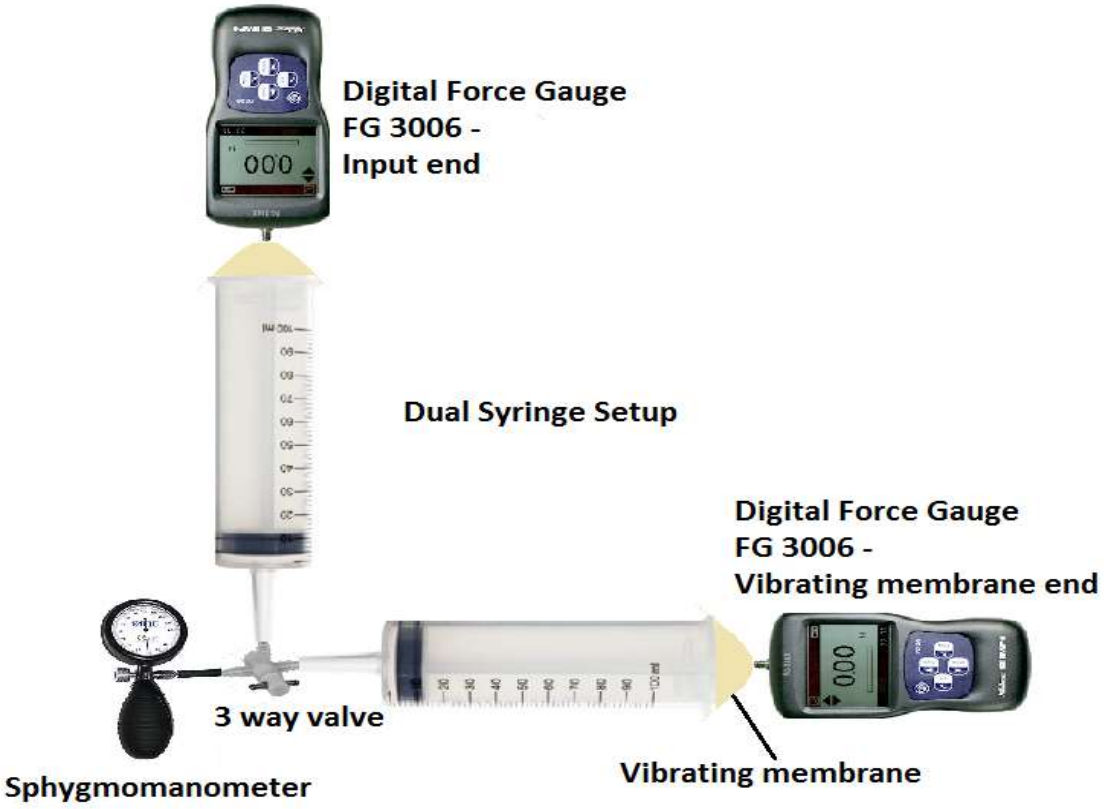

Figure 8.12: Block diagram for calibration of the dual syringe setup

To calculate the force applied on one end of the dual syringe assembly and the force received on the other side of the assembly, two digital force gauges, Shimpo FG-3006 are used, one on either end of the dual syringe assembly, as shown in Figure 8.12.

A manual steadily increasing and decreasing force from 0 to 4 N is applied using one of the force gauges on the input end of the assembly. The force the vibrating membrane on the other end of the assembly receives, is recorded from the other force gauge.

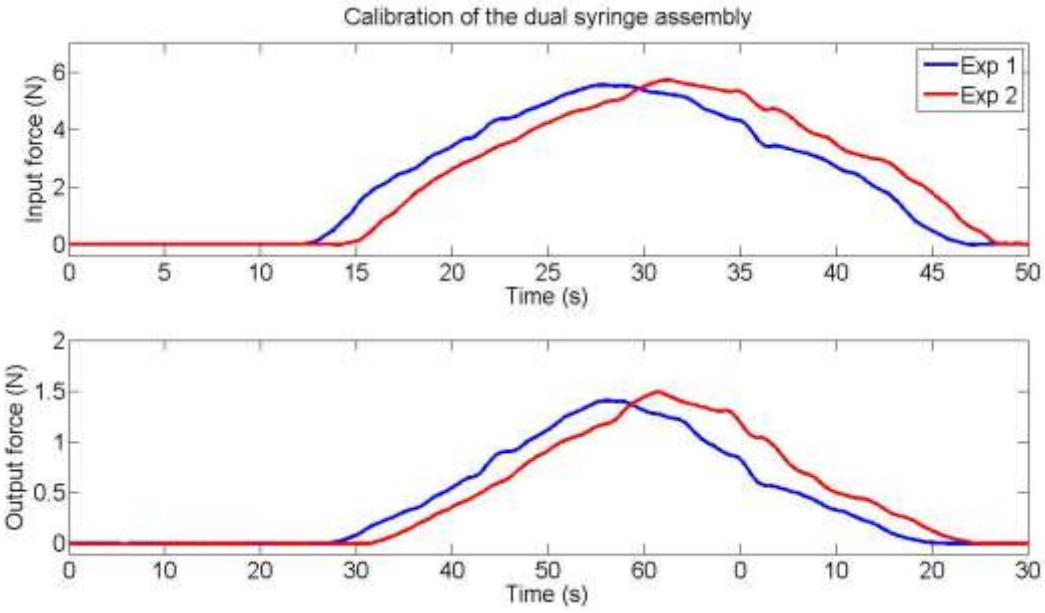

Figure 8.13: Input and output force on the two ends of the dual syringe setup

The force on either side of the dual assembly are plotted in the below figure. A reduction or loss of force by 3.8 times from the input end to the vibrating membrane end is seen, as in Figure 8.13. The best fit transfer function (97.55%) for the input and output end of the dual syringe setup, TF_{sy}, from system identification tool of MATLAB is given by,

$$TF_{sy} = \frac{0.03895s+0.1433}{s^2+0.1131s+0.7788} \tag{8.6}$$

This transfer function is included in experimental analysis. The calibration test is done several times on different days to check the consistency.

8.5 Calibration of the Mechanical Amplification Structure

The calibration test is continued to calibrate the mechanical structure. The force applied on the circular end of the pole and the force that is transmitted along the structure and the force on the tip of the vertical link will also differ doe to loss of energy. Calibration of the mechanical structure is done, as shown in Figure 8.14. To calculate the force applied on circular end of the pole and the force received on the tip of the vertical link, two digital force gauges, Shimpo FG-3006 are used, one on either end of the mechanical structure assembly, as shown. A manual steadily increasing and decreasing force from 0 to 5 N is applied using one of the force gauges on the circular end of the pole. The force the tip of the vertical link on the other end of the assembly receives, is recorded from the other force gauge. The force on either side of the mechanical structure assembly are plotted in the below Figure 8.15. A reduction or loss of force by 3.5 times from the circular end of the pole to the vibrating mem tip of the vertical link end is seen, which correlates with the design of the lever mechanism of reduced force and increased deflection. The

calibration test is done several times on different days to check the consistency.

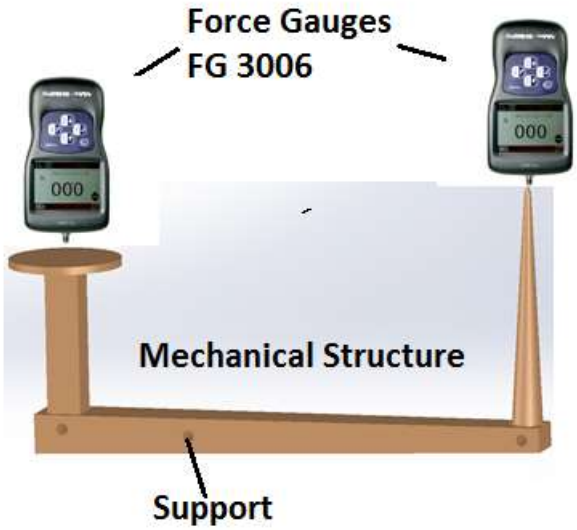

Figure 8.14: Block diagram for calibration of the mechanical structure

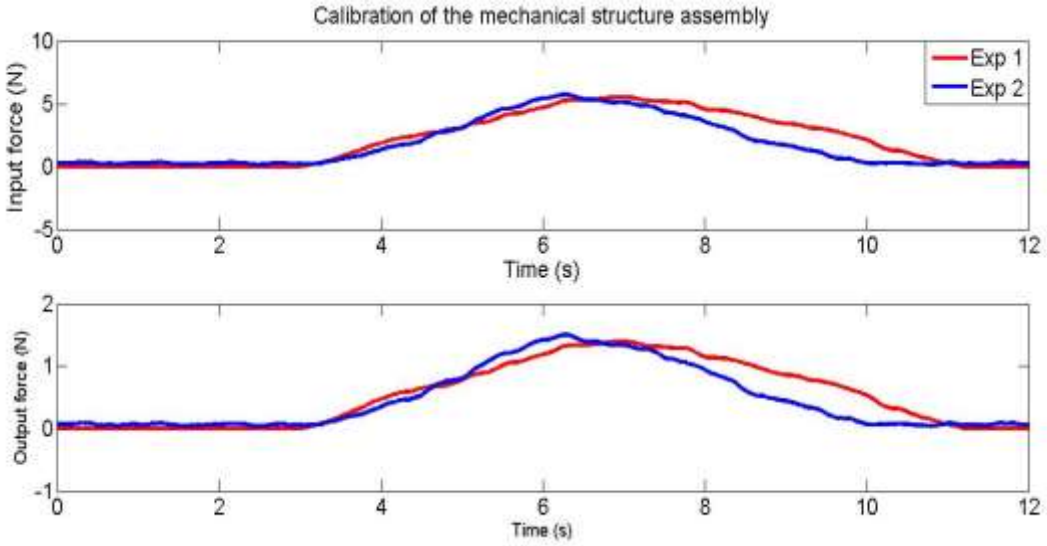

Figure 8.15: Input and output force on either side of the mechanical structure

8.6 Simulation, Experiment and Analysis

Simulation is done for both with and without the mechanical structure for comparison. The simulation setup on ANSYS 16.2 for both the designs are shown in Figures 8.16 and 8.17.

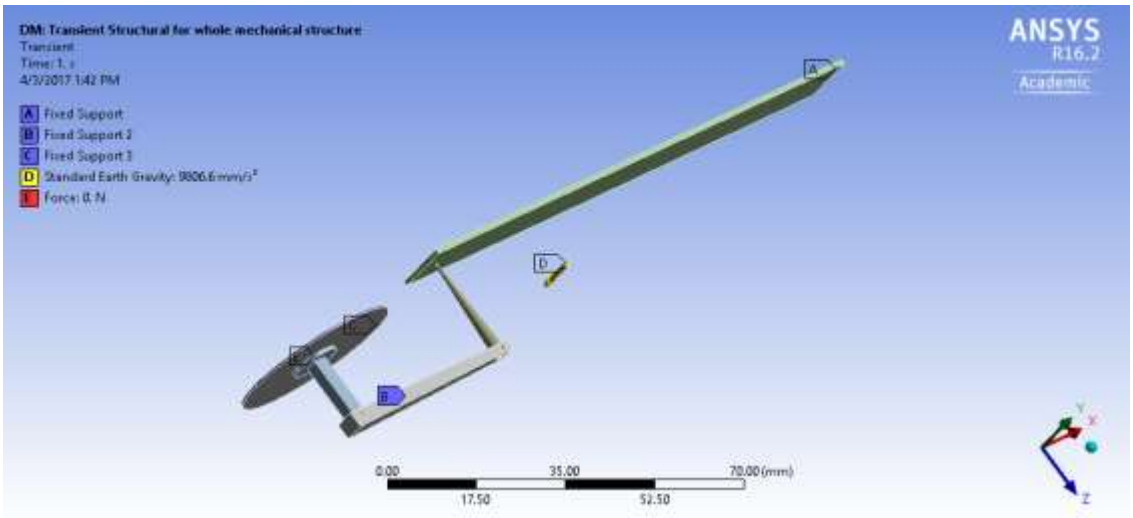

Figure 8.16: Simulation setup for with the mechanical structure design

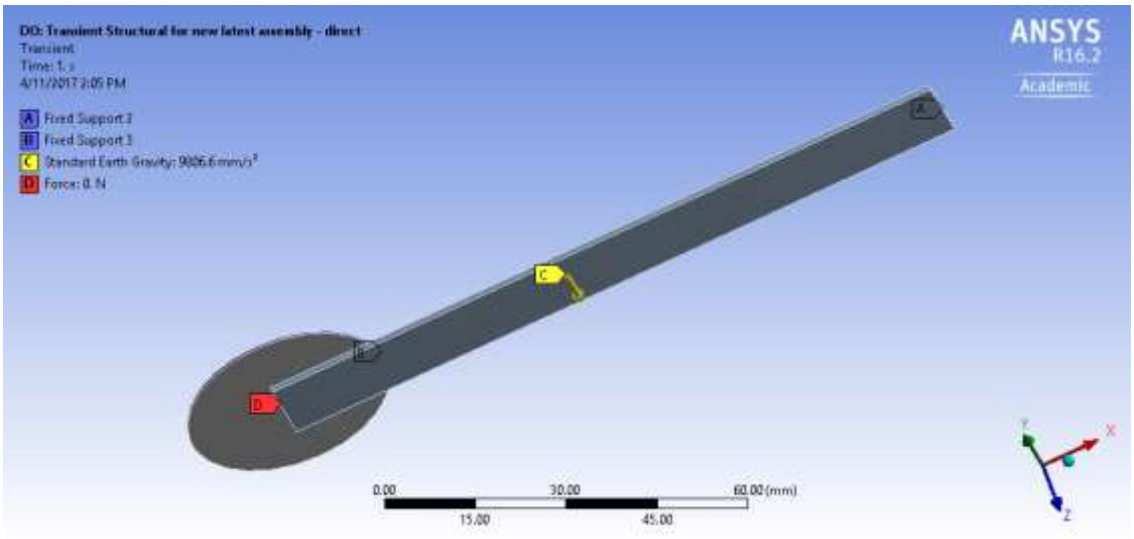

Figure 8.17: Simulation setup for without the mechanical structure design

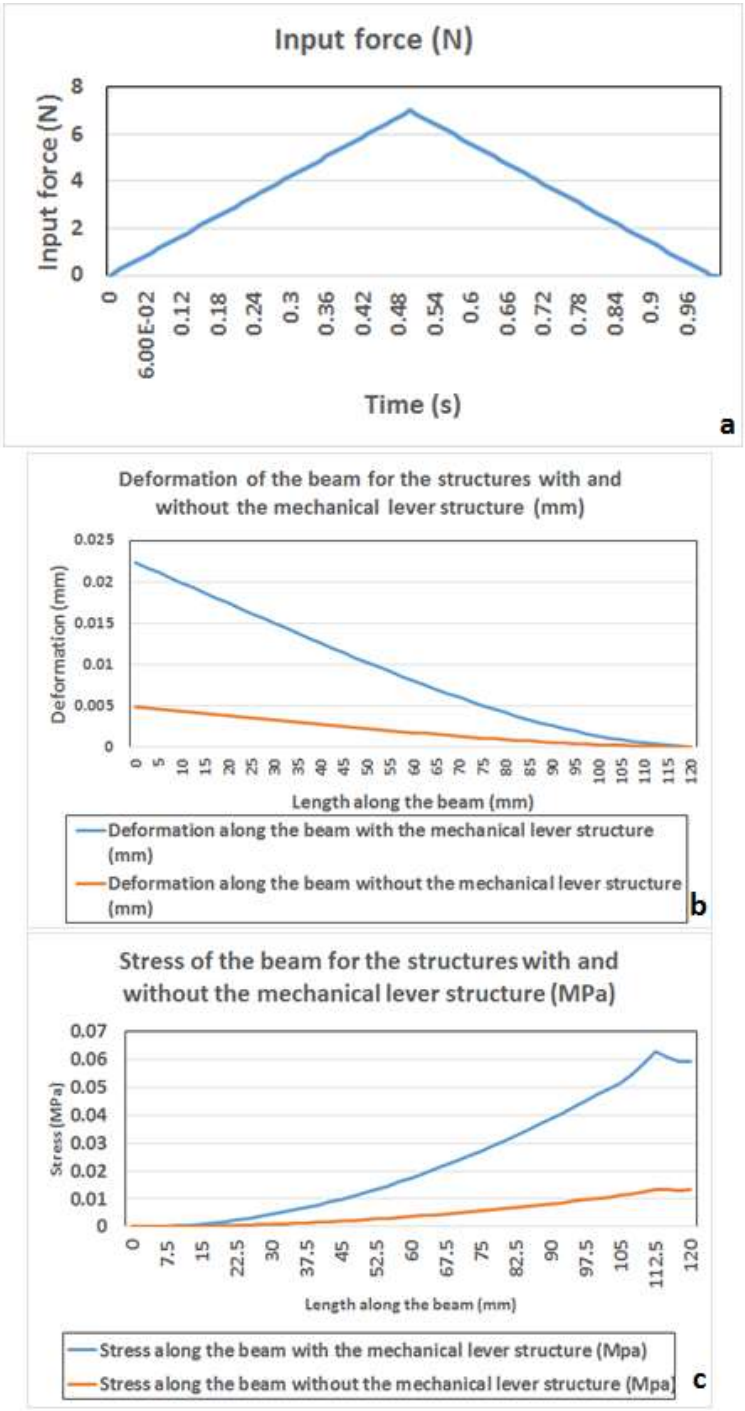

Figure 8.18: a: Input Force applied, b: Deformation for both designs, c: Stress for both designs

An input force from 0 to 7N and then back to 0N is applied on the center of the vibrating membrane. The corresponding deformation and stress developed along the length of the beam for both the structures are shown in Figure 8.18. An increased deformation and stress is seen on the structure with the mechanical amplification structure. The amplification factor obrtained in simulation is around 6. Experiments are done for both with and without the mechanical structure for comparison. The block diagrams for the testing setups for with and without the mechanical amplification structures are shown in the below Figures 8.19 and 8.20 respectively.

The first test is done to study the system characteristics in free vibration. The beam is subjected to a force, which causes the beam to bend. The force is released from the beam and the free vibration is noted for both the design structures for comparison. This is to study the damping factor for the structure and to study how fast the system comes to stead state after oscillations.

The free vibration is plotted for the model transfer function equation derived in equations (8.1 and 8.2) as below in Figure 8.21.

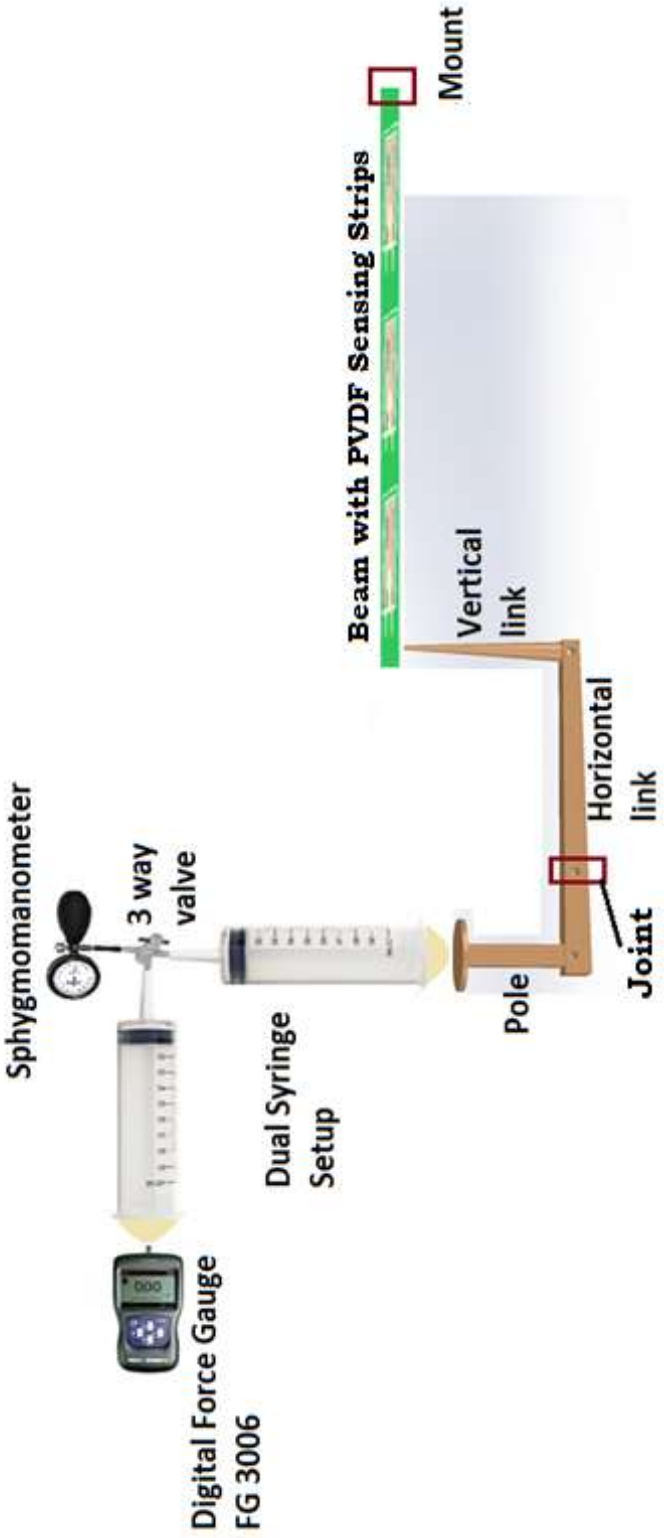

Figure 8.19: Block diagram showing the setup with the mechanical amplification structure design

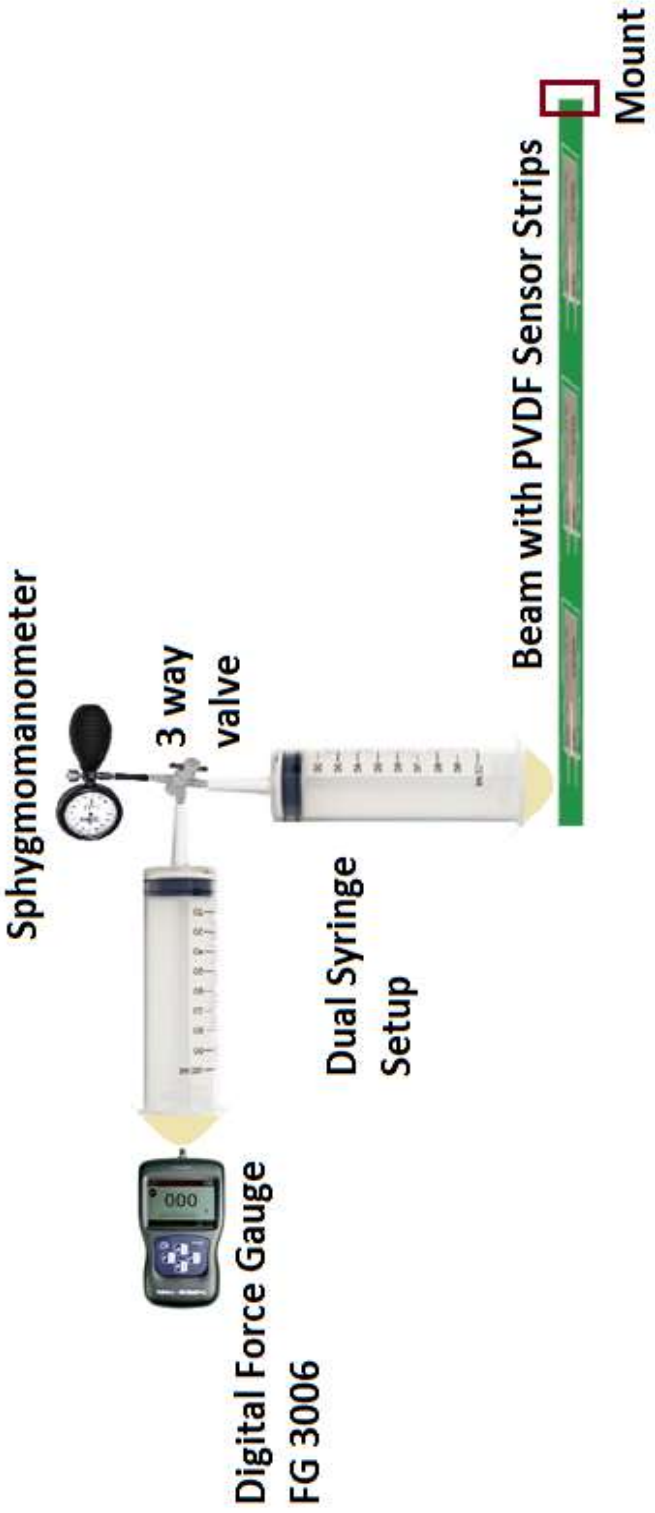

Figure 8.20: Block diagram showing the setup without the mechanical amplification structure design

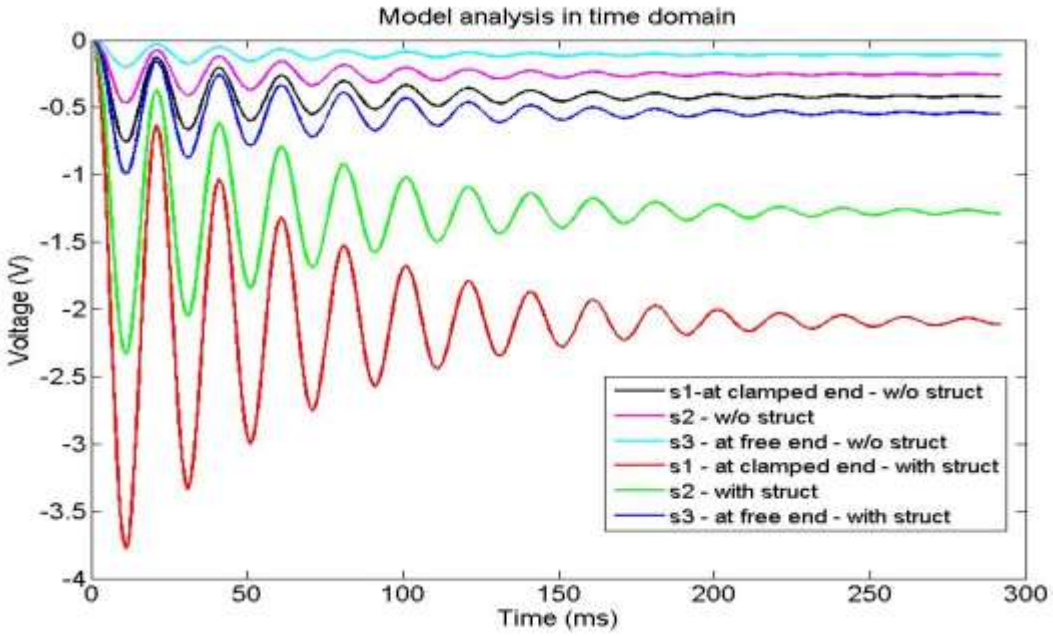

Figure 8.21: Free vibration analysis of model transfer function for both designs

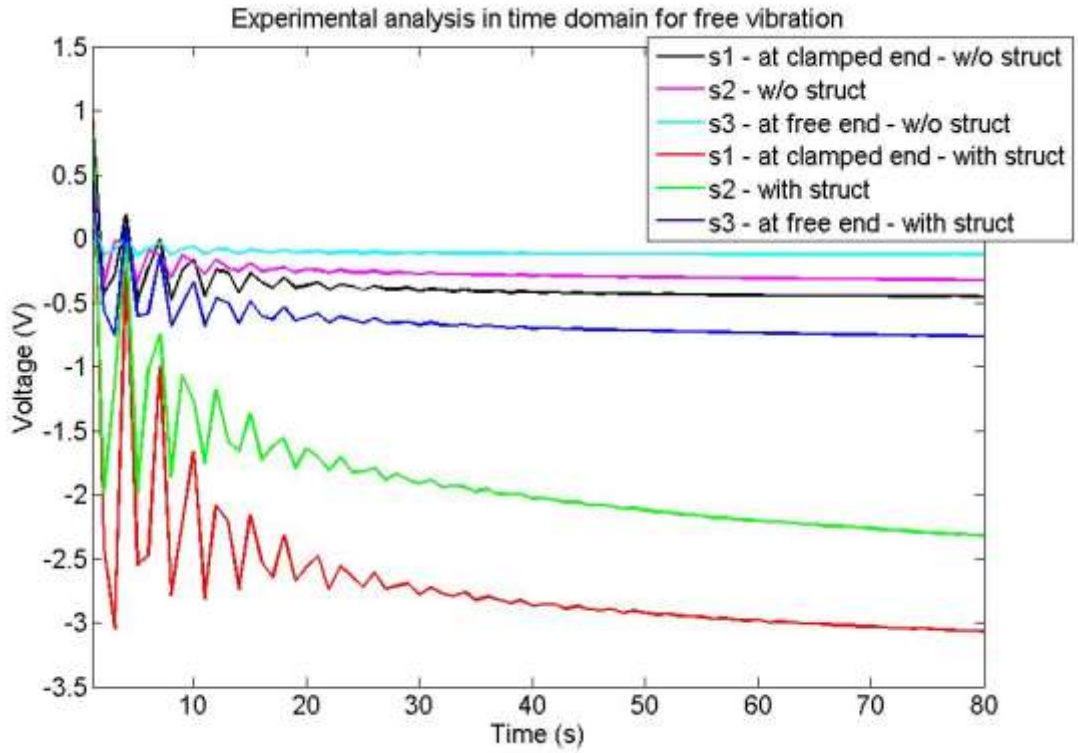

Figure 8.22: Free vibration experiment for both designs

The free vibration analyses are also done for our experimental design setup and the results are plotted in the below Figure 8.22, in time domain. The damping factor calculated from the free vibration is 0.05 and it is also used for our modelling. It is seen that the without the mechanical structure design, comes to steady state faster than the with the mechanical structure design. The mechanical structure contributes more to the oscillation, as the mechanical structure system involves the pole-horizontal link-vertical link mechanical structure along with the beam while the direct system involves just the beam.

However, the mechanical structure system provides amplified signal both in the modelling and in the experimental results. The output voltage from the system with the mechanical structure is around 6 times greater than the output voltage from the system without the mechanical structure (direct). This satisfies the bio-mimicked middle ear amplification design of the pressure sensor design.

Preliminary force-pressure comparison work is done before the actual experiment to see the relationship between the force applied on FG 3006 and the corresponding pressure readings on the Sphygmomanometer used in the setup.

An initial 80 mmHg pressure is setup inside the fluids in the dual syringe setup for initial conditions. Since the normal blood pressure range of a

normal adult ranges from 80 – 120 mmHg which correspond to 0 – 40 mmHg of pressure change in our experimental setup, force-pressure relationship for 0 – 40 mmHg of pressure change (a 40 mmHg rise in pressure level from the initial 80 mmHg pressure level) is monitored and recorded. The below Table 8.1 shows the recorded values.

Pressure value in the Sphygmomanometer (mmHg)	**Corresponding Force value in the digital Force Gauge FG 3006 (N) (approximately)**
80	0
90	1
100	2
110	3
120	4

Table 8.1: Table showing the pressure to force relationship for the experimental setup

The analysis is further continued by applying force on the input end of the dual syringe using the digital force gauge Shimpo FG 3006 (Shimpo Instruments). The force applied here is a manual one for more random and real-time input. A manual steadily increasing and steadily decreasing force from 0 to 5 N and 5 to 0 N is applied on the input end. The corresponding output voltage generated from all three PVDF sensor strips for the design

with the mechanical structure and without the mechanical structure is plotted in the below Figures 8.23 and 8.24 respectively, in time domain. Also, the input force for both the structures are the calibrated input values. The input force data is multiplied with the calibrated transfer function from sessions 8.4.

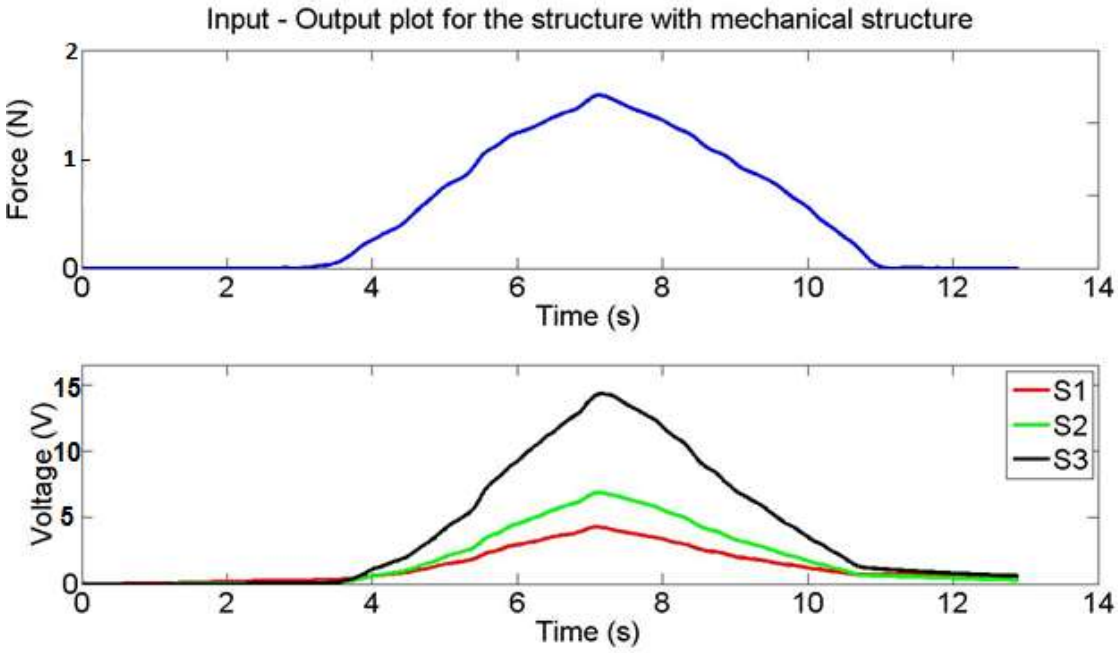

Figure 8.23: Input force – output voltage from 3 sensors with the mechanical structure design with S1 in free end and S3 in clamped end

Each plot shows the output from all three sensor strips with sensor towards the clamped end, S3, generating the highest output. Along with that, the design with the mechanical structure has generated an amplified output voltage of approximately 3.8 times in comparison to the design without the mechanical structure. This is less than the modelled amplified value of 6 times. The loss could be due to loss of energy due to

environmental factors, noise and more. The test is conducted several times on different to test the consistency in data and it correlates

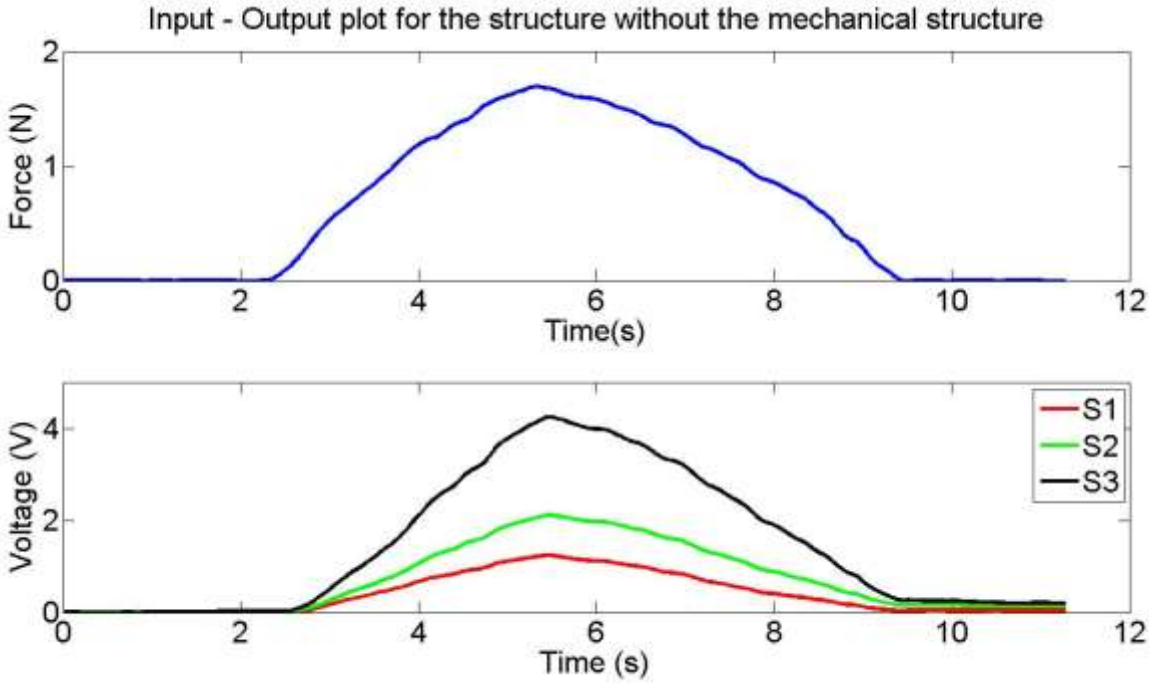

Figure 8.24: Input force – output voltage from 3 sensors without the mechanical structure design with S1 in free end and S3 in clamped

The frequency domain plots for the above experimental data and the model is shown in the below Figure 8.25. The bode plot shows five modes for the design with the structure and design without the structure for the model. The frequency curve "model – w/o struct" and "model – with struct" correspond to the frequency plots of the model transfer function for the without the mechanical structure design and with the mechanical structure design. The plot also shows two sets of experimental data for both the designs. The frequency curve "exp1 – with struct" and "exp2 – with struct" correspond to two experimental analyses on the design with

mechanical structure. Similarly, the frequency curve “exp1 – w/o struct” and “exp2 – w/o struct” correspond to two experimental analyses on the design without mechanical structure.

The first mode on the model occurs at 91.4956 rad/s and the first modes for the experimental data is also around 89 rad/s, which is closer to the model value. Also, the magnitude part of the experimental data although lower than the model values, which could be due to environmental losses and noise, still follow a variation pattern between the with the mechanical structure and without the mechanical structure design.

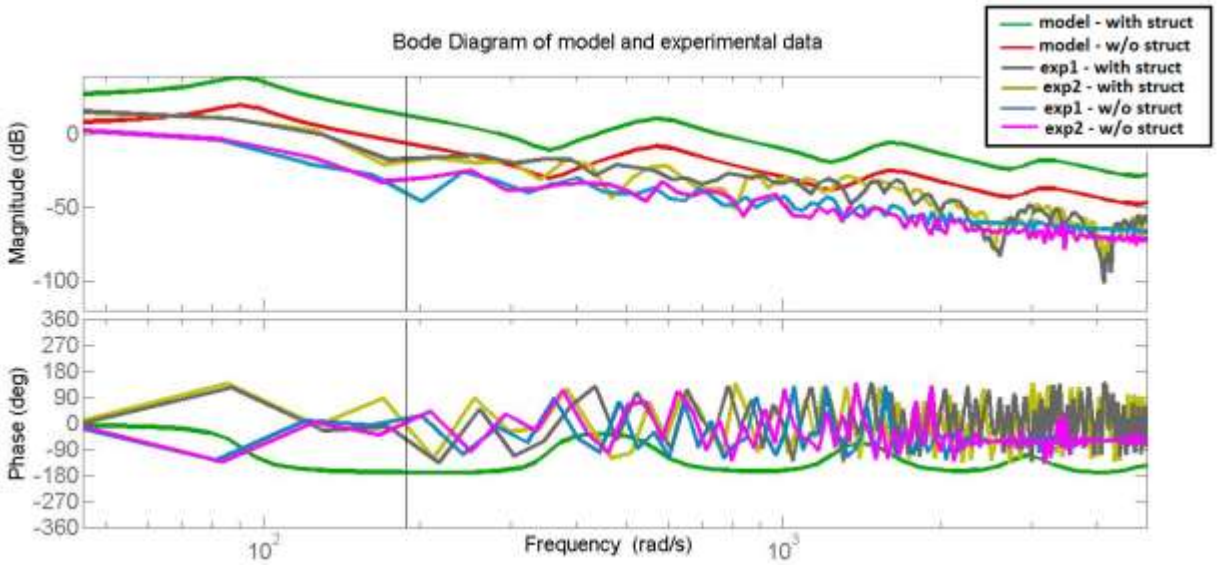

Figure 8.25: Frequency domain analysis of the transfer function and experimental data for both designs

8.7 DSA Experiments and Discussion

DSA, often referred to Dynamic Signal Analysis or Dynamic Signal Analyzer depending on the context, is an application area of digital signal

processing technology [67]. Compared to general data acquisition and time domain analysis, DSA instruments [67] and math tools focus more on the dynamic aspect of the signals such as frequency response, dynamic range, total harmonic distortion, phase match, amplitude flatness etc. In recent years, time domain data acquisition devices and DSA instruments have gradually converged together. With advancements, time domain systems can involve frequency analysis and dynamic signal analyzers can do time domain analysis. DSA [67] uses various technology of digital signal processing. Among them, the most fundamental and popular technology is based on the so called the Fast Fourier Transform (FFT).

The Dynamic Signal Analyzer, SR 785 from Stanford Dynamic Systems is used in our analysis to analyze the dynamics of the system. SR 785 is a two-channel, high precision dynamic analyzer which can be operated in six measurement groups. The two measurement groups that are used in our work are FFT and correlation. In FFT group, the input data is taken in time domain and then transformed into frequency spectra. In Correlation group, these spectra are transformed back into the time domain to yield auto and cross correlations.

To test the dynamics of both the designs and check the superiority of the with the mechanical structure design, an input of approximately -1 to +1 V, 2 Hz square signal, is applied with a vibration shaker, which is an electro-dynamic vibration generator from Ling Dynamic Systems, through

the DSA SR 785. The block diagrams for the testing setups for with and without the mechanical amplification structures with DSA are shown in the below Figures 8.26 and 8.27 respectively. The input-output data from the DSA for both the designs are plotted in the below Figures 8.28 and 8.29 respectively. The output signal generated by both the designs on the DSA, shows approximately 1.1V peak-to-peak from the without the mechanical structure design and approximately 3.5V peak-to-peak from the with the mechanical structure design, respectively.

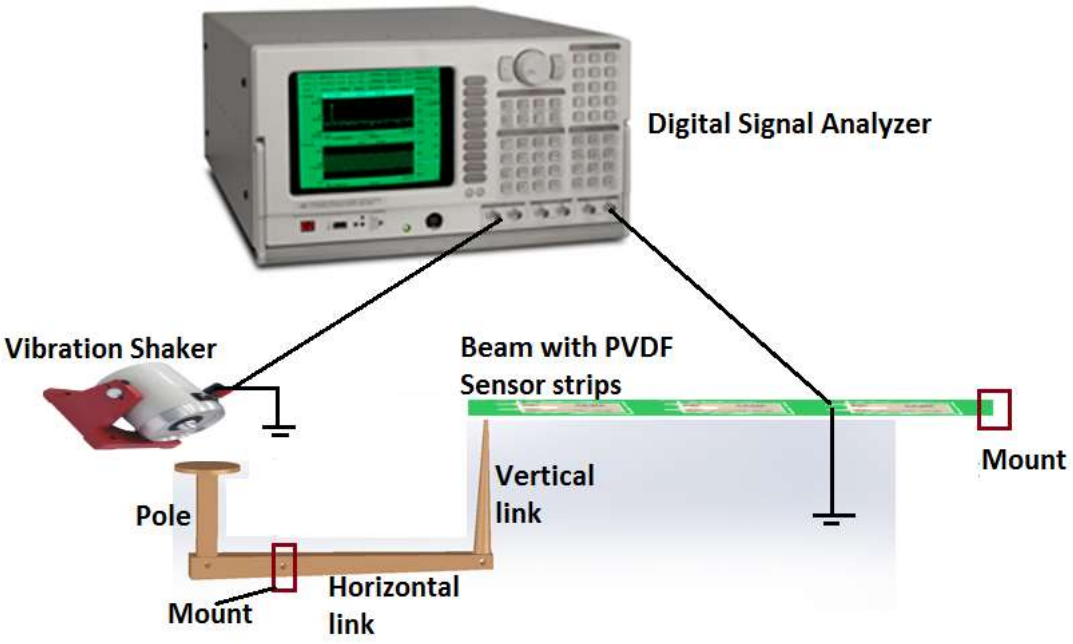

Figure 8.26: Illustration of the experimental setup with the mechanical amplification structure

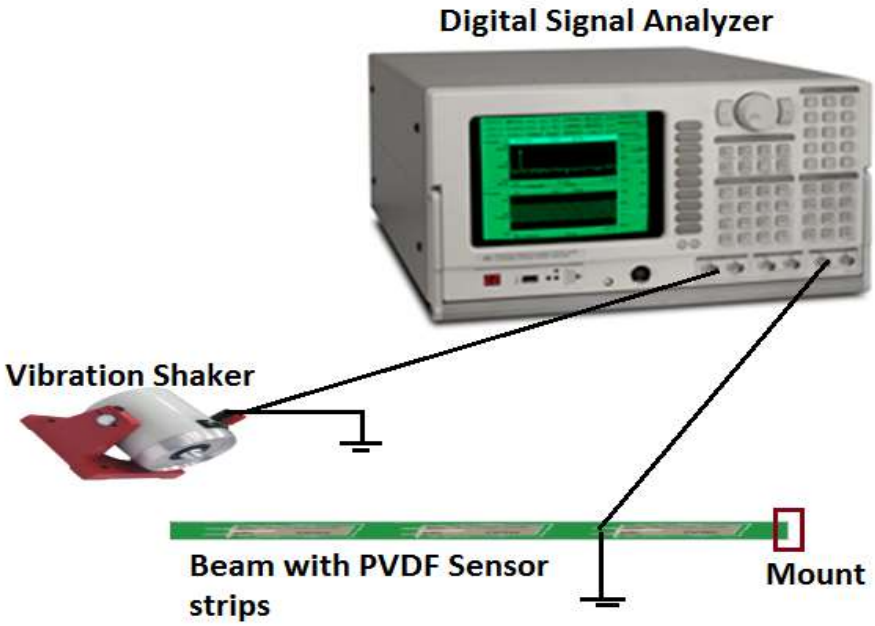

Figure 8.27: Illustration of the experimental setup without the mechanical amplification structure

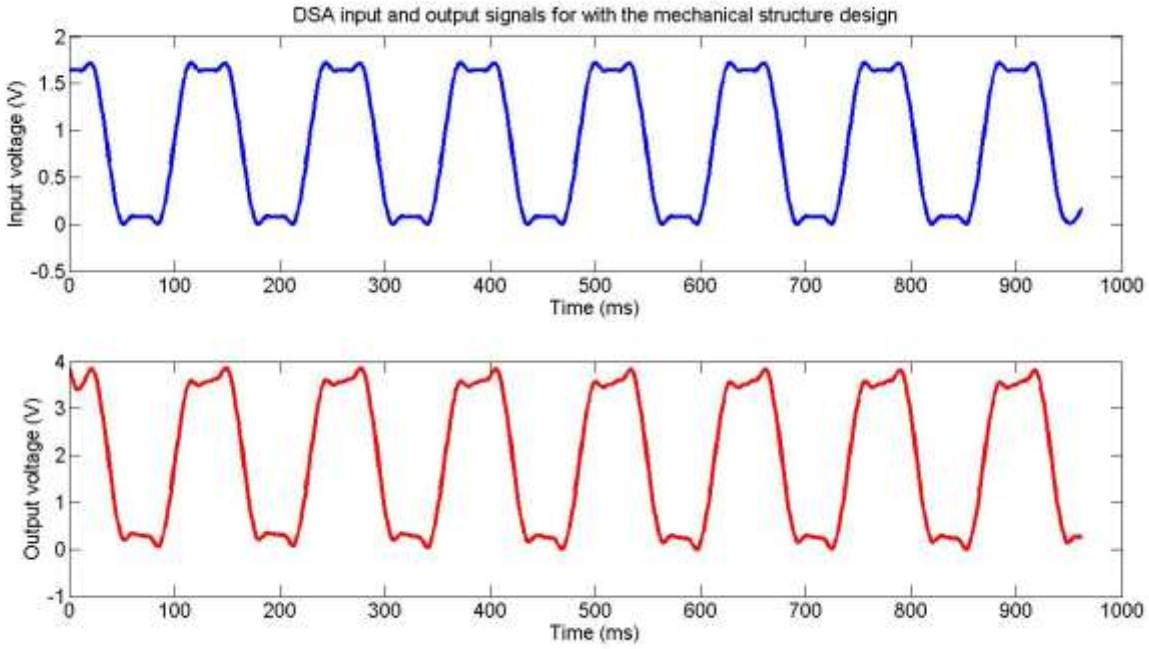

Figure 8.28: The input from the shaker-output from sensing beam for the setup with the mechanical amplification structure

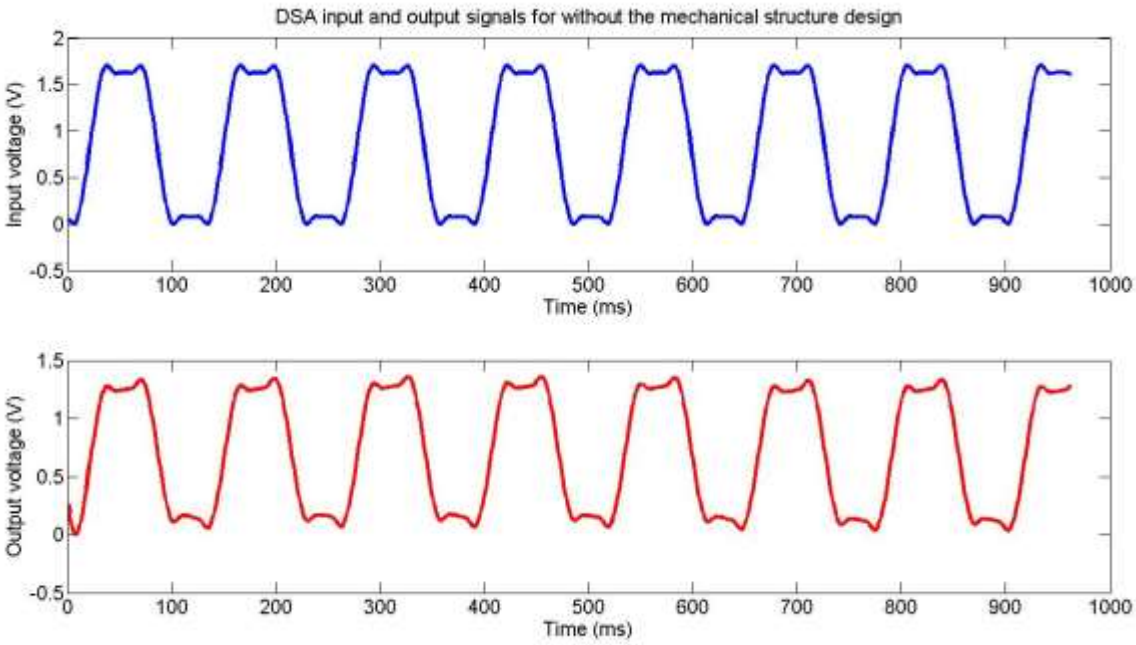

Figure 8.29: The input from the shaker-output from the sensing beam for the setup without the mechanical amplification structure

This corresponds to approximately 3 times amplification by with the mechanical structure design, which is close to the experimental data from Section 8.7. A chirp [68] is a signal in which the frequency increases (up-chirp) and decreases (down-chirp) with time. A chirp input is applied to both the design structures and the DSA outputs are obtained. The input – output chirp plots for both the designs are plotted below in Figures 8.30 and 8.31 respectively. Both the designs follow the chirp pattern with, with the mechanical structure design output having an amplified signal with respect to the without the mechanical structure design.

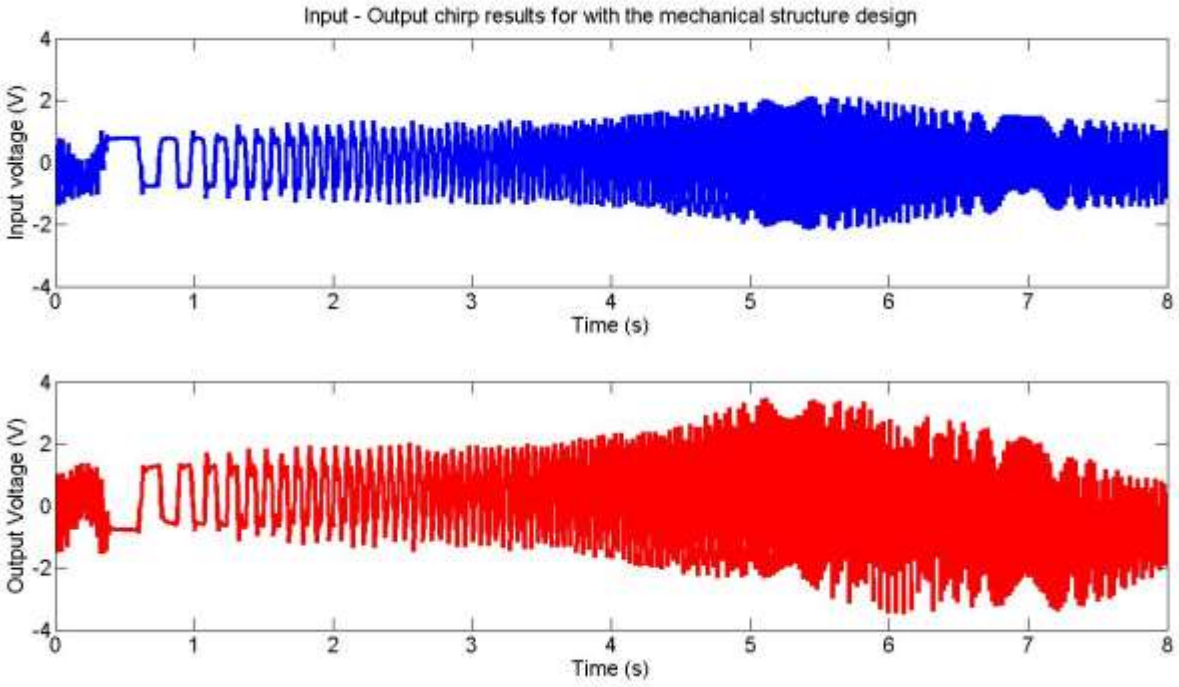

Figure 8.30: The input – output chirp plots for the setup with the mechanical amplification structure

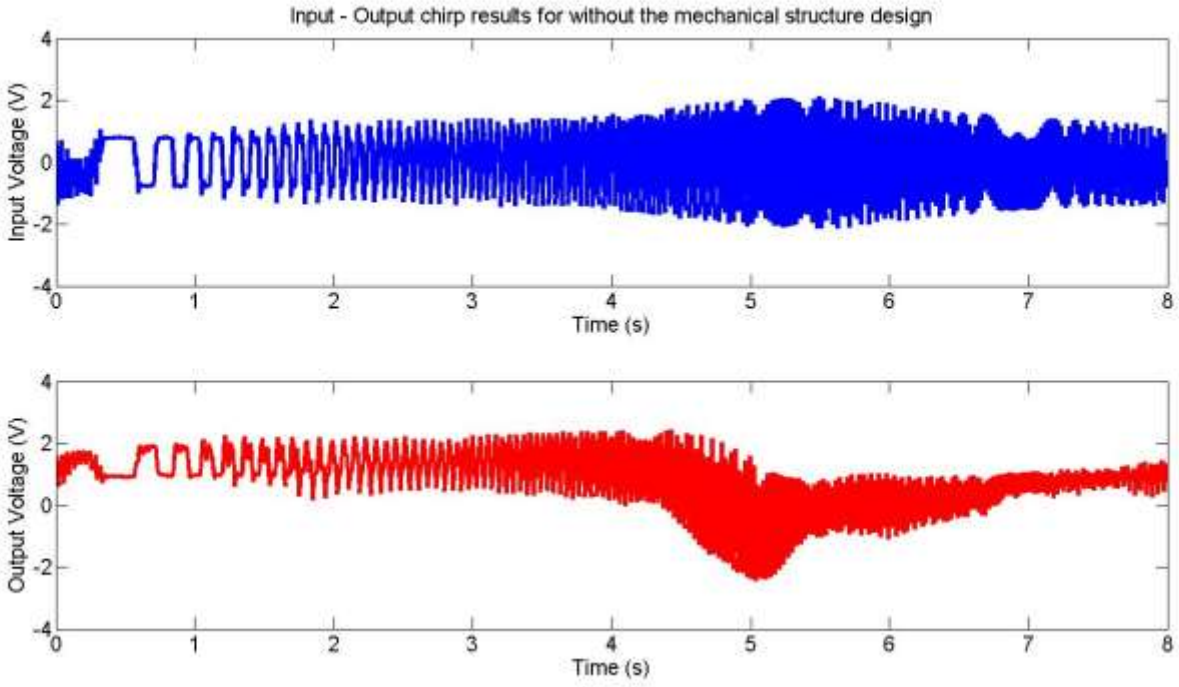

Figure 8.31: The input – output chirp plots for the setup without the mechanical amplification structure

The corresponding bode plots are plotted in the below figure 8.32. Along with the DSA frequency domain plots, are plotted the frequency domain plots of the model, for comparison.

The first mode on the model occurs at 91.4956 rad/s and the first modes for the experimental data is also around 80 rad/s, which is closer to the model value. Also, the magnitude part of the experimental data although lower than the model values, which could be due to environmental losses and noise, still follow a variation pattern between the with the mechanical structure and without the mechanical structure design.

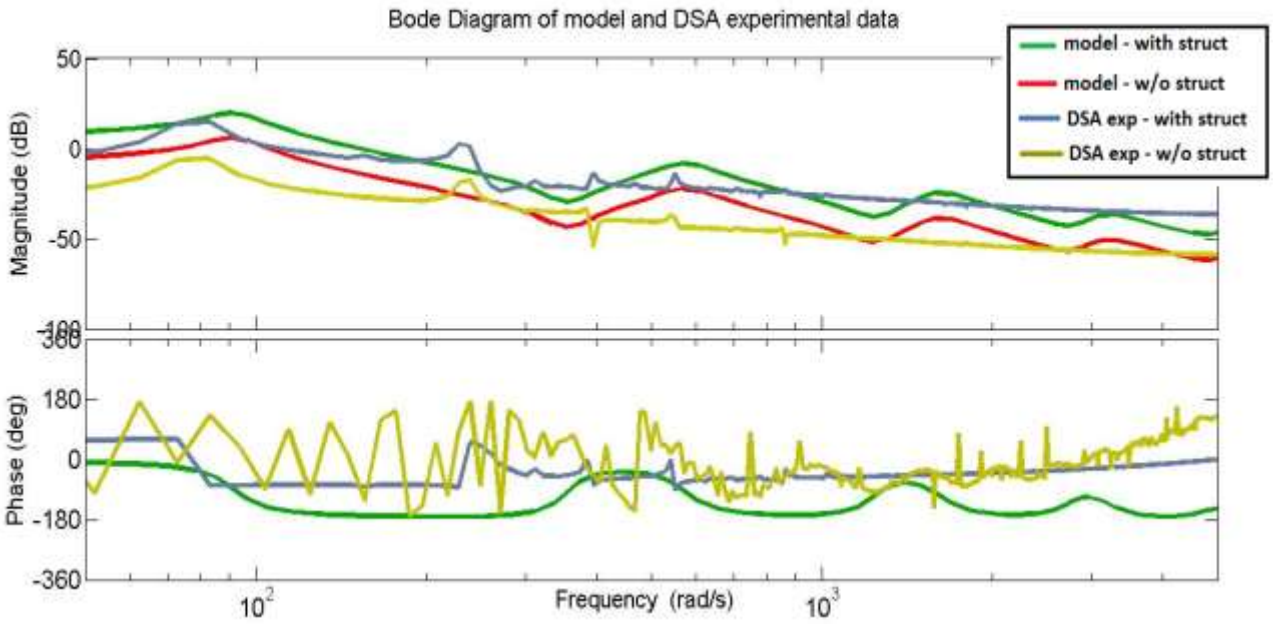

Figure 8.32: Frequency domain plot for model transfer function and DSA results for both designs

8.8 Model Validation Results

To validate the accuracy of the derived model transfer functions in equations (8.1) and (8.2) for without the mechanical structure design and with the mechanical structure design respectively, DSA input data from session 8.7 is used as input into the below model transfer function equations and the respective outputs obtained from the transfer functions are plotted below.

$$V_{ko}(s) = \frac{1}{1+sRC_k} * \left(1+\frac{R_2}{R_1}\right) * \frac{C_{sk}\sum_{ki=1}^{\infty}\sum_{i=1}^{\infty}\varphi_i(L)\,[\ \varphi_i'(s_{k2}) - \ \varphi_i'(s_{k1})]}{\left[[s^2+2\zeta_{ki}\omega_{ki}s+\omega_{ki}^2]\right]} * F(s)$$

where $C_{sk} = \frac{c_{4k}Y_4\left(1-\gamma\frac{d_{32}}{d_{31}}\right)}{C_k}$ (8.8)

$$V_{ko}(s) = MA * \frac{1}{1+sRC_k} * \left(1+\frac{R_2}{R_1}\right) * \frac{C_{sk}\sum_{ki=1}^{\infty}\sum_{i=1}^{\infty}\varphi_i(L)\,[\ \varphi_i'(s_{k2}) - \ \varphi_i'(s_{k1})]}{\left[[s^2+2\zeta_{ki}\omega_{ki}s+\omega_{ki}^2]\right]} * F(s)$$

where $C_{sk} = \frac{c_{4k}Y_4\left(1-\gamma\frac{d_{32}}{d_{31}}\right)}{C_k}$ and

$$\text{MA} = \left[\left(\frac{SA\ of\ pole}{SA\ of\ vertical\ link\ tip}\right) + \left(\frac{Distance\ from\ mount\ to\ right\ end\ of\ horizontal\ link}{Distance\ from\ left\ end\ of\ horizontal\ link\ to\ mount}\right)\right] \quad (8.9)$$

For comparison, the input DSA data, the output from the DSA and the output from the model transfer function are plotted in one plot. This analysis is done for the design with the mechanical structure and for the

design without the mechanical structure, in Figures 8.33 and 8.34 respectively.

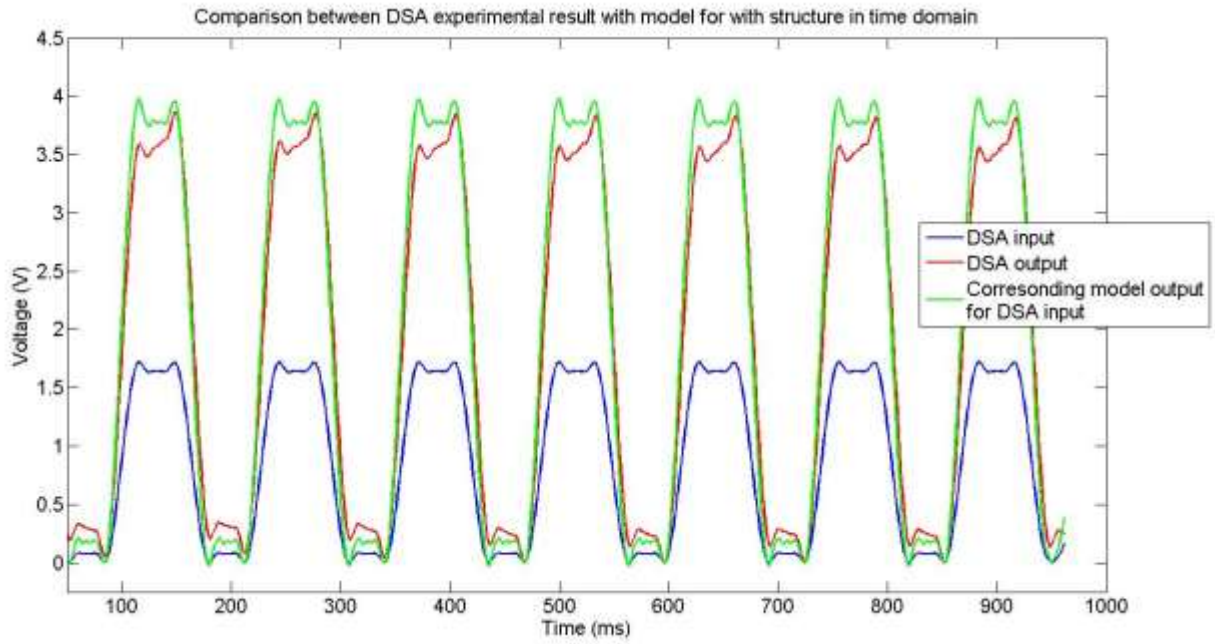

Figure 8.33: Input and output from DSA and the model transfer function for the setup with the mechanical amplification structure

It is seen that output from the model transfer function closely match the DSA output result, for both the designs, thereby validating the accuracy of the transfer function. The test is conducted couple more times, to test the consistency and results match.

In the above plots, the DSA input square wave of approximately 1.6V peak-to-peak was applied as input to the model transfer function. The DSA output for with the mechanical structure design, is 4V peak-to-peak and the corresponding transfer function output is approximately 3.75V.

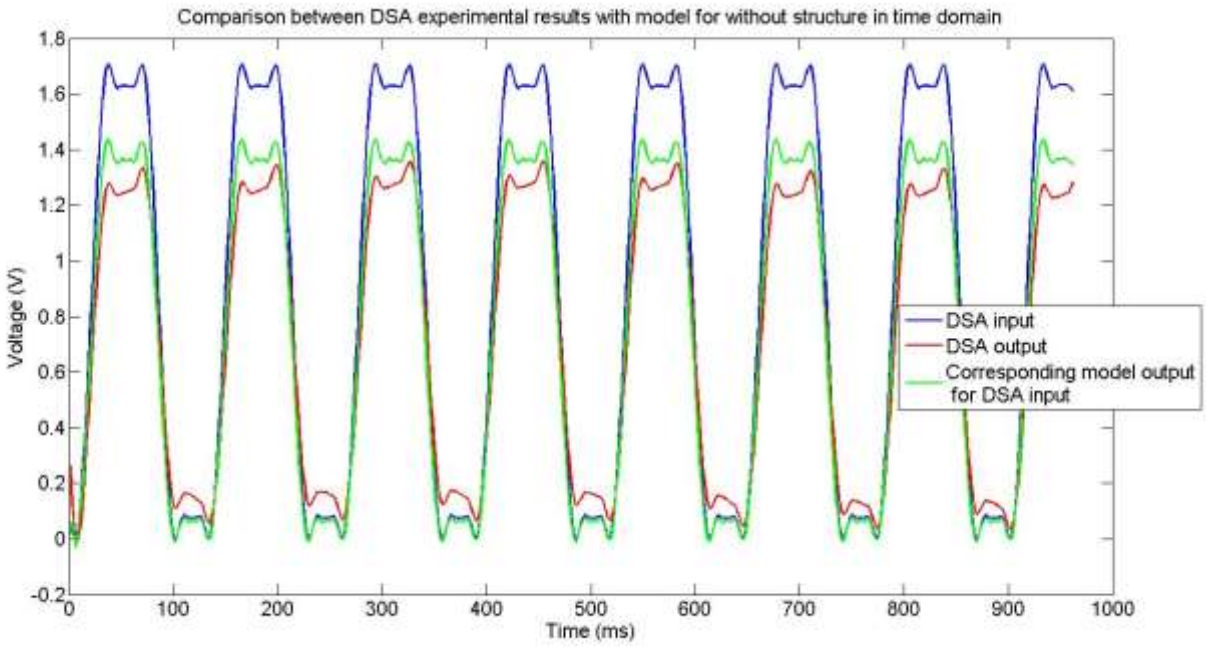

Figure 8.34: Input and output from DSA and the model transfer function for the setup without the mechanical amplification structure

Similarly, the DSA output for without the mechanical structure design is 1.4V peak-to-peak and the corresponding transfer function output is approximately 1.3V peak-to-peak.

To conclude, 80 – 120 mmHg is the normal blood pressure range seen in the parent blood vessel arteries and a minimal or no pressure change should be seen inside the aneurysm after the flow-diverting stent placement. So, any corresponding voltage to a corresponding significant pressure change will lead to contradicting the flow-diverting stent theory.

Chapter 9

Future Work and Conclusion

9.1 Wireless Transmission

In the real world, most data are characterized by analog signals. To wirelessly transfer and manipulate the data using a microprocessor [69], we need to convert the analog signals to the digital signals, using analog-to-digital converters, so that the microprocessor will be able to read, understand and manipulate the data. The digitalized data is then stored in the memory. The data is wirelessly transferred via RF transmitter after modulating (outside the scope of the project). The data can be transferred by using the 3D ESAs patterned on top of the micro-mount in a similar fashion as done by Adams et al, Duoss et al and their colleagues [69]. In this work, conformal printing of silver nanoparticle inks on curvilinear surfaces to create electrically meander lines, is demonstrated.

The RF receiver outside receives the data and using signal conditioning electronics, the digitalized data can be converted back to the analog signal using digital-to-analog converters and interpolation and by using the

above model equations the force (pressure) values corresponding to the output voltage values can be calculated.

9.2 Conclusion

The bio-inspired pressure sensor utilizes the ear hearing mechanics. It benefits by consisting of:

(1) the circular vibrating membrane which vibrates based on the intraaneursymal pressure changes. This mimic the tympanic membrane part of the ear,

(2) the other side of the vibrating membrane is connected to three pole-links structures similar to the three bones of the middle ear to perform the middle ear's leverage mechanism,

(3) the composite cantilever beam structure with the sensor strips mimics the coiled cochlea of the inner ear, in elongated form. The piezoelectric sensing strips are responsible for the passive mechanoelectrical conversion and generation of electric voltage, for the intraaneursymal pressure change application.

As mentioned in research background, with the post procedural complication rate being around 3% leading to delayed bleeding and the reason behind this rupture being still unclear; the developed self-power, highly sensitive pressure in this work, can be built in micro scale with wireless feature (outside scope) and upon approval and tested, can monitor

the pressure changes inside the aneurysm. It should provide a different and clear understanding to the surgeons on what could be going on inside the aneurysm. Based on this clarity and the results from the sensor, the decision on treatment options made by the surgeons may or may not change. Based on the pressure recordings from the sensor inside the aneurysm, after the stent placement, the future research on this sensor and measurement tasks can be in two directions:

- If the pressure changes after the deployment of the stent, it can turn the research focus into development of better stents which may not increase the pressure.
- If there is no change in pressure, then the theory that delayed aneurismal rupture due to pressure changes can be ruled out and can further lead to search for other causes of delayed aneurysmal rupture.

Appendix

The following programs complements the modelling of the pressure sensor design discussed and derived in Chapter 6. The below program derives the transfer function for with the mechanical structure design by incorporating the piezoelectric equations along with equation of motion of the beam. It also incorporates the amplifications factor of the ear mechanism, along with voltage follower and amplifications characteristics of the circuit. It also compares itself with the transfer function of the design without the mechanical structure. The program also plots the transfer function of both the designs on free vibration for both designs in time and frequency domain. It also plots the time and frequency domain analyses of experimental data and validates it with DSA data.

```
% Matlab Code
% Deriving the transfer function for the modelled design - with
% the mechanical structure design and comparing it with the without
% the mechanical structure design

% Nithya P Mohan
%============================================================
 clc;
clear all;
close all;
%============================================================
damp=[0.05];
% young's modulus pvdf
E=3*10^9;
% Dimensions of the beam in metres
L=.12; B=.013; Th=0.001;
% Moment of Inertia
I=(1/12)*B*(Th^3);
% Material density of PVDF in kg/m^3
Ro=1.78*10^3;
m=B.*Th.*Ro;
%possion ratio
PR=0.34;
C=3.3e-9;
```

```
Cpvdf=(880e-12);

Cin=(1000e-12);

Rin=1e13;

R1=1e3;

R2=10e3;

SA1=0.036649; %surface area of pole

SA2=0.013434; %surface area of vertical link tip

d1=3; %distance from mount to right end

d2=1; %distance from mount to left end
c4=0.006;

d31=23e-12;

d32=2.7e-12;

nmodes=5;

% 5 modes

Beta(1)=1.875;

Beta(2)=4.694;

Beta(3)=7.855;

Beta(4)=10.99554;

Beta(5)=14.13;

%============================================================

 a=(c4.*E.*d31.*B)./(C+Cpvdf);

% Specifying the number of sensors on the beam

nSensors=input('Enter the no of Sensors =');

for ii=1:nSensors

    fprintf('\n\n%s%d\n','Input For Sensor-',ii);
```

```
      SPosition(ii)=input(strcat('Enter the Position of
           Sensor-',num2str(ii),' = '));
      SWidth(ii)=input(strcat('Enter the Width of Sensor-
           ',num2str(ii),' = '));
end
%============================================================
% Initializing
   str1='X,Hmg{';
   str2='X,V_of_K_1{';
   str3='X,Hph{';
   str4='t,SensorVoltage{';
hmg=[];vof=[];hph=[];sVoltage=[];sys1=[];sys2=[];
TF2=[];TF1=[];TF3=[];TF4=[];TF5=[];TF6=[];TF7=[];TF8=[];TF9=[];TF
10=[];TF11=[];TF12=[];TF13=[];TF14=[];TF15=[];
QKII=[];QKI11=[];QKI12=[];QKI13=[];QKII2=[];QKII3=[];QKII1=[];QKI
21=[];QKI22=[];QKI23=[];QKI31=[];QKI32=[];QKI33=[];
CA=0;MA=0;
for ij=1:nSensors
      V_of_K_1{ij}=[];
      V_of_K_2{ij}=[];
      V_of_K_3{ij}=[];
      V_of_K_0{ij}=[];
      V_of_K_4{ij}=[];
      V_of_K_5{ij}=[];
End
```

```
%============================================================
% modal shapes, frequency of vibration and equation of motion
% calculations
 for  jj=1:nSensors
      SDist=SPosition(jj);
      Fy{1,1}=((1/sqrt(Ro.*L)).*(Beta./L)).*((cos((Beta./L).
           *SDist)cosh((Beta./L).*SDist))((sin(Beta)+sinh(Be
           ta))./(cos(Beta)+cosh(Beta))).*(((cos((Beta./L).*
           SDist))-cosh((Beta./L).* SDist))));

      SDist=SPosition(jj)-SWidth(jj);
      Fy{1,2}=((1/sqrt(Ro.*L)).*(Beta./L)).*((cos((Beta./L).
           *SDist)-cosh((Beta./L).*SDist))-sin(Beta)+
           sinh(Beta))./(cos(Beta)+cosh(Beta))).*(((cos((Bet
           a./L).*SDist))-cosh((Beta./L).* SDist))));
      DiffFyr(jj,:)=(a.*((Fy{1,1}-Fy{1,2})));
end
 Hptf=tf({ [Rin.*Cpvdf 0]},{[Rin.*Cpvdf 1]});
 for i=1:nmodes
    Omegai{i}=(((Beta(i))^2)./(L^2)).*(sqrt((E.*I)./(m)));
     Omegad{i}=(sqrt(1-(damp).^2).*Omegai{i});
      FyL(i)=(1/sqrt(Ro.*L)).*((cosh(Beta(i))-cos(Beta(i)))-
      ((cosh(Beta(i))+cos(Beta(i)))/(sinh(Beta(i))+sin(Beta(i))))
      *(((sinh(Beta(i)))-sin(Beta(i)))));
     QKI{i}=tf([(FyL(i))],[1
```

```
            (2.*damp.*Omegai{i}) (Omegai{i}).^2]);
end

%============================================================
% Calculation transfer functions for each sensors
TF1=DiffFyr(1,1).*QKI{1};
TF2=DiffFyr(1,2).*QKI{2};
TF3=DiffFyr(1,3).*QKI{3};
TF4=DiffFyr(1,4).*QKI{4};
TF5=DiffFyr(1,5).*QKI{5};
TF6=DiffFyr(2,1).*QKI{1};
TF7=DiffFyr(2,2).*QKI{2};
TF8=DiffFyr(2,3).*QKI{3};
TF9=DiffFyr(2,4).*QKI{4};
TF10=DiffFyr(2,5).*QKI{5};
TF11=DiffFyr(3,1).*QKI{1};
TF12=DiffFyr(3,2).*QKI{2};
TF13=DiffFyr(3,3).*QKI{3};
TF14=DiffFyr(3,4).*QKI{4};
TF15=DiffFyr(3,5).*QKI{5};
%============================================================
% incorporating the voltage follower characteristics and
% amplification factors
QKI11=parallel(TF1,TF2);
QKI12=parallel(QKI11,TF3);
```

```
QKI13=parallel(QKI12,TF4);

QKII1=parallel(QKI13,TF5);

QKII=(QKII1.*Hptf);

QKI21=parallel(TF6,TF7);

QKI22=parallel(QKI21,TF8);

QKI23=parallel(QKI22,TF9);

QKII2=parallel(QKI23,TF10);

QKII222=(QKII2.*Hptf);

QKI31=parallel(TF11,TF12);

QKI32=parallel(QKI31,TF13);

QKI33=parallel(QKI32,TF14);

QKII3=parallel(QKI33,TF15);

QKII333=(QKII3.*Hptf);

CA=1+(R2./R1);

MA= ((SA1./SA2)+(d1./d2));

for ij=1:nSensors

    V_of_K{ij}=[(CA).*QKII];%TF

     V_of_K2{ij}=[(CA.*MA).*QKII];% 5 times TF

     V_of_K1{ij}=(CA).*QKII222;%TF

     V_of_K3{ij}=(CA.*MA).*QKII222;% 5 times TF

     V_of_K4{ij}=(CA).*QKII333;%TF

     V_of_K5{ij}=(CA.*MA).*QKII333;% 5 times TF

end

%============================================================

% plotting free vibration for both the model designs
```

```
figure;
     [V_of_K_0{ij} t]=step(V_of_K{ij},1);
plot(V_of_K_0{ij},'k');
hold on;
    [V_of_K_1{ij} t]=step(V_of_K1{ij},1);
 plot(V_of_K_1{ij},'m');
 hold on;
    [V_of_K_4{ij} t]=step(V_of_K4{ij},1);
 plot(V_of_K_4{ij},'c');
     [V_of_K_2{ij} t]=step(V_of_K2{ij},1;
 plot(V_of_K_2{ij},'r');
 hold on;
     [V_of_K_3{ij} t]=step(V_of_K3{ij},1);
 plot(V_of_K_3{ij},'g');
 hold on;
     [V_of_K_5{ij} t]=step(V_of_K5{ij},1;
plot(V_of_K_5{ij},'b');
%============================================================
% plotting free vibration for experimental data
figure;
plot(s3n,'k');
hold on;
plot(s2n,'m');
hold on;
plot(s1n,'c');
```

```
hold on;
plot(s3a,'r');
hold on;
plot(s2a,'g');
hold on;
plot(s1a,'b');
%============================================================
% bode plot for both the designs for comparison
figure;
bode(V_of_K{ij});
    hold on;
bode(V_of_K2{ij},'g');
  hold on;
%============================================================
% plotting experimental data in time and frequency domain; DSA data
load('123_amp.mat');
     bodeplot(s21,s31);
     bodeplot(s11_a_d);
     bodeplot(ch_s11_a);
load('134_noamp.mat');
    bodeplot(s11,s41);
    bodeplot(s11_na_d);
    bodeplot(ch_s11_na);
G=c2d(V_of_K{ij},.01);%without times 2,modes=3
A=[1,-1.677,1.449,-0.3709,-0.08847,0.05634,0.01066,1.205e-
```

```
     19];
B=[.3153,0.08567,-0.1348,0.02101,0.02651,0.003624,3.349e-
     07];
in_noamp=in_noamp./0.5;
gg=filter(B,A,in_noamp);
figure;
plot(in_noamp);
hold on;
plot(out_noamp,'r');
hold on;
plot(gg,'g');
G1=c2d(V_of_K2{ij},.01); % with times 5.5 modes 3
A1=[1,-1.677,1.449,-0.3709,-0.08847,0.05634,0.01066,1.205e-
     19];
B1=[0.8671,0.2356,-0.3708,0.05778,0.0729,0.009967,9.209e-
     07];
in_amp=in_amp*7;
g1=filter(B1,A1,in_amp);
figure;
plot(in_amp);
hold on;
plot(out_amp,'r');
hold on;
plot(g1,'g');
%============================================================
```

Bibliography

[1] Nerves and blood vessels, 420evaluationsonline, August 2016.

[2] Pathology of the Heart and Blood Vessels, PMC,J Clin Pathol. 1970 Mar; 23(2): 191–192.

[3] Blood Vessels – Heart and Blood Vessel Disorders, Merck Manuals Consumer Version. 2016-12-22.

[4] http://ischemicstroke.org/tag/ischemic-stroke/

[5] http://www.medicinae-doc.info/2017/06/13/hemorrhagic-stroke/

[6] Factors that Affect Blood Pressure 6 *Dec 2014.*

[7] Furie B, Furie BC (2008). Mechanisms of thrombus formation, New England Journal of Medicine. *359 (9): 938–949.* PMID 18753650. doi*:*10.1056/NEJMra0801082.

[8] http://www.medbroadcast.com/condition/getcondition/embolism

[9] http://www.medbroadcast.com/condition/getcondition/embolism

[10] https://www.cincinnatichildrens.org/health/v/malformation

[11] Memphis Vascular Center, http://memphisvascular.com/,

http://memphisvascular.com/patient-education/brain-aneurysms/

[12] https://www.medicalnewstoday.com/articles/156993.php

[13] https://en.wikipedia.org/wiki/Intracranial_aneurysm

[14] http://anatomy-medicine.com/diseases-of-the-blood-vessels/170-aneurysm.html

[15] http://www.hopkinsmedicine.org/healthlibrary/conditions/nervous_system_disorders/subarachnoid_hemorrhage_134,68

[16] https://clinicalgate.com/a-survey-of-the-cerebrovascular-system/

[17] http://jsurgacad.com/article/endovascular-treatment-cerebral-aneurysm-early-experience-malaysian-tertiary-centre

[18] Pouratian N., Oskouian R.J., Jensen M.E., Kassell N.F., Dumont A.S., Endovascular management of unruptured intracranial aneurysms, Journal of Neurology and Neurosurgery Psychiatry, Vol.77(5), May 2006, PMC2117441

[19] http://www.hopkinsmedicine.org/neurology_neurosurgery/centers_clinics/aneurysm/treatment/aneurysm_clipping.html

[20] https://medicine.stonybrookmedicine.edu/surgery/blog/aortic-aneurysm-repair

[21] Chimowitz M.I., Lynn M.J., Derdeyn C.P., Stenting versus aggressive medical therapy for intracranial arterial stenosis, NEJM. 2011 Sep 15, 365(11): 993-1003. PMID 21899409

[22] Seibert B., Tummala R.P., Chow R., Faridar A., Mousavi S.A. and Divani A.A., Intracranial aneurysms: review of current treatment options and outcomes, Frontiers in Neurology, 2011, Vol. 2: 45, PMCID: PMC3134887

[23] Eddleman C.S., Welch B.G., Vance A.Z., Rickert K.L., White J.A., Pride G.L., Purdy P.D., Endovascular coils: properties, technical complications and salvage techniques, Journal of Neurointerventional Surgery, 2012, 10.1136/neurintsurg-2012-010263, ISSN: 1759-8478, 1759-8486

[24] https://www.slideshare.net/AllinaHealth/endovascular-treatment-of-brain-aneurysms-beyond-coiling

[25] Microvention, http://www.microvention.com/Products/Coils/MicroPlexProducts/tabid/63/Default.aspx

[26] http://www.neuroradiologist.com.au/services/intracranial-brain-aneurysm-sydney/

[27] Spiotta A. M., Wheeler A.M., Smithaso S., Ferdinand, Comparison of techniques for stent assisted coil embolization of aneurysms, Journal of NeuroInterventional Surgery, 2011; Vol. 3: A14 doi:10.1136/neurintsurg-2011-010097.31

[28] https://clinicalgate.com/endovascular-stenting-of-intracranial-aneurysms/

[29] Weber W., Siekmann R., Kis B., and Kuehne D., Treatment and Follow-Up of 22 Unruptured Wide-Necked Intracranial Aneurysms of the Internal Carotid Artery with Onyx HD 500, American Journal of Neuroradiology, 2005 Sep;26(8):1909-15.

[30] Zhang J., Lu X., Yang J., Wu Z., Stent-assisted coil embolization of intracranial aneurysms using Solitaire stent, Neurology in India, 2012 May-Jun; 60(3): 278-82. doi: 10.4103/0028-3886.98508.

[31] Saatci I., Yavuz K., Ozer C., Geyik S., Cekirge H.S.,, Treatment of Intracranial Aneurysms Using the Pipeline Flow-Diverter Embolization Device: A Single-Center Experience with Long-Term Follow- Up Results, American Journal of Neuroradiology, 2012 Sep;33(8):1436-46. doi: 10.3174/ajnr.A3246. Epub 2012 Jul 19.

[32] Cebral J.R., Mut F., Raschi M., Scrivano E., Ceratto R., Lylyk P., Putman C.M., Aneurysm Rupture Following Treatment with Flow-Diverting Stents: Computational Hemodynamics Analysis of Treatment, American Journal of Neuroradiology, 2011 Jan;32(1):27-33. doi: 10.3174/ajnr.A2398. Epub 2010 Nov 11.

[33] Schneiders J.J., Vanbavel E., Majoie C.B., Ferns S.P. and van den Berg R., A Flow-Diverting Stent Is Not a Pressure-Diverting Stent, American Journal of Neuroradiology, 2013 Jan;34(1):E1-4. doi: 10.3174/ajnr.A2613. Epub 2011 Aug 18.

[34] Cebral J.R., Mut F., Weir J., Putman C.M., Association of

Hemodynamic Characteristics and Cerebral Aneurysm Rupture, American Journal of Neuroradiology, 2011 Feb; 32(2): 264-70. doi: 10.3174/ajnr.A2274. Epub 2010 Nov 4.

[35] Jeong W. and Rhee K., Hemodynamics of Cerebral Aneurysms: Computational Analyses of Aneurysm Progress and Treatment, Computational and Mathematical Methods in Medicine, Vol. 2012, Article ID 782801, 11 pages

[36] Santos I.C..T. & Manuel J., TavaresR.S., Sepúlveda A.T.,Pontes A.J., Viana J.C. & Rocha L.A., Development of a Flexible Pressure Sensor for Measurement of Endotension, TMSi - Sixth International Conference on Technology and Medical Sciences, 2012, http://hdl.handle.net/10216/39346

[37] Ellozy, S. H., A. Carroccio & et al. 2004. First experience in human beings with a permanently implantable intrasac pressure transducer for monitoring endovascular repair of abdominal aortic aneurysms. Journal of Vascular Surgery 40(3): 405-412

[38] Silveira, P. G., C. W. T. Miller & et al. 2008. Correlation between intrasac pressure measurements of a pressure sensor and an angiographic catheter during endovascular repair of abdominal aortic

aneurysm. Clinics 63: 59-66.

[39] Springer, F., R. Schlierf & et al. 2007b. Detecting endoleaks after endovascular AAA repair with a minimally invasive, implantable, telemetric pressure sensor: an in vitro study. European Radiology 17(10): 2589-2597.

[40] O'Kelly C.J., Spears J., Chow M., Wong J., Boulton M., Weill A., Willinsky R.A., Kelly M. and Marotta T.R., Canadian Experience with the Pipeline Embolization Device for Repair of Unruptured Intracranial Aneurysms, American Journal of Neuroradiology, 2013 Feb;34(2):381-7. doi: 10.3174/ajnr.A3224. Epub 2012 Aug 2.

[41] Intra-Aneurysmal Pressure and Flow Changes Induced by Flow Diverters: Relation to Aneurysm Size and Shape, I.Larrabide, M.L. Aguilar, H.G. Morales, A.J. Geers, Z. Kulcsár, D. Rüfenacht and A.F. Frangi. American Journal of Neuroradiology April 2013, 34 (4) 816-822; DOI: https://doi.org/10.3174/ajnr.A3288

[42] Pressure Changes Within the Sac of Human Cerebral Aneurysms in Reponsse to Artificially Induced Transient Increases in Systemic Blood Pressure, David M. Hasan, Bradley J. Hindman, Michael M. Todd, Hypertension, 2015:66:324-331.

[43] Intra-aneurysmal hemodynamic alterations by a self-expandable

intracranial stent and flow diversion stent: high intra-aneurysmal pressure remains regardless of flow velocity reduction Yasuhiro Shobayashi, Satoshi Tateshima, Ryuichi Kakizaki, Ryo Sudo, Kazuo Tanishita, Fernando Viñuela, Journal of NeuroInterventional Surgery, Vol 5, Issue 3.

[44] Research progress on complications of intracranial aneurysms with flow-diverting stents Jinlu Yu, Lei Shi, Yongjie Yuan, Wei Wu, International Journal of Clinical and Experimental Medicine, 2016;9(7):13340-13350, ISSN:1940-5901/IJCEM0027840

[45] Delayed hemorrhagic complications after flow diversion for intracranial aneurysms: a literature overview Aymeric Rouchaud1 & Waleed Brinjikji 1 & Giuseppe Lanzino1,2 & Harry J. Cloft 1,2 & Ramanathan Kadirvel1 & David F. Kallmes 1,2, Interventional Neuroradiology, (2016)58:171–177 DOI10.1007/s00234-015-1615-4.

[46] Flow-Diverting Stent Is Not a Pressure-Diverting Stent, J.J. Schneiders, E. VanBavel, C.B. Majoie, S.P. Ferns and R. van den Berg, American Journal of Neuroradiology January 2013, 34 (1) E1-

E4; DOI: https://doi.org/10.3174/ajnr.A2613

[47] Nanorobot for Brain Aneurysm, Adriano Cavalcanti, Bijan Shirinzadeh, Toshio Fukuda, Seiichi Ikeda, , The International Journal of Robotics Research, Volume: 28 issue: 4, page(s): 558-570 https://doi.org/10.1177/0278364908097586

[48] Development of Sensing System for Cerebral Aneurysm Treatment, Yoshitaka NAGANO Hideo FUJIMOTO, NTN Technical REVIEW No.76（2008）

[49] Shen Y., Winder E., Xi N., Pomeroy C.A., Wejinya U.C.,Closed-Loop Optimal Control-Enabled piezoelectric Microforce Sensors, IEEE/ASME Transactions on Mechatronics, Vol.11, NO. $, August 2006.

[50] http://www.nacd.org/middle-ear-fluid/

[51] https://naturalhistory.si.edu/mna/glossary.cfm?glossary_id=42

[52] Diana C. Emanuel, Sumalai Maroonroge, Tomasz R. Letowski, Auditory function, http://www.usaarl.army.mil/publications/HMD_Book09/files/Section%2016%20%20Chapter%209%20Auditory%20Function.pdf

[53]] D.J. Kelly1, A.W. Blayney2 and P.J. Prendergast1, Biomechanics of

ossiculoplasty, CME Bulletin Otorhinolaryngology Head and Neck Surgery, 7, 2003, pp 64 – 66

[54] KURZ,http://www.atosmedical.com/Corporate/Products/~/media/Files/Ear/Catalogs%20etc/Kurz/7942_200808B_web.ashx

[55] Piezoelectric and piezoresistive sensors, slideshare, https://www.slideshare.net/IndranilBhattacharyya/piezoelectric-and-piezo-sensors

[56] https://www.sparkfun.com/datasheets/Sensors/Flex/MSI-techman.pdf

[57] http://www2.pitt.edu/~qiw4/Academic/ME2082/references/Fundamental%20Piezo1.pdf

[58] Sirohi J., Chopra I., Fundamental Understanding of Piezoelectric Strain Sensors, Journal of Intelligent Material Systems and Structures, Vol.11, April 2000

[59] Mohan N., Tang S., and Shen Y., Ear-Hearing Mechanism Inspired Miniature Pressure Sensing System for Monitoring Brain Aneurysms, Proceeding of the 2017 IEEE International Conference on Real-time Computing and Robotics, pp. 733-738, 2017.

[60] Mohan N., Luo Y., Shen Y., Developing a Self-Powered and Directly Digitized Piezoelectric Micro Sensor for Monitoring Blood Pressure

Change inside Brain Aneurysm after Endovascular Treatment: A Feasibility Study, Proceedings of 2015 IEEE International Conference on Cyber Technology, pp. 2115-2120, 2015.

[61] Mohan N., Luo Y., Shen Y., Multi-striped PVDF Miniature Pressure Sensing System for Monitoring Embolized Brain Aneurysms: Design, Modeling, and Validation, The 2015 ISSAT International Conference on Modeling of Complex Systems and Environments (MCSE), 2015.

[62] Zohar Y., Pressure Loss in Constriction Microchannels, Microelectro-mechanical Systems, Journal of, 2002. 11:p.236–244. 21.

[63] Baumer laser distance sensor, OADM 2016, OADM 2116 series manual.

[64] Leonard Meirovitch, Fundamentals of Vibrations, McGraw Hill, 2001.

[65] A Novel Piezoelectric 3-D Micro-Force Sensor for Force-Guided Bio-Manipulation: Design and Test, Zane Ricks, Yantao Shen.

[66] https://en.wikipedia.org/wiki/Blood_pressure

[67] https://static1.squarespace.com/static/5230e9f8e4b06ab69d1d8068/t/56ce6c37f699bb91e5aa778b/1456368704362/Dynamic+Signal+Analysis+Basics.pdf

[68] http://www3.imperial.ac.uk/pls/portallive/docs/1/28811707.PDF

[69] Jacob J. Adams , Eric B. Duoss , Thomas F. Malkowski , Michael J. Motala, Bok Yeop Ahn , Ralph G. Nuzzo , Jennifer T. Bernhard , and Jennifer A. Lewis, Conformal Printing of Electrically Small Antennas on Three- Dimensional Surfaces, Advanced Materials, Volume 23, Issue 11, pages 1335–1340, March 18, 2011.